Earth Observing System (EOS)

Microwave Limb Sounder (MLS)

EOS MLS Level 1 Data Processing Algorithm Theoretical Basis
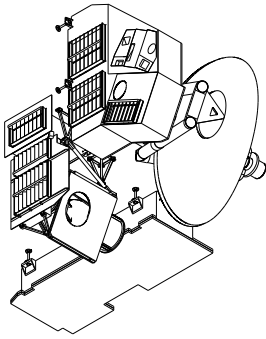
$$\overset{\bullet}{\mathbf{P}}_{\mathbf{i}}^{\mathbf{L}} = \frac{1}{\eta_{\mathbf{r}}^{\mathbf{ML}}} \left(\frac{\mathbf{C}_{\mathbf{i}}^{\mathbf{L}} - \widehat{\mathbf{C}}_{\mathbf{i}}^{\mathbf{S}}(\mathbf{L})}{\widehat{\mathbf{g}}_{\mathbf{i}}(\mathbf{L})} + \eta_{\mathbf{r}}^{\mathbf{MS}}\overset{\bullet}{\mathbf{P}}_{\mathbf{r}}^{\mathbf{S}} - (1 - \eta_{\mathbf{r}}^{\mathbf{ML}})\overset{\bullet}{\mathbf{P}}_{\mathbf{r}}^{\mathbf{BL}} + (1 - \eta_{\mathbf{r}}^{\mathbf{MS}})\overset{\bullet}{\mathbf{P}}_{\mathbf{r}}^{\mathbf{BS}} \right)$$

Robert F. Jarnot, Herbert M. Pickett and Michael J. Schwartz

Version 2.1

25 March 2025

JPL

Release Record

Version	Date	Comments
1.0	15 Jan 1999	Initial version
1.1	15 Oct 1999	Released following formal review of Version 1.0 by NASA board reviewing the EOS CHEM Algorithm Theoretical Basis Documents. This document received the top grade of 'A' from the review board. The board recommendations which apply to this document are italicized below, followed by the (non-italicized) responses of the MLS team.

Investigate image enhancement methods for possible implementation in Level 1 processing ... This was investigated during the design of EOS MLS, and our early investigations indicated that the appropriate place in data processing to implement resolution enhancement is Level 2 (retrieval), not Level 1.

A more complete (compared to that described in the ATBD's) validation plan should be developed for the experiment. Particular emphasis should be on self-consistency plans and in-orbit calibration and performance monitoring. This is planned, and will be documented in the MLS Calibration Plan. See [4] for examples of this kind of activity on UARS MLS.

The performance of the electronics unique to EOS MLS should be assessed. This is planned as part of instrument development, and will be documented in the MLS Functional Verification Plan.

No changes to the document were needed as a result of these recommendations. Changes to Version 1.0 are described below, and reflect expected progress and correction of a few minor errors:

- Units for rotation matrices in Table 4.2 corrected.

- Equations (4.13) and (4.15) giving atmospheric limb radiance corrected (radiance offset components were not being divided by antenna reflectivity, ρ).

- Clarification added preceding Equations (4.16) as to why Level 1 processing treats radiometric calibration as a double sideband calculation, even though earlier formulations (e.g., Equation (4.5)) are given single sideband.

- Minor changes to correct grammatical and spelling errors, or clarify the meaning of some statements.

Version	Date	Comments
2.0	22 Jun 2004	Numerous updates to reflect major release version, and to make the document more closely represent reality rather than predictions. Also incorporated comments from Drs. Bill Read and Nathaniel Livesey.
2.1	25 Mar 2025	Correct sign error in Equations 4.13 and 4.14

This is: /users/jarnot/texinput/L1TB/L1AlgThBasis.TEX

Contents

Chapter 1

Introduction

EOS MLS measures thermal limb emission from molecules and radicals of special interest in the stratosphere and upper troposphere, with some measurements extending into the mesosphere. By measuring emission spectra as a function of limb altitude it is possible during ground processing to infer concentration profiles of various species including ClO, BrO, CH_3CN, O_2, HNO_3, N_2O, CO, H_2O, H_2O_2, HO_2, O_3, OH, HCl, HCN, SO_2 and cloud ice water content. Measurement of O_2 emission provides pressure and temperature data necessary for accurate constituent retrievals, and the spacecraft inertial reference unit (IRU) provides the pointing reference necessary for measurement of geopotential height. An overview of the EOS MLS experiment is given in [1].

The EOS project has defined several 'Levels' of data, the definitions below taken from the MTPE EOS REFERENCE HANDBOOK (1995 EDITION)[2]:

Level 0: *Reconstructed, unprocessed instrument/payload data at full resolution; any and all communications artifacts, e.g., synchronization frames, communications headers, duplicate data removed.*

Level 1A: *Reconstructed, unprocessed instrument data at full resolution, time-referenced, and annotated with ancillary information, including radiometric and geometric calibration coefficients and georeferencing parameters, e.g., platform ephemeris, computed and appended but not applied to the Level 0 data.*

Level 1B: *Level 1A data that have been processed to sensor units.* For MLS these include calibrated instrument radiances and related (e.g., instrument engineering) data.

Level 2: *Derived geophysical variables at the same resolution and location as the Level 1 source data.*

Level 3: *Variables mapped on uniform space-time grid scales, usually with some completeness and consistency.*

Level 4: *Model output or results from analyses of lower level data, e.g., variables derived from multiple measurements.*

This document gives the theoretical basis for algorithms used in the EOS MLS Level 1 processing software (i.e., the software used to generate daily Level 1B data files from Level 0 and ancillary data input). The primary tasks of this software are to:

1. Qualify each data quantity using instrument configuration and checksum data as well as data transmission quality flags. Apply statistical tests for data quality and 'reasonableness.'

2. Calibrate the instrument engineering data (e.g., voltages, currents, temperatures and encoder angles).

3. Interpolate filter channel space reference measurements onto the times of each limb measurement and difference the interpolates from the measurements.[1]

4. Interpolate filter channel calibration target measurements[2] onto the times of each limb measurement and compute radiometric gain.

5. Determine the total signal power analyzed by each Digital Autocorrelator Spectrometer (DACS) during each data integration.

6. Convert each DACS data integration from an autocorrelation measurement in the time domain into a spectral measurement in the frequency domain.

7. Estimate separately the spectrally smoothly-varying and spectrally-averaged components of the limb port signal arising from antenna emission and scattering effects.

8. Calibrate the limb radiances. For this instrument we compute the radiance at the limb port of the radiometer module, *including non-atmospheric radiance contributions from antenna emission and scattering.* It is the task of the retrieval/forward model software (Level 2) to compute the atmospheric component of limb radiation reaching this interface. This is a departure from UARS MLS practice, for which Level 1 estimated the true *limb* radiance. It is necessitated by the greatly increased bandwidth of EOS MLS radiometers, and the double-sideband nature of most measurements. Estimates of the random component of uncertainty (noise) on each limb radiance are also determined.

9. Combine spacecraft inertial pointing and star tracker data with spacecraft and GHz antenna structural/thermal data and scan mechanism encoder data to estimate the boresight angles for each radiometer.

10. Collect and generate ancillary data (e.g., tangent point location, local solar time, local solar zenith angle, flags for bright objects in field of view) which are needed in Level 2 processing.

11. Produce a Log file summarizing instrument performance and outputs.

This software processes the Level 0 product into the Level 1B data set used as the primary input to retrieval (Level 2) software. Level 1 software also processes and/or generates

---

[1] The reference view for limb measurements is nominally the space view, but the processing software also allows the ambient calibration target views to be used as the primary reference. For clarity, use of the space reference view is assumed in the rest of this document.

[2] There are two calibration targets in the EOS MLS GHz module, one at instrument ambient temperature, the other passively cooled by approximately 20 K. Level 1 software can be instructed to use either GHz target.

additional ancillary data not included in the instrument Level 0 stream, but which are needed at Level 2. These data include tangent point locations and solar zenith angles at the tangent points.

The following is a list of the data products for which the algorithms described in this document will be used:

1. Calibrated limb radiances (and uncertainties) for all channels. For the GHz radiometers we determine limb port radiances.

2. Estimates of instrument spectral baseline.

3. Calibrated engineering data (e.g., voltages, currents and temperatures).

4. System noise temperatures.

5. Reference χ^2.

6. Interpolated channel radiometric gains.

Radiances, including spectral baseline, are written to the daily Radiance File, and the engineering and related diagnostics data (such at the noise temperatures, reference χ^2 and radiometric gains) to Diagnostics files.

1.1   The ATBD review

A Peer Review for the main ATBDs of the EOS Aura (formerly Chem I) experiments was held on 18 May 1999 at the Goddard Space Flight Center (GSFC). All EOS MLS ATBDs were well received (receiving the top grade of 'A'), and the board recommendations for the Level 1 ATBD (this document), together with responses, are given in the release record at the beginning of this document.

1.2   Status of this document

Numerous changes/updates have taken place to this document since the ATBD review, reflecting changes and updates to algorithms, minor changes to the nominal operating mode(s), and minor corrections. Where we have additional information, such as in the area of resource requirements, estimates have been updated based on experience with the current pre-launch Level 1 product processing instrument data from performance validation and calibration data sets.

A list of these changes is available as comments in the LaTeX source of this document, embedded in the release record.

Chapter 2

Overview and heritage

2.1 Overview of EOS MLS Level 1 data processing

Level 1 software provides the initial steps in the processing of EOS MLS instrument and ancillary data. The inputs and outputs of this process are illustrated in Figure 2.1. Input data to Level 1 processing software are the 'raw' uncalibrated instrument spectrometer and engineering data, spacecraft ancillary data, startup information, and command and parameter files. The command files provide the mechanism for informing the processing software of the sources of input data and any other details of the processing to be performed, while the user inputs represent additional command line (runstream) parameters. The parameter files contain calibration data and conversion parameters necessary to convert the raw data into calibrated output quantities. The startup file (if available) contains data structures created at the end of processing of the previous contiguous data set which serve to provide continuity at the startup of a new processing run.

The primary output files used as input to Level 2 processing contains the calibrated limb radiances and uncertainties, together with additional data (such as pointing and baseline information) needed by that software. Additional output files contain calibrated engineering and performance diagnostic data, logging data which provides a 'quick look' of instrument and software operation, and a termination file which serves as the startup file for a subsequent data processing run.

For UARS MLS the startup and termination files were separate from the daily Level 0 input file, and were created during Level 1 processing. For EOS MLS we retain this concept, but no additional files are created. Instead, the end of the previous day's data and the start of the next day's data serve this function. This change is logical for the current software because EOS Level 0 data are delivered in 2 hour 'chunks.'

2.2 Heritage

The EOS MLS instrument is a direct descendent of UARS MLS, with increased and enhanced spectral coverage by virtue of:

1. An increased number of radiometers (5 unique center frequencies versus 3),

2. a larger number (19 versus 6) standard filterbanks with broader spectral coverage ($\sim$1,300 MHz versus $\sim$500 MHz),

4

3. the addition of 5 mid-band filter spectrometers with ∼200 MHz bandwidth,

4. 12 additional broad individual filter channels[1] in the IF passbands of the 118 and 240 GHz radiometers, and

5. the addition of 4 Digital Autocorrelator Spectrometers (DACS) with ∼10 MHz bandwidth and 0.2 MHz resolution to complement selected standard filterbanks.

In addition to the increased complement of radiometers, their IF bandwidths range from 7 to 13 GHz, substantially larger in both absolute and relative terms than the 0.5 to 3 GHz bandwidths of the UARS radiometers. The data sampling rate of 6 Hz, combined with continuous scanning and narrower fields of view at 240 and 640 GHz for EOS MLS, provides substantially improved vertical resolution compared to the step-scanned implementation with 0.5 Hz sampling on UARS.

The front-end mixers are all Schottky diode implementations as before, but a significant enhancement in terms of reliability comes from the use of monolithic diodes in all front-end mixers. A significant reduction in signal/LO diplexing complexity, together with the substantially larger IF bandwidths, arises from the use of dual-diode subharmonically pumped mixer implementations. The antenna/telescope for the GHz measurements is based on the design flown on UARS, and is very similar in external dimensions.

In-flight radiometric calibration of the GHz radiometers is performed using a Switching Mirror which directs the radiometer FOVs sequentially to 'cold space' and ambient target

---

[1]These channels are referred to as Wide Filters and Broad Filters interchangeably in the following text.
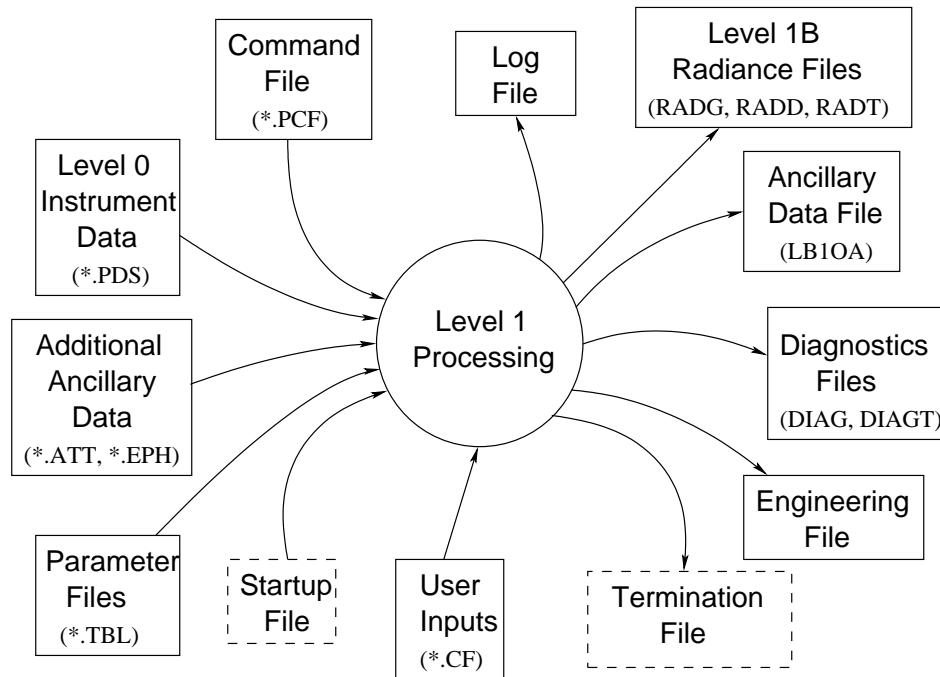
Figure 2.1: High level dataflow diagram for Level 1 data processing. The startup/termination files are the previous/next day's .PDS data files.

references, as on UARS. For the THz radiometers a single scanning reflector serves for both limb scanning and radiometric calibration. Scanning of the both GHz and THz FOVs through the atmospheric limb is continuous, but the data digitization implementation in the filter spectrometers is derived directly from the UARS design. This allows the GHz radiance calibration algorithms for EOS MLS to be directly descended from, and very similar to, those used in UARS MLS. The operational characteristics of the THz radiometers are such that some details of the radiometric calibration algorithms are of necessity quite different. The algorithms for the THz radiometers are described separately in this document.

Engineering data are acquired using circuitry based on the design concepts used in UARS MLS with minor enhancements to increase data resolution, allowing slightly modified versions of the UARS processing algorithms to be used for calibrating these data, and identical algorithms to be used for converting the calibrated data into engineering units.

The considerable experience obtained with the processing of data from, and operation of, UARS MLS over a decade has had a considerable influence on the design of the processing software for this instrument. Key concepts developed for UARS MLS Level 1 processing, such as the generation of Calibration Windows (described in Appendix D), and the use of startup and termination data sets to avoid 'edge effects' on day boundaries, are retained in EOS Level 1 software. Significant differences between the UARS and EOS MLS instruments are described in Appendix A.

Chapter 3

The EOS MLS instrument

EOS MLS views the atmospheric limb in the orbital plane with a vertical scan centered $\sim 25.4°$ below the spacecraft velocity vector. The nominal atmospheric scan ranges from tangent heights of ~ 0 km to ~ 95 km, but is fully programmable to accommodate alternate measurement strategies. The GHz and THz limb-viewing portions of each scan are synchronized, but the THz one ends ~ 1 s earlier than the GHz one to stagger current pulses generated by the two mechanisms. Measurements are made in 5 bands with radiometers centered near 118, 190, 240, 640 GHz and 2.5 THz, called R1 through R5 respectively. The 2.5 THz radiometer resides in its own assembly referred to as the 'THz module,' the other radiometers being grouped together in the larger 'GHz module.' Both radiometer modules share a common Spectrometer module which houses 19 25-channel filterbank spectrometers, 5 11-channel mid-band spectrometers (~ 200 MHz bandwidth) and 4 129-channel digital autocorrelator spectrometers (DACS, 10 MHz bandwidth). 12 additional broad filter channels (each with ~ 0.5 GHz bandwidth) reside in the GHz module. The GHz and THz modules contain separate antennæ/telescopes, scan systems and radiometric calibration targets, but their operation is synchronized via the common Command and Data Handling assembly (C&DH). A simplified signal flow block diagram of the instrument is shown in Figure 3.1.

3.1   Spectral bands

EOS MLS measures thermal emission from the Earth's atmospheric limb in 21 major spectral bands, each subdivided into 25 channels. The 21 bands (B1 to B21) are covered by seven radiometers operating at frequencies defined in Table 3.1, which also identifies the principal species affecting each band. R1 is implemented with 2 radiometers (R1A and R1B) to provide redundancy for the crucial pressure/temperature (P/T) measurements. R5 is implemented with 2 radiometers to provide additional signal-to-noise for the OH measurements, with a redundant pressure measurement band (B20) implemented on the second radiometer to provide measurement resilience. The bands enclosed in parentheses in Table 3.1 are turned off in the primary nominal instrument operating mode.

Additional bands are analyzed by 5 mid-band spectrometers (B27 to B31), 12 broad (~ 500 MHz) filter channels (B32 to B34) and 4 digital autocorrelator spectrometers[1] (DACS, B22 to B26). The mid-band spectrometers and DACS provide additional spectral resolution

---

[1]Although 5 DACS bands are indicated, B25 and B26 timeshare a common DACS unit.

GHz Scanning Antenna Assembly

Primary
Reflector

GHz Module

Spectrometer Module

Thermal Radiation from

Atmospheric Limb

118 GHz
Radiometer

Spectrometer

Spectrometer

Spectrometer

190 GHz
Radiometer

Tertiary

Secondary

Space View

Switching
Mirror

Optical
Multiplexer

240 GHz
Radiometer

Switch
Network

Spectrometer

Calibration
Targets

Spectrometer

THz Module

Calibration
Target

640 GHz
Radiometer

Thermal Radiation
from Atmospheric

THz Scan and
Switching
Mirror

Telescope

2.5 THz
Radiometer

Command and
Data Handling

Limb and Space
View

To Spacecraft

Figure 3.1: Simplified signal flow block diagram for EOS MLS. Some spectrometer channels (broad filters) are implemented within the radiometer IF downconversion chains. The 118 GHz and 2.5 THz radiometers implement receivers with dual (orthogonal) polarizations, not shown in the figure.

The EOS MLS Instrument

for sub-bands within spectral regions analyzed by selected 25-channel filter bank spectrometers. The placement of all spectrometers, together with representative atmospheric radiance spectra, are illustrated in Figure 3.2.

3.2 Spectrometers

EOS MLS implements 4 different 'types' of spectrometer:

1. A set of 19 25-channel 'standard' filterbank spectrometers,

2. A set of 5 11-channel 'mid-band' filterbank spectrometers spectrometers,

3. 12 discrete, non-adjacent, non-overlapping 'broad filter' channels, and

4. 4 129-channel digital autocorrelator spectrometers (DACS).

3.2.1 Standard spectrometers

The standard filter spectrometer design is based on UARS MLS, but increases the number of channels per spectrometer from 15 to 25, and the analyzed bandwidth from ∼500 to ∼1,300 MHz, while reducing mass, power consumption and volume. Details of channel relative positions and widths for both these and the mid-band filterbank spectrometers are given in Table 3.2.

3.2.2 Mid-band spectrometers

The mid-band spectrometers replicate the center 11 channels of a standard 25-channel filterbank spectrometer. These spectrometers are fabricated from a subset of the building blocks used to manufacture the more complex, modular 25-channel filterbank spectrometers.

3.2.3 Broad Filter channels

These are discrete single channel filters which use the detector/digitizer design employed in the 11 and 25-channel spectrometers. Unlike the other spectrometers, the broad filter channels are implemented within the GHz module.

The common implementation of the back end electronics for all filter spectrometer channels allows the use of common algorithms within Level 1 software for processing data from the 400+ filter spectrometer channels supporting the GHz radiometers, and a slightly different common algorithm set to support the 150 channels analyzing the THz radiometer data.
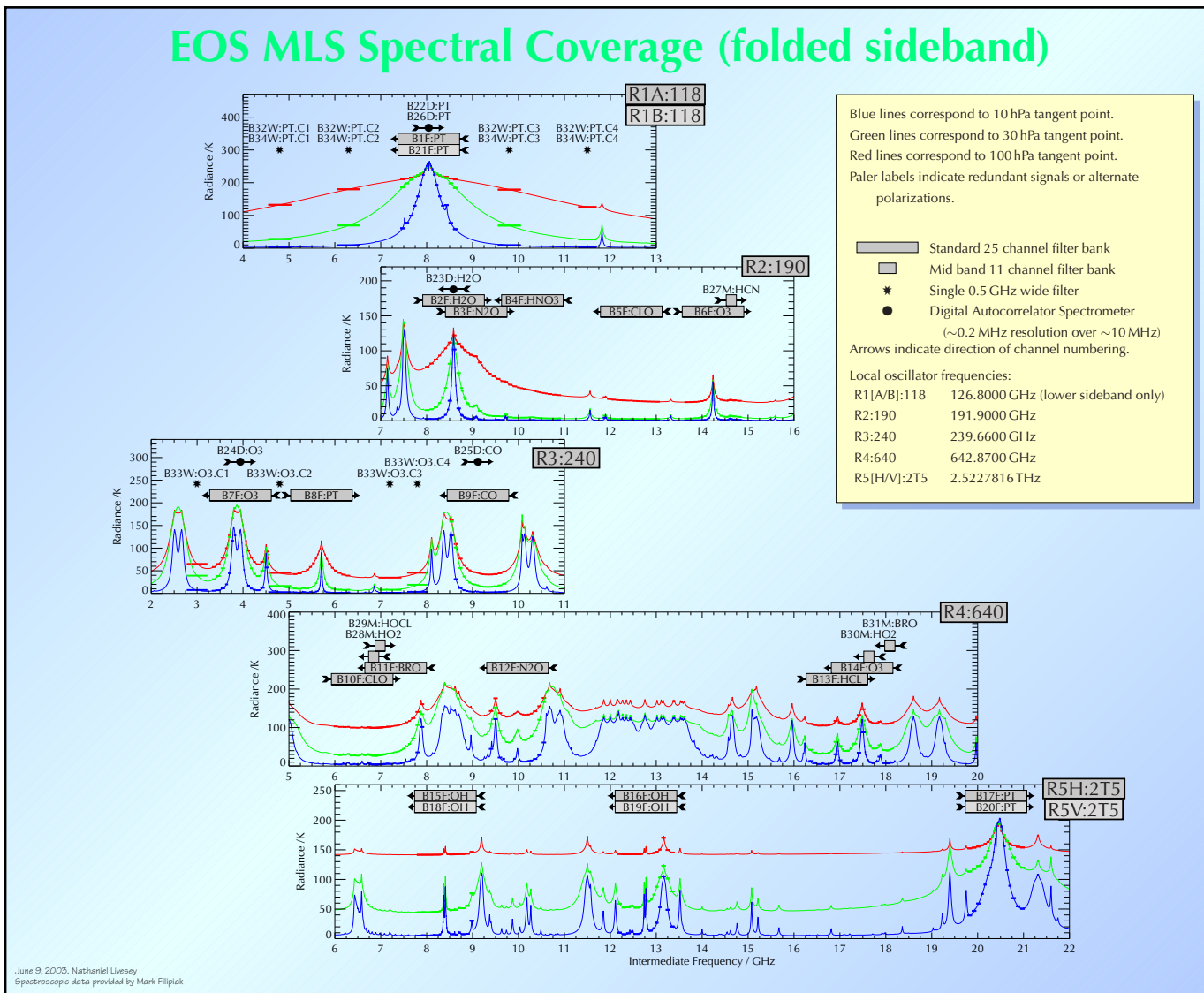
Figure 3.2: This figure shows the bands measured by EOS MLS, and the spectral coverage of all spectrometers. The abscissa of each panel indicates the IF frequency in GHz. The three spectra in each panel correspond to nominal atmospheric radiances for tangent pressures of 10, 30 and 100 hPa and assume single sideband response for R1 and equal relative sideband responses all other radiometers. This figure is from N.J. Livesey.

Table 3.1: MLS Spectral Bands analyzed with 25-channel Filter Bank Spectrometers. Bands in parentheses are redundant (for measurement resiliency) and are not normally powered on. Negative IF frequencies indicate the the primary signals come from the lower sideband of the radiometer. See text for additional details.

Radiometer 1st. LO frequency	Band	IF Center Frequency (GHz)	Primary Measurement
R1 126.8000 GHz	B1 (B21)	-8.0470	O_2
R2 191.9000 GHz	B2	-8.5858	H_2O
	B3	9.0798	N_2O
	B4	-10.3013	HNO_3
	B5	12.4566	ClO
	B6	14.2367	O_3
R3 239.6600 GHz	B7	-9.1168	CO
	B8	-5.7085	P/T
	B9	-3.9449	O_3
R4 642.8700 GHz	B10	6.5959	ClO
	B11	7.3237	BrO
	B12	9.9785	N_2O
	B13	-16.9373	HCl
	B14	-17.4844	O_3
R5 2522.7816 GHz	B15	-8.4081	OH
	B18	-8.4081	OH
	B16	-12.7759	OH
	B19	-12.7759	OH
	B17	-20.4012	P
	(B20)	-20.4012	P

3.2.4 Digital Autocorrelator Spectrometers (DACS)

The DACS implement high resolution ($\sim$0.2 MHz) spectrometers with uniform spectral coverage over a measurement bandwidth of $\sim$10 MHz. Their implementation and operation is described in detail in Appendix G.

The operation of a DACS is very similar conceptually to that of a Fourier Transform Interferometer (FTI). Consider Figure 3.3 which shows a simplified FTI in the upper half, and the analogous DACS below. In the FTI the band-limited input signal is split into 2 paths using a beam splitter, and recombined at the detector. As the path length is varied by altering the position of the moving reflector, the detector records the interferogram generated by the optical signals traversing the 2 paths. The path difference varies from 0 (to capture the zero order signal when the 2 path lengths are identical, in order to determine the total power in the input signal), to a maximum path difference which defines the longest wavelength (lowest frequency) distinguishable by the measurement system. The path length differences between successive readouts of the detector define the bandwidth of the measurement system; the maximum path length difference sets the resolution. Measurement bandwidth and resolution are limited by the Nyquist criterion to wavelengths corresponding to twice the path length

Table 3.2: Positions and widths of filters in the 25-channel and 11-channel (mid-band) filterbank spectrometers. Channel positions are with respect to spectrometer center frequency which is 1,300 MHz for the standard (25 channel) spectrometers, and 200 MHz for the mid-band spectrometers. Widths are the nominal 3 dB channel widths.

channel #	position (MHz)	width (MHz)	channel #	position (MHz)	width (MHz)	channel #	position (MHz)	width (MHz)
1	-575	96	8	-79	32	19	119	48
2	-479	96	9	-51	24	20	175	64
3	-383	96	10	-31	16	21	239	64
4	-303	64	11	-17	12	22	303	64
5	-239	64	12	-7	8	23	383	96
6	-175	64	13	0	6	24	479	96
7	-119	48	14	7	8	25	575	96
			15	17	12			
			16	31	16			
			17	51	24			
			18	79	32			

← mid-band filterbank →

←———   25-channel filterbank   ———→

increment and twice the total path length difference respectively.

The DACS utilize a shift register to provide the delayed (path length altered) form of the digitized input signal, and a chain of simple multipliers generate the equivalent of the interferogram. Instead of a single 'detector,' the output from each multiplier is accumulated simultaneously. This is a major advantage of the DACS compared to the FTI, since all 'path length differences' are measured simultaneously with subsequent signal-to-noise benefits. Other obvious advantages include a completely electronic implementation with no precision optical or moving parts, and high accuracy in the frequency domain for the transformed signal since the sampling clock is a precise 25-MHz crystal oscillator. At the end of a data integration period the accumulators contain the measured autocorrelation function of the input signal, the same quantity measured by the FTI as its path length is swept. The coarse quantization of the input signals by the DACS results in a distortion in the measured autocorrelation function, and a transformation (described in Appendix G) is required to obtain an estimate of the true autocorrelation function before Fourier transforming into the frequency domain.

In both measurement systems the input signal is typically band-limited to less than the bandwidth implied by the Nyquist criterion in order to enhance signal-to-noise ratio (by virtue of oversampling). In the case of the EOS MLS DACS this is also done to ease the implementation of the input band defining filter. The mathematical conversion of the measured autocorrelation function/interferogram into the frequency domain is the same for both systems, the DACS having the advantage that no additional processing and interpolation is necessary to correct for imprecision in the relative delays of the 2 signal paths, including mirror placement for the critical zero path length measurement.

Fourier Transform Interferometer

Digital Autocorrelator Spectrometer (DACS)
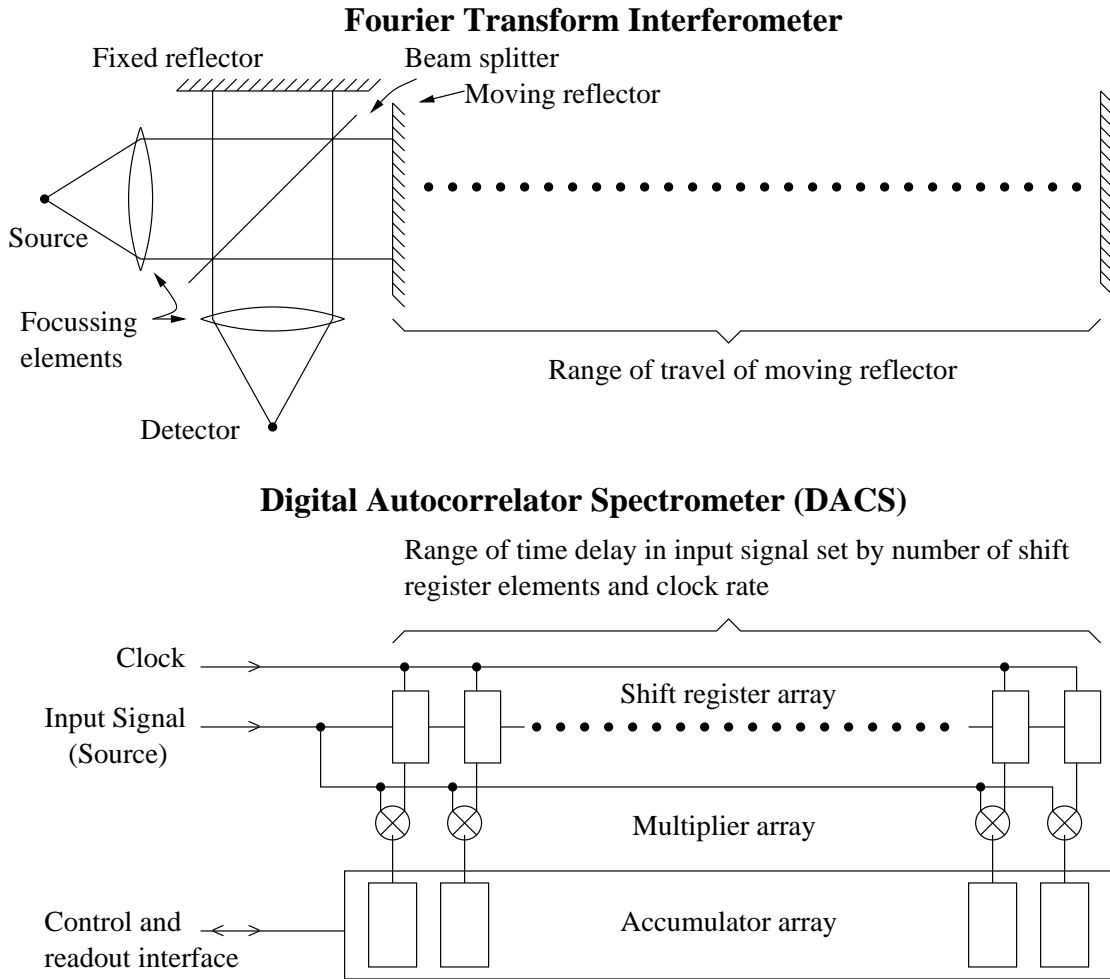
Figure 3.3: Simplified block diagram showing signal flow in a Fourier Transform Interferometer (upper portion) and a digital autocorrelator spectrometer (lower portion). Additional circuitry in the DACS (not shown) is used to measure input signal power during each data integration.

3.3 Timing and FOV scanning

The basic internal timing events of EOS MLS are the minor and major frames (MIF and MAF) which define the integration repeat cycle and FOV atmospheric scan cycle respectively. Instrument operation over timescales of one MIF to an orbit are illustrated in Figure 3.4. Spectrometer data are integrated simultaneously in all active channels during every MIF, each of which has a nominal duration of $\frac{1}{6}$ s (but is programmable over the range $\frac{1}{6}$ to $\frac{1}{3}$ s). Each MIF starts with a 5 ms dead time during which housekeeping activities (e.g. resetting counters) take place. Each MAF consists of an integer number of MIFs, and there are 240 MAFs (nominal) per orbit. The number of MAFs per orbit is programmable, but we choose an even integer number of limb scans per orbit. We also require the sampled latitude bands to be the same for ascending and descending observations which forces the integer number

of limb scans per orbit to be a multiple of 4. Since the orbital period will vary slightly with orbit decay and lunar gravitational influences, the synchronization of limb scans to the orbit is a software function of the Command and Data System (C&DH), with synchronization maintained by the infrequent addition of one MIF to the end a MAF. This requires the 'nominal' MIF duration to be slightly shorter than 'perfect.' MIF duration is tunable in increments of $83.\dot{3}$ ns, and it will be one of the tasks of the MLS Flight Operations team to tune MIF duration to account for timing changes resulting from orbit corrections. We anticipate being able to perform this tuning so that MAF length corrections occur less than once per day.

An important consequence of the factors (1) that limb scans are synchronized to the (variable length) orbit, and (2) that MAFs are composed of an integer number of (nominally fixed length) MIFs, is that MAFs are not of constant length, and will occasionally increase in duration by 1 MIF. The main impact of this in Level 1 processing is that calibration measurements (i.e., Space and Target dwells) will have a slightly non-uniform distribution in time.

In-flight radiometric calibration is accomplished in the GHz module by sequencing the switching mirror through three positions as illustrated in the lower portion of Figure 3.5. This provides simultaneous radiometric calibration of all GHz bands and channels. Motion of both the antenna and switching mirror is smoother than shown in the figure to limit disturbances to the spacecraft which could adversely effect the accuracy of atmospheric measurements of
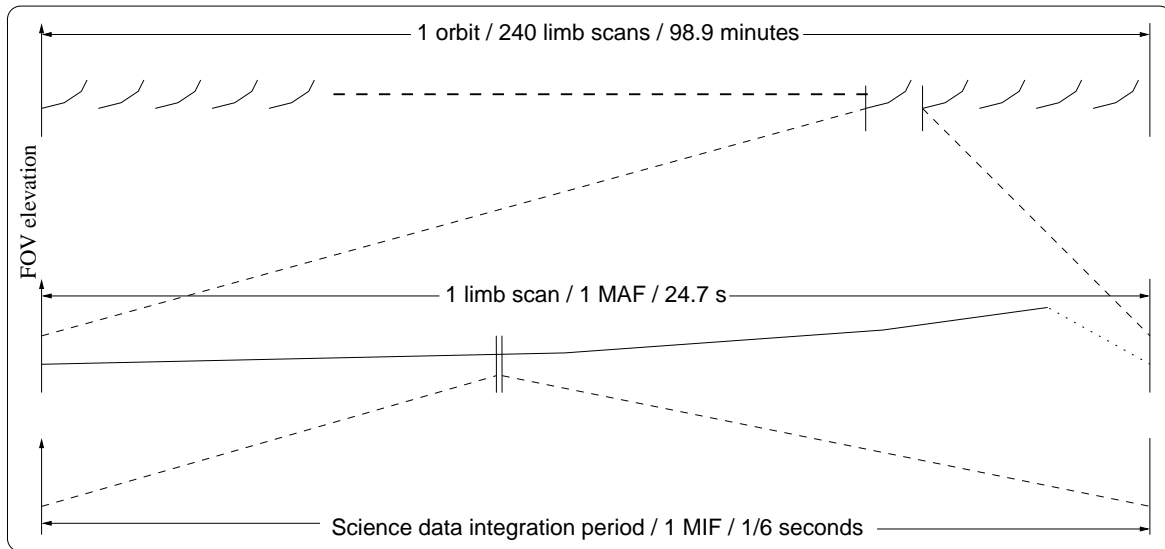
Figure 3.4: Sketch of MLS operation over timescales of an orbit, a major frame (MAF) and a minor frame (MIF). Major and minor frame boundaries are coincident, requiring an integer number of MIFs per MAF. The patterns replicated sequentially along an orbit represent limb scans (antenna angular position) and are not shown to scale. The gaps between limb scans shown in the orbit duration segment, and the dotted portion of the MAF length segment, are used to perform radiometric calibration and retrace prior to the start of the subsequent limb scan.

MLS and other instruments on the platform. The nominal observing mode devotes $\sim$1 s of each MAF to viewing the ambient calibration target, and $\sim$2 s to viewing cold space. The THz module uses a single scanning mirror which serves for both atmospheric scanning and viewing the radiometric calibration references. The cold space view for this module is obtained by raising the limb FOV $\sim$1° above the highest atmospheric view, and the target is viewed by rotating the FOV by $\sim$186° from the nominal limb observing position, as shown in the upper portion of Figure 3.5. All mechanism activities are triggered by software command from the instrument C&DH, and the limb scanning portions of both GHz and THz radiometers are synchronized to start on the same MIF. Although GHz and THz limb scans start simultaneously, it is necessary to stagger their ends slightly due to operational constraints on peak power, ripple current and disturbance torques imposed by the spacecraft. The nominal scan profile ends the THz limb scan approximately 1 s before that of the GHz.

The GHz module contains two ambient calibration targets, one at approximately the temperature of the surrounding structure, the other designed to float to a temperature $\sim$20 K lower than the structure, using a radiator for passive cooling. The floating target also contains heating elements which can be used to elevate the target temperature by $\sim$20 K. This target serves to provide an 'aliveness' check before launch without the need for an external target with an umbilical connection to the ground support equipment (GSE) system. This removes a limitation present during portions of integration of the UARS instrument with the spacecraft. Due to packaging constraints, there is only a single calibration target in the THz module.
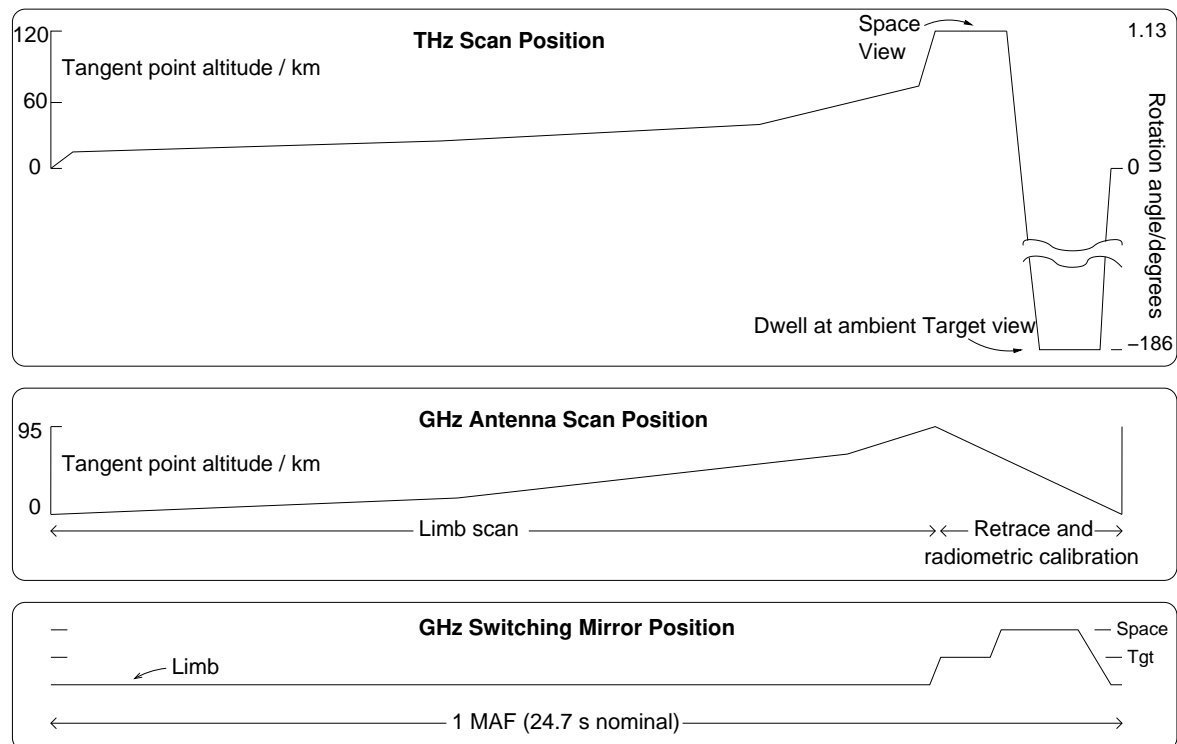
Figure 3.5: The top panel shows a nominal limb scan and calibration cycle for the THz scan mirror which also serves as the switching mirror for in-flight radiometric calibration. The center panel shows a nominal limb scan and retrace for the GHz antenna. The lower panel illustrates the use of the GHz switching mirror to provide in-flight radiometric calibration for all GHz radiometers by simultaneously directing their fields of view to an internal ambient calibration target, followed by a view to cold space. Drawings are not to scale, and are intended for illustration only.

Chapter 4

EOS MLS Level 1 data processing algorithms

4.1 Radiances

The MLS radiometers are heterodyne systems which receive power $h\nu/\{\exp(h\nu/kT)-1\}$ per unit frequency range when viewing a blackbody source at temperature T which completely fills their FOV, where ν is frequency, h is Planck's constant, and k is Boltzmann's constant (see Appendix B). The MLS signals originate thermally, and it is convenient to measure radiant power per unit bandwidth, $\dot{P}_\nu$, in units of temperature so that the measure converges to the absolute temperature, T, in the long wave (Rayleigh-Jeans) limit where $h\nu \ll kT$ and classical statistical mechanics applies. The dot above a symbol indicates a measured quantity. For the blackbody this is

$$\dot{P}_\nu^{BB} = \frac{h\nu}{k\{\exp(h\nu/kT) - 1\}} \tag{4.1}$$

The long wave expansion of this expression and values (in Kelvin) of the individual terms for various temperatures are given below for $\nu = 115\,\text{GHz}$, approximately the lowest frequency received by EOS MLS:

$$
\begin{array}{rclclclcl}
\dot{P}_\nu^{BB} & = & T & - & \frac{h\nu}{2k} & + & \left(\frac{h\nu}{2k}\right)^2 \frac{1}{3T} & \cdots \\
297.249 & = & 300 & - & 2.760 & + & 0.008 & \cdots \\
97.266 & = & 100 & - & 2.760 & + & 0.025 & \cdots \\
0.821 & = & 2.7 & - & 2.760 & + & 0.940 & \cdots
\end{array}
\tag{4.2}
$$

Temperatures of the atmospheric regions measured by the MLS, and of its internal calibration targets, are within the range $150 - 300\,\text{K}$, for which $\dot{P}_\nu^{BB} \approx T - \delta T$, where δT is a nearly temperature independent offset, different for each radiometer, increasing in magnitude as the frequency of observation increases. This behavior is readily apparent from Figure 4.1 which plots radiance versus blackbody temperature over the range 0 to $300\,\text{K}$ for frequencies corresponding to the nominal centers of the bandpasses of the 5 MLS radiometers. Values of δT for temperatures of 2.7, 150 and $300\,\text{K}$ at the center frequencies of all EOS MLS radiometers are given in Table 4.1. The full formula (4.1) is used throughout processing of MLS data.

Table 4.1: This table lists the differences, δT, between physical temperature, T, and received blackbody radiance per unit bandwidth (Kelvin). δT is computed at the nominal center frequencies of all EOS MLS radiometers, and at physical temperatures of 2.7, 150 and 300 K corresponding to the physical temperatures of 'cold space' and approximately the full range of observed temperatures.

$\nu/\,\mathrm{GHz}$	δT		
	$T = 2.7\,\mathrm{K}$	$T = 150\,\mathrm{K}$	$T = 300\,\mathrm{K}$
118	1.907	2.814	2.823
190	2.378	4.513	4.536
240	2.536	5.685	5.722
640	2.700	14.834	15.096
2,500	2.700	52.076	56.043
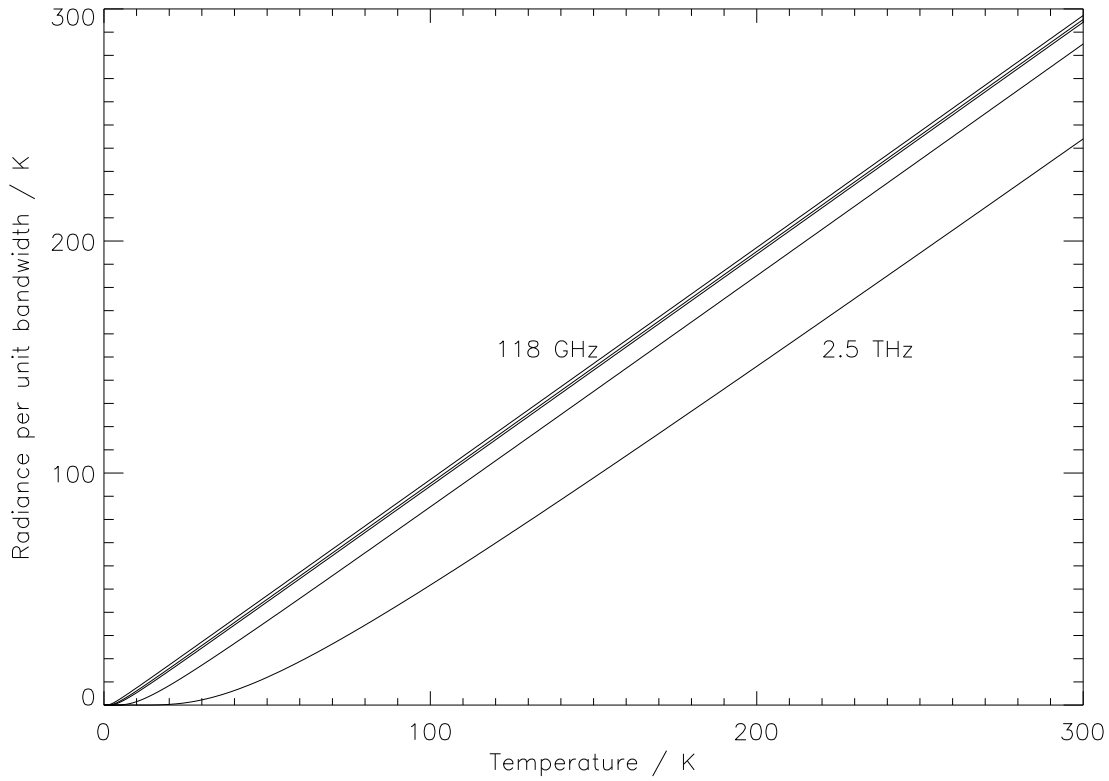
Figure 4.1: Plots of received blackbody radiance per unit bandwidth versus blackbody temperature over the temperature range 0 to 300 K at frequencies corresponding to the center frequencies of the 5 EOS MLS radiometers (118, 190, 240 and 640 GHz and 2.5 THz). The approximately linear relationship between physical temperature and radiance over the atmospheric temperature range ($\sim$150 to 300 K) is readily evident, as is the frequency-dependent offset.

4.1.1 Radiometric signals and the calibration process

MLS measures atmospheric limb radiances captured by the GHz and THz antennæ. For both subsystems regular periodic radiometric calibration is performed using switching mirrors. The operation of the 2 switching mirrors is independent, but synchronized at both the MIF and MAF level by the C&DH so that the start of limb scanning is coincident for both modules, and with slightly staggered (but overlapped) radiometric calibration sequences to meet spacecraft peak power, ripple current and disturbance torque requirements.

For both GHz and THz modules the use of a switching mirror for radiometric calibrations ensures that all radiometers within a module are calibrated concurrently, but in each case the measured radiances at the limb ports of the switching mirrors must be corrected for the FOV transformations and losses in the telescope optics. For the GHz module a 3 element offset Cassegrain telescope scans the atmosphere, directing this radiation into the limb port of the switching mirror. For the THz module the switching and atmospheric scanning mirrors are one and the same. In both cases the FOV response scanning the atmosphere will be characterized over a $\sim\pm6°$ angle from pre-launch FOV calibrations, and the much larger solid angle outside of this region will be characterized using scattering models. For the GHz FOV the $\pm6°$ region is a cone centered on the main response, while for the THz system this region is one dimensional (i.e., collapsed into a response in the vertical) because of the method used for its measurement.

Below we discuss radiometric response, effects introduced by the antenna, radiometric calibration using the switching mirror, and the impacts of noise on radiance measurements. Radiometric calibration of the DACS is discussed separately at the end of this chapter.

4.1.2 Radiometric Response

The response of radiometer filter channel i is proportional to received power $\overset{\bullet}{P}_i^{MX}$ obtained by integrating the power per unit frequency and per unit solid angle, $\overset{\bullet}{I}_\nu^{MX}(\theta, \phi)$, incident on the switching mirror (M) from view X, where X is one of L, T or S, representing the limb, target and space view ports respectively. The integrals are evaluated over angle and frequency with weighting functions $G^M(\nu, \theta, \phi)$ and $F_i(\nu)$ which describe the angular and frequency response of the antenna and radiometer respectively:

$$\overset{\bullet}{P}_i^{MX} = \frac{1}{4\pi} \int_\nu \int_\Omega \overset{\bullet}{I}_\nu^{MX}(\theta, \phi) F_i(\nu) G^M(\nu, \theta, \phi) \, d\Omega \, d\nu \tag{4.3}$$

where $F_i(\nu)$ is normalized to unit area ($\int_\nu F_i(\nu) d\nu = 1$), $\int_\Omega G d\Omega = 4\pi$ (Appendix B), and the integrals are evaluated over the full range of frequencies and solid angles over which the instrument has a response. For the THz radiometers the switching and antenna scanning mirrors are the same device. Level 1 software will report the estimated GHz and THz boresight angles at the center of each MIF, and it is the task of Level 2 processing to account for higher order effects such as FOV smearing during each data integration.

The following considerations are important in relating the radiation incident upon the switching mirror to that from the antenna, target, and space ports:

1. In the case of the GHz module, the views from the switching mirror are restricted by baffles, coated with absorbing material, which define solid angles Ω_{MX} for view X. We

define quantities $\overset{\bullet}{P}{}_i^X$ for $X = L$, T, or S from (4.3) by restricting the integral to the solid angle Ω_{MX}:

$$
\overset{\bullet}{P}{}_i^X = r_l \times \frac{\displaystyle\int_0^{\nu_{LO}} \int_{\Omega_{MX}} \overset{\bullet}{I}{}_\nu^X(\theta, \phi) F_i(\nu) G_{i,l}^M(\theta, \phi) \, d\Omega \, d\nu}{\displaystyle\int_{\Omega_{MX}} G_{i,l}^M(\theta, \phi) \, d\Omega} +
$$
$$
r_u \times \frac{\displaystyle\int_{\nu_{LO}}^\infty \int_{\Omega_{MX}} \overset{\bullet}{I}{}_\nu^X(\theta, \phi) F_i(\nu) G_{i,u}^M(\theta, \phi) \, d\Omega \, d\nu}{\displaystyle\int_{\Omega_{MX}} G_{i,u}^M(\theta, \phi) \, d\Omega}
$$

$$(\overset{\bullet}{I}{}_\nu^{MX} \equiv \overset{\bullet}{I}{}_\nu^X \text{ for directions within solid angle } \Omega_{MX})$$

(4.4)

where r_l and r_u are the radiometer relative responses for channel i in the lower and upper sidebands (lower sideband only for the single sideband 118 GHz radiometers), and use has been made of the fact that relative sideband response does not vary significantly over the spectral region measured by a spectrometer channel in one sideband. ν_{LO} is the frequency of the radiometer local oscillator. To reduce the complexity of Equation 4.4, and many of those which follow in this chapter, channel dependence of r_l and r_u is not called out explicitly.

2. The fractional ranges of ν over which the above integrands have significant magnitude are very small, allowing the dependence on ν to be removed from the expression for G^M when performing the integrals (i.e., constant values for ν corresponding to the center frequencies of the channel in each sideband are used when evaluating the integrals for each sideband).

3. Radiation $\overset{\bullet}{I}{}_\nu^X$ from the calibration target and from space is isotropic and has a black-body spectrum.

The restriction of the beam pattern by the baffles of the GHz switching mirror cavity is illustrated in Figure 4.2. The baffles are approximately elliptical in shape, and coated with microwave absorber. The most severe truncation is for the R1B 118 GHz radiometer for which ~ 0.993 of the power in the nominal beam passes through each of the three switching mirror port baffles. We represent baffle transmissions by the parameter η^{ML} where M signifies switching Mirror, and X indicates the three ports (Target, Space or Limb). With the above definitions, for the limb view,

$$
\overset{\bullet}{P}{}_i^{ML} = r_l \times \left(\eta_{i,l}^{ML} \overset{\bullet}{P}{}_{i,l}^L + (1 - \eta_{i,l}^{ML}) \overset{\bullet}{P}{}_{i,l}^{BL} \right) + r_u \times \left(\eta_{i,u}^{ML} \overset{\bullet}{P}{}_{i,u}^L + (1 - \eta_{i,u}^{ML}) \overset{\bullet}{P}{}_{i,u}^{BL} \right)
$$
(4.5)

where $\eta_{i,s}^{ML} = \frac{1}{4\pi} \int_{\Omega_{ML}} G_i^M(\theta, \phi) \, d\Omega$ is the fraction of the 'volume' under the gain pattern which is inside Ω^{ML}, and $\overset{\bullet}{P}{}_{i,s}^{BL}$ is the radiation from the baffle in the limb view, averaged over the solid angle outside Ω_{ML}, for sideband s. $\overset{\bullet}{P}{}_{i,s}^L$ is the appropriate sideband component
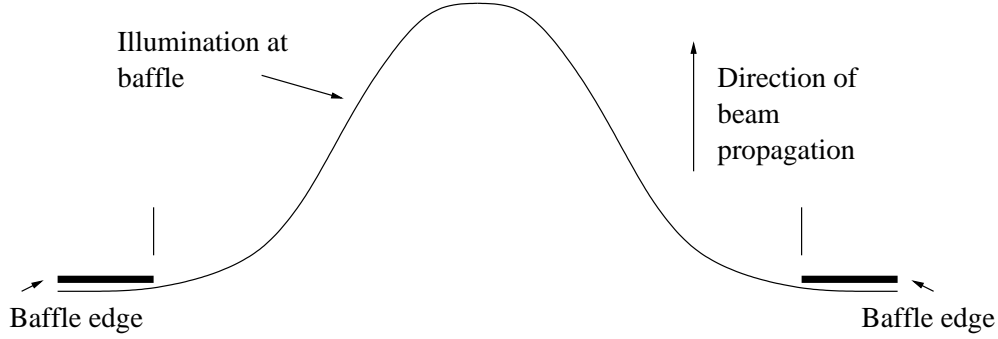
Figure 4.2: Truncation of beam pattern by the baffles of the GHz switching mirror cavity. A cross section through the center of the approximately elliptical cavity port is shown.

from the right hand side of Equation 4.4, thus accounting for the relative sideband response of the radiometer. Similarly, for the target $(X = T)$ and space $(X = S)$ views,

$$\overset{\bullet}{P}_i^{MX} = r_l \times \left(\eta_{i,l}^{MX} \overset{\bullet}{P}_{i,l}^{X} + (1 - \eta_{i,l}^{MX}) \overset{\bullet}{P}_{i,l}^{BX} \right) + r_u \times \left(\eta_{i,u}^{MX} \overset{\bullet}{P}_{i,u}^{X} + (1 - \eta_{i,u}^{MX}) \overset{\bullet}{P}_{i,u}^{BX} \right) \quad (4.6)$$

where $\eta_{i,s}^{MX}$ and $\overset{\bullet}{P}_{i,s}^{BX}$ are the corresponding values for these two views, and $\overset{\bullet}{P}_{i,s}^{X} = \overset{\bullet}{P}_{\nu_{i,s}}^{X}$.

4.1.3 Antenna Effects

The radiance intercepted by the switching mirror when viewing the limb consists of not just the desired atmospheric limb radiance, but also components arising from antenna emission, diffraction and scattering. In addition, the limb radiance itself is attenuated due to losses in the antenna system. For the THz system, which uses the same mirror for both switching (calibration) and limb scanning, the situation is simpler. We discuss the more complex GHz case in detail below.

The GHz antenna, interposed between the switching mirror and the atmospheric limb, transforms the FOV of the radiometer so that when calculating the radiance collected by the antenna, $\overset{\bullet}{P}_i^A$, from the limb spectral intensity incident upon the antenna, $\overset{\bullet}{I}_\nu^A(\theta, \phi)$, $G_i^M(\theta, \phi)$ must be replaced by $G_i^A(\theta, \phi)$, the measured antenna gain. Imperfections in the antenna and practical limitations on its characterization result in the introduction of further terms. One limitation is that $G_i^A(\theta, \phi)$ is measured only over directions included in a solid angle Ω_A, about $\pm 6°$ from the boresight axis. The calculated response for directions outside this range, and the calculated ohmic loss in the antenna, are used to estimate an effective transmission loss of the radiation received within Ω_A and an additive radiation offset from the antenna.

Antenna transmission is more easily described by considering the antenna as a transmitter with illumination function $G_i^A(\theta, \phi)$ (restricted to solid angle Ω_A). Two processes are involved:

1. Ohmic loss: the antenna transmission due to ohmic loss is ρ_r^A where a fraction $(1 - \rho_r^A)$ of the incident radiation is absorbed, and

2. diffraction and scattering: of the remainder, in any narrow frequency band a fraction

$(1-\eta^A)$ is transmitted into directions outside the solid angle Ω_A over which the antenna pattern is characterized in detail.

Antenna ohmic loss, ρ^A, varies sufficiently slowly with frequency that a single value suffices for each radiometer r. Antenna efficiency, η^A, however, has sufficient frequency dependence that we must provide values for each channel i and sideband s, where

$$\eta_{i,s}^A = \frac{1}{4\pi} \int_{\Omega_A} G_{i,s}^A(\theta, \phi)\, d\Omega \tag{4.7}$$

Radiation offsets arise from the same two processes: (1) ohmic loss: radiation $(1-\rho_r^A)\overset{\bullet}{P}_{i,s}^{OA}$ is emitted by the antenna, where $\overset{\bullet}{P}_{i,s}^{OA}$ is an effective brightness for the antenna thermal emission; (2) diffraction and scattering: radiation $(1 - \eta_{i,s}^A)\rho_r^A \overset{\bullet}{P}_{i,s}^{SA}$, characterized by an effective brightness $\overset{\bullet}{P}_{i,s}^{SA}$, is scattered outside solid angle Ω_A.

Accounting for loss and scattering as described above relates $\overset{\bullet}{P}_i^L$, the radiance at the limb port of the switching mirror, to $\overset{\bullet}{P}_{i,l}^A$ and $\overset{\bullet}{P}_{i,u}^A$, the radiance collected by the antenna within solid angle Ω_A for the two sidebands:

$$\begin{aligned}
\overset{\bullet}{P}_i^L &= \rho_r^A(r_l'\eta_{i,l}^A \overset{\bullet}{P}_{i,l}^A + r_u'\eta_{i,u}^A \overset{\bullet}{P}_{i,u}^A) + \\
&\quad r_l'(1-\rho_r^A)\overset{\bullet}{P}_{i,l}^{OA} + r_u'(1-\rho_r^A)\overset{\bullet}{P}_{i,u}^{OA} + r_l'(1-\eta_{i,l}^A)\rho_r^A \overset{\bullet}{P}_{i,l}^{SA} + r_u'(1-\eta_{i,u}^A)\rho_r^A \overset{\bullet}{P}_{i,u}^{SA}
\end{aligned} \tag{4.8}$$

where

$$\begin{aligned}
r_l &= r_l'\eta_{i,l}^A \\
\text{and} \quad r_u &= r_u'\eta_{i,u}^A
\end{aligned} \tag{4.9}$$

are the lower and upper sideband responses through the entire signal chain including antenna effects, whereas r_l' and r_u' are the sideband responses for the radiometers and optics up to the radiometer port of the switching mirror. The quantities r_l' and r_u', normalized according to

$$r_l' + r_u' = 1 \tag{4.10}$$

are measured during spectral calibration of the instrument, while $\eta_{i,s}^A$ are determined during FOV calibration.

Calculated values of $\overset{\bullet}{P}_i^A$ are produced during Level 2 processing in a Forward Model (where they are designated $\overset{\star}{P}_i^A$) by integrating $\overset{\bullet}{I}_\nu^A(\theta, \phi)$ over the angular response of the antenna within solid angle Ω_A and over the frequency response of a radiometer channel, where

$$\overset{\star}{P}_i^A = \frac{\displaystyle\int_\nu \int_{\Omega_A} \overset{\bullet}{I}_\nu^A(\theta, \phi) F_i(\nu) G_i^A(\nu, \theta, \phi)\, d\Omega\, d\nu}{\displaystyle\int_{\Omega_A} G_i^A(\theta, \phi)\, d\Omega} \tag{4.11}$$

It is important to note that $\overset{\star}{P}_i^A$ is computed separately for both sidebands of each radiometer (except for the single sideband 118 GHz radiometers), which allows the frequency dependence of G to be removed from the integrals by substituting the value for ν in the center of channel i in each measurement sideband. These components are then combined appropriately using the radiometer sideband responses to produce the Forward Model quantity $\overset{\star}{P}_i^A$ given by

$$
\overset{\star}{P}{}^A_i \;=\; r_l \times \frac{\displaystyle\int_0^{\nu_{LO}} \int_{\Omega_A} \overset{\bullet}{I}{}^A_\nu(\theta,\phi) F_i(\nu) G^A_{i,l}(\theta,\phi)\, d\Omega\, d\nu}{\displaystyle\int_{\Omega_A} G^A_{i,l}(\theta,\phi)\, d\Omega} \;+\; \tag{4.12}
$$

$$
r_u \times \frac{\displaystyle\int_{\nu_{LO}}^{\infty} \int_{\Omega_A} \overset{\bullet}{I}{}^A_\nu(\theta,\phi) F_i(\nu) G^A_{i,u}(\theta,\phi)\, d\Omega\, d\nu}{\displaystyle\int_{\Omega_A} G^A_{i,u}(\theta,\phi)\, d\Omega}
$$

The Forward Model calculations of $\overset{\star}{P}{}^A_i$ include the effects of vertical smearing due to motion of the FOV during the limb data integration by including the time dependence in the FOV direction of G. This does not affect any of the derivations below and, to improve clarity in discussion of the key points, we do not include this time dependence here or later in this chapter.

4.2 The interface between Level 1 and Level 2

The relatively narrow IF bandwidths and low overall fractional bandwidth of UARS MLS measurement bands allowed the Level 1 and level 2 estimates of limb radiance to be reconciled by:

$$
\begin{aligned}
\langle \overset{\bullet}{P}{}^A_i \rangle \;&=\; r_l \overset{\bullet}{P}{}^A_{i,l} + r_u \overset{\bullet}{P}{}^A_{i,u} \tag{4.13}\\[4pt]
&=\; \frac{\overset{\bullet}{P}{}^L_i}{\rho^A_r} - \left(\frac{1}{\rho^A_r} - 1 \right)\left(r'_l \overset{\bullet}{P}{}^{OA}_{i,l} + r'_u \overset{\bullet}{P}{}^{OA}_{i,u} \right) - r'_l (1 - \eta^A_{i,l}) \overset{\bullet}{P}{}^{SA}_{i,l} - r'_u (1 - \eta^A_{i,u}) \overset{\bullet}{P}{}^{SA}_{i,u}
\end{aligned}
$$

where the Level 1 estimate of $\overset{\bullet}{P}{}^A_i$ is given by $\langle \overset{\bullet}{P}{}^A_i \rangle$, which corresponds to $\overset{\star}{P}{}^A_i$ in Equation 4.12.

For the current instrument, with its significantly larger fractional measurement bandwidths and sideband separations, we cannot make the UARS approximation of assuming that $\overset{\bullet}{P}{}^A_{i,l}$ and $\overset{\bullet}{P}{}^A_{i,u}$ can be evaluated at the LO frequency of each double-sideband radiometer without the introduction of unacceptable errors. In other words, it is not possible for Level 1 processing to accurately estimate the *atmospheric* contribution to limb port radiance. In addition, the relative computation times for Level 1 and Level 2 processing are quite disparate, with Level 2 requiring hundreds of processors to complete the processing of a daily data set in a reasonable time-frame. For these reasons we have chosen to have the interface between the processing levels be the estimate of radiance at the Limb port of the GHz radiometer, and for Level 1 to evaluate the radiance contribution from antenna emission and scattering.

This is summarized in Equation 4.14, where the left hand side is evaluated by Level 1 software, and the right hand side by Level 2:

$$
\langle \overset{\bullet}{P}{}^A_i \rangle + \left(\frac{1}{\rho^A_r} - 1 \right)\left(r'_l \overset{\bullet}{P}{}^{OA}_{i,l} + r'_u \overset{\bullet}{P}{}^{OA}_{i,u} \right) + r'_l (1 - \eta^A_{i,l}) \overset{\bullet}{P}{}^{SA}_{i,l} + r'_u (1 - \eta^A_{i,u}) \overset{\bullet}{P}{}^{SA}_{i,u} = \frac{\overset{\bullet}{P}{}^L_i}{\rho^A_r} \tag{4.14}
$$

We now expand the first term in Equation 4.14 to explicitly include separate terms for the three reflectors in the GHz antenna system, as these will be explicitly accounted for in

Level 1 processing to improve accuracy in the absolute values of calibrated MLS radiances. This expansion leads to:

$$\langle \overset{\bullet}{P}{}_i^A \rangle = \frac{\overset{\bullet}{P}{}_i^L}{\rho_r^1 \rho_r^2 \rho_r^3} - \alpha_r \tag{4.15}$$

where

$$
\begin{aligned}
\alpha_r \;=\; \{ r_l' \times (\;\; & \rho_r^1 \rho_r^2 \rho_r^3 (1 - \eta_{i,l}^{AA}) \eta_{i,l}^1 \overset{\bullet}{P}{}_{i,l}^{SA} + (1 - \rho_r^1) \rho_r^2 \rho_r^3 \eta_{i,l}^1 \overset{\bullet}{P}{}_{i,l}^{O1} \\
+ & \rho_r^2 \rho_r^3 (\eta_{i,l}^2 - \eta_{i,l}^1) \overset{\bullet}{P}{}_{i,l}^{S1} + (1 - \rho_r^2) \rho_r^3 \eta_{i,l}^2 \overset{\bullet}{P}{}_{i,l}^{O2} \\
+ & \rho_r^3 (\eta_{i,l}^3 - \eta_{i,l}^2) \overset{\bullet}{P}{}_{i,l}^{S2} + (1 - \rho_r^3) \eta_{i,l}^3 \overset{\bullet}{P}{}_{i,l}^{O3} \\
+ & (1 - \eta_{i,l}^3) \overset{\bullet}{P}{}_{i,l}^{S3} \Big) \\
+ r_u' \times (\;\; & \rho_r^1 \rho_r^2 \rho_r^3 (1 - \eta_{i,u}^{AA}) \eta_{i,u}^1 \overset{\bullet}{P}{}_{i,u}^{SA} + (1 - \rho_r^1) \rho_r^2 \rho_r^3 \eta_{i,u}^1 \overset{\bullet}{P}{}_{i,u}^{O1} \\
+ & \rho_r^2 \rho_r^3 (\eta_{i,u}^2 - \eta_{i,u}^1) \overset{\bullet}{P}{}_{i,u}^{S1} + (1 - \rho_r^2) \rho_r^3 \eta_{i,u}^2 \overset{\bullet}{P}{}_{i,u}^{O2} \\
+ & \rho_r^3 (\eta_{i,u}^3 - \eta_{i,u}^2) \overset{\bullet}{P}{}_{i,u}^{S2} + (1 - \rho_r^3) \eta_{i,u}^3 \overset{\bullet}{P}{}_{i,u}^{O3} \\
+ & (1 - \eta_{i,u}^3) \overset{\bullet}{P}{}_{i,u}^{S3} \Big) \} \\
& / (\rho_r^1 \rho_r^2 \rho_r^3),
\end{aligned}
\tag{4.16}
$$

and i,s indicate channel i, sideband s (l or u), r indicates radiometer r, and where

$$
\begin{aligned}
\overset{\bullet}{P}{}_{i,s}^L \;\; &= \;\; \text{limb port radiance power,} \\
\rho_r^k \;\; &= \;\; \text{reflectivity of reflector } k = 1,\,2,\,3 \text{ (primary, secondary, tertiary),} \\
\eta_{i,s}^{AA} \;\; &= \;\; \text{optical transmission of the antenna system: the product of scattering } (\eta_{i,s}^{AS}) \\
&\qquad \text{and diffraction } (\eta_{i,s}^{AD}) \text{ from the primary plane,} \\
\eta_{i,s}^k \;\; &= \;\; \text{optical transmission of reflector } k, \\
\overset{\bullet}{P}{}_{i,s}^{SA} \;\; &= \;\; \text{radiance power in the limb hemisphere but outside FOV measurement angle} \\
&\qquad \Omega_A, \\
\overset{\bullet}{P}{}_{i,s}^{Sk} \;\; &= \;\; \text{radiance power illuminating the spillover solid angle for reflector } k, \text{ and} \\
\overset{\bullet}{P}{}_{i,s}^{Ok} \;\; &= \;\; \text{power thermally emitted by reflector } k.
\end{aligned}
$$

At the time of launch we have chosen not to include the expanded formulation for α_r shown above, but to amalgamate the antenna emission estimates from the three antenna reflectors into a simpler expression using a mean of the reflector temperatures, and mean reflector emissivities. During the instrument activation period we have included special scan and switching sequences designed specifically to provide additional information regarding baffle transmissions and antenna properties (including emission and scattering components). After data from this period has been thoroughly evaluated, any necessary changes will be made to Level 1 software and this document.

The next section of this document describes how $\overset{\bullet}{P}{}_i^L$ appearing in Equation 4.15 is obtained during in-flight radiometric calibration of the instrument. The quantities ρ_r^k, $\eta_{i,s}^{AA}$ and $\eta_{i,s}^k$ appearing in Equations 4.15 and 4.16 are produced during instrument FOV calibration. Precalculated values are used for $\overset{\bullet}{P}{}_{i,s}^{SA}$ and $\overset{\bullet}{P}{}_{i,s}^{Sk}$. $\overset{\bullet}{P}{}_{i,s}^{Ok}$ is calculated from temperatures measured by sensors on the appropriate reflectors.
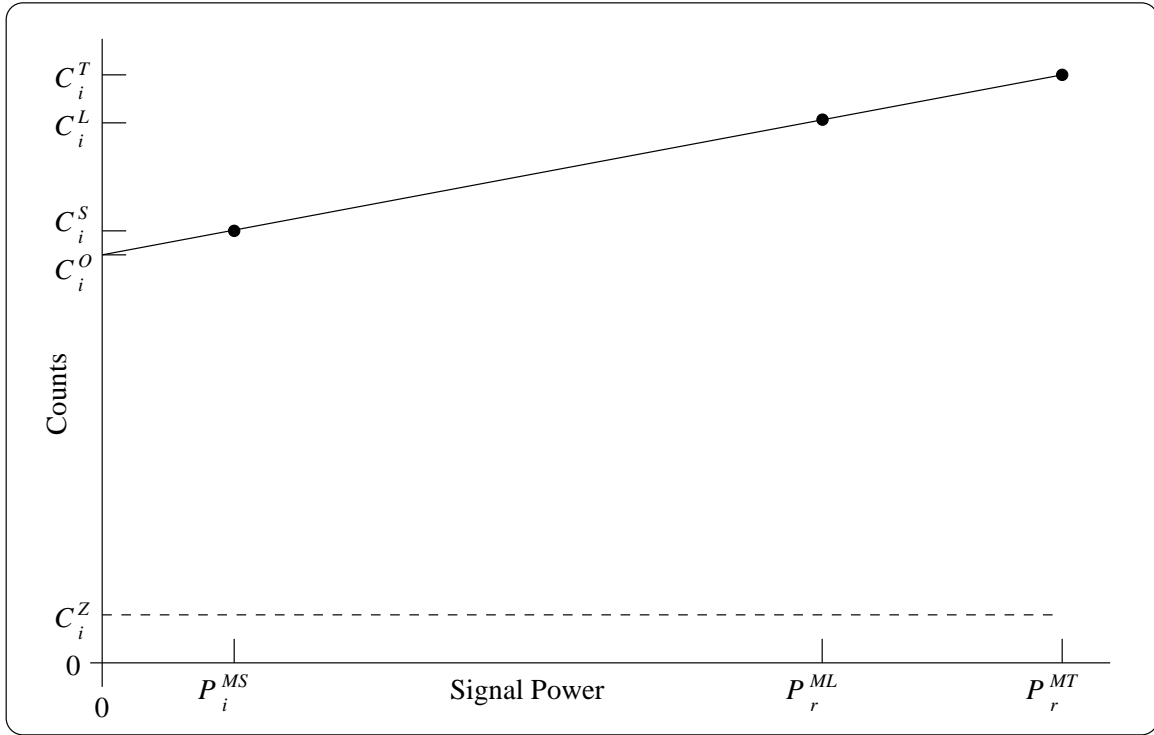
Figure 4.3: Plot illustrating the linear relationship between filterbank channel digitized output (counts) and power collected by the switching mirror. S, A and T correspond to the space, limb (antenna) and target views of the switching mirror respectively. C_i^O is the offset generated by instrument noise, and C_i^Z is the offset built into the digitizing system.

4.2.1 The radiance calibration process

In-flight radiometric calibration is performed during every limb scan using the switching mirror (scanning mirror in the case of the THz module) to direct the FOVs of all radiometers to the space and internal calibration target ports. The filterbank detectors are operated at sufficiently low signal power to provide a linear relationship between input radiance and channel output, illustrated in Figure 4.3, where the abscissa indicates signal power collected by the switching mirror, and the ordinate indicates the output counts from the voltage-to-frequency (V/F) converter digitizer of an individual channel i. The discussion below applies to all filter spectrometer channels, including the single filter channel implemented in each DACS as a signal power monitor.

In the formulation below, the sideband dependence of the receivers and of the baffle transmissions (shown in Equation 4.5) is omitted, since the error introduced by this approximation is negligible.

The output of channel i for each of the three switching mirror positions is given by:

$$
\begin{aligned}
C_i^L &= g_i\left(\eta_r^{ML}\overset{\bullet}{P}_i^L + (1-\eta_r^{ML})\overset{\bullet}{P}_r^{BL}\right) + C_i^O + C_i^Z, \\
C_i^T &= g_i\left(\eta_r^{MT}\overset{\bullet}{P}_r^T + (1-\eta_r^{MT})\overset{\bullet}{P}_r^{BT}\right) + C_i^O + C_i^Z, \\
C_i^S &= g_i\left(\eta_r^{MS}\overset{\bullet}{P}_r^S + (1-\eta_r^{MS})\overset{\bullet}{P}_r^{BS}\right) + C_i^O + C_i^Z.
\end{aligned}
\tag{4.17}
$$

where C_i^X are the outputs of channel i for the three switching mirror positions X. C_i^O are the counts that would be generated if observed radiances were zero (i.e., generated by radiometer and IF noise alone), and g_i is the overall radiometric gain of channel i (expressed in counts per Kelvin of signal brightness). C_i^Z are the offsets built into the spectrometer digitization system, measured nominally once per orbit to facilitate determination of system temperature (described later) as a diagnostic of radiometer performance. The measurement of C_i^Z is performed by commanding the IF gains of all radiometers to such a low value that the spectrometers see essentially no RF signal at their inputs. Although counts C_i^O are shown the same for all views in Equation 4.17, it must be noted that this offset is time dependent due to thermal drifts and noise, and that its power spectrum invariably displays some form of $\frac{1}{f}$ dependence, usually over the timescales of radiometric calibrations for this instrument. Another important fact to note is that C_i^O dominates the digitized signal because system temperatures in all radiometers exceed the temperature of any radiometric source. One of the most crucial aspects of the radiometric calibration data processing is thus the interpolation of reference counts (C_i^S and C_i^T) necessary for estimating channel reference counts and gains at the times of the limb views, since this must be done in a manner which reduces the variance (noise) on the interpolated quantities without the introduction of bias. Of particular concern are the low frequency variations in signal path gain which tend to have a $\frac{1}{f}$ characteristic. These issues are discussed later.

4.3 Radiance calibration algorithms

Radiance calibration of each filter channel is a straightforward process in which Space and Target counts are interpolated onto the times of Limb measurements. The radiometric gain and random component of uncertainty is then computed for each limb view, and after a complete MAF of data has been processed as just described, an estimate of the spectrally flat component for each radiometer is generated. The above steps are now discussed further, followed by a description of the radiance calibration algorithms used with the DACS data.

Channel gain at the time of a limb view, $\hat{g}_i(L)$, is estimated by

$$
\hat{g}_i(L) = \frac{\widehat{C}_i^T(L) - \widehat{C}_i^S(L)}{\left(\eta_r^{MT}\epsilon_r\overset{\bullet}{P}_r^T - \eta_r^{MS}\overset{\bullet}{P}_r^S - (1-\eta_r^{MT})\overset{\bullet}{P}_r^{BT} + (1-\eta_r^{MS})\overset{\bullet}{P}_r^{BS}\right)}
\tag{4.18}
$$

where the 'radiation offset' terms in the denominator involving $\overset{\bullet}{P}_r^{BT}$ and $\overset{\bullet}{P}_r^{BS}$ are provided from FOV calibrations. The calibration target emissivity is indicated by ϵ_r (>0.999 in all GHz and THz bands). Temperature sensors on the ambient calibration targets, switching mirror baffle structures, and antenna reflectors allow all $\overset{\bullet}{P}$ quantities in the above expression to be determined from instrument engineering data. The estimated Space and Target reference

counts at the times of each Limb view, $\widehat{C}_i^S(L)$ and $\widehat{C}_i^T(L)$, are provided by interpolation using a weighted quadratic fit over the calibration window (with the MAF at the center of the sequence containing the limb data being processed). Solving the first and third of equations (4.17) for $\overset{\bullet}{P}_i^L$, and using $\hat{g}_i(L)$ for g_i, gives

$$\overset{\bullet}{P}_i^L = \frac{1}{\eta_r^{ML}} \left(\frac{C_i^L - \widehat{C}_i^S(L)}{\hat{g}_i(L)} + \eta_r^{MS} \overset{\bullet}{P}_r^S - (1 - \eta_r^{ML}) \overset{\bullet}{P}_r^{BL} + (1 - \eta_r^{MS}) \overset{\bullet}{P}_r^{BS} \right) \tag{4.19}$$

where $\widehat{C}_i^S(L)$ is the previously-determined interpolated value of the space counts at the time of the limb view.

4.4 Interpolation of Reference Measurements

The performance of the radiance calibration algorithms described earlier is highly dependent upon the manner in which the interpolated reference counts, $\widehat{C}_i^S(L)$ and $\widehat{C}_i^T(L)$, are determined. Further discussion of this topic is given in Appendix E. Below we discuss further the interpolation of Space reference counts, and the same interpolation scheme is used to estimate Target counts at the times of Limb views. The chosen method is to perform a quadratic least squares fit (as a function of MIF number) to a sequence of reference measurement groups disposed as symmetrically as possible about the MIF for which the interpolate is being calculated. The interpolations are performed on raw data counts from the filter spectrometer channels. The noise, ΔC_i, on each individual measurement is given by the radiometer equation:

$$\Delta C_i = \frac{(C_i^S - C_i^Z)}{\sqrt{B_i \tau}} \tag{4.20}$$

where:

$\quad i$ is the channel index,

$\quad C_i^S$ is the value, in counts, of the raw reference measurement,

$\quad C_i^Z$ is the value, in counts, of the offset built into the digitizer system (see Section 4.2.1),

$\quad B_i$ is the predetection noise bandwidth in Hz, and

$\quad \tau$ is the postdetection integration time in seconds.

Values of B_i are provided for each channel from prelaunch calibrations, and τ is determined directly from telemetry. The digitizer offsets, C_i^Z, are known from prior (UARS) experience to be a stable quantity, and the effects of small errors in their values have negligible impact upon the calibrated limb radiances and associated uncertainty estimates. Since they do not provide essential science data, their values will only be measured periodically for diagnostic purposes (once per month), and the last measured valid values of these quantities are adequate for Level 1 computational purposes.

Equation 4.20 provides a reliable estimate of the rms noise on an individual reference measurement, but we must also include the uncertainties in interpolated space reference and radiometric gain. This is discussed later in this chapter. In practice there will be a small additional component of noise arising from gain variations common to all channels of a given radiometer. The most important manifestation of this additional source of noise arises when computing the rms of a time series of data, where it is seen that the ratio of measured to

expected rms rises above unity as the duration of the time series extends. It is also seen when fitting a quadratic to a time series of measurement as described earlier for space reference interpolation, where the χ^2 for the fit increases from unity as the calibration window duration is increased. The effects of this noise are diminished by providing less weight to reference measurements that are more distant from the interpolation point. These topics are discussed in more detail in Appendix C and D where it is pointed out:

(1) that a common weighting (apodizing) function must be used for all channels whose calibrated radiance data is to be used together in higher level analyses, and

(2) for the range of planned EOS MLS in-orbit operating modes there is only a very weak dependence on the actual form of the weighting function for the calculated radiances and uncertainties.

4.4.1 Reference interpolation details

To the space reference count sequence from each channel we fit the function

$$\widehat{C}^S(t) = a + b \times t + c \times t^2 \tag{4.21}$$

where the channel index i has been dropped for clarity. In practice we replace t by an integer index (corresponding to relative MIF location, indicated by j below) when performing the quadratic fit. The same method is used to interpolate target reference counts. The best-fit coefficients are given by the standard relationships:

$$a = \frac{1}{\Delta} \begin{vmatrix} \Sigma \frac{C(j)}{\sigma^2(j)} & \Sigma \frac{j}{\sigma^2(j)} & \Sigma \frac{j^2}{\sigma^2(j)} \\ \Sigma \frac{jC(j)}{\sigma^2(j)} & \Sigma \frac{j^2}{\sigma^2(j)} & \Sigma \frac{j^3}{\sigma^2(j)} \\ \Sigma \frac{j^2C(j)}{\sigma^2(j)} & \Sigma \frac{j^3}{\sigma^2(j)} & \Sigma \frac{j^4}{\sigma^2(j)} \end{vmatrix} \tag{4.22}$$

$$b = \frac{1}{\Delta} \begin{vmatrix} \Sigma \frac{1}{\sigma^2(j)} & \Sigma \frac{C(j)}{\sigma^2(j)} & \Sigma \frac{j^2}{\sigma^2(j)} \\ \Sigma \frac{j}{\sigma^2(j)} & \Sigma \frac{jC(j)}{\sigma^2(j)} & \Sigma \frac{j^3}{\sigma^2(j)} \\ \Sigma \frac{j^2}{\sigma^2(j)} & \Sigma \frac{j^2C(j)}{\sigma^2(j)} & \Sigma \frac{j^4}{\sigma^2(j)} \end{vmatrix} \tag{4.23}$$

$$c = \frac{1}{\Delta} \begin{vmatrix} \Sigma \frac{1}{\sigma^2(j)} & \Sigma \frac{j}{\sigma^2(j)} & \Sigma \frac{C(j)}{\sigma^2(j)} \\ \Sigma \frac{j}{\sigma^2(j)} & \Sigma \frac{j^2}{\sigma^2(j)} & \Sigma \frac{jC(j)}{\sigma^2(j)} \\ \Sigma \frac{j^2}{\sigma^2(j)} & \Sigma \frac{j^3}{\sigma^2(j)} & \Sigma \frac{j^2C(j)}{\sigma^2(j)} \end{vmatrix} \tag{4.24}$$

and

$$\Delta = \begin{vmatrix} \Sigma \frac{1}{\sigma^2(j)} & \Sigma \frac{j}{\sigma^2(j)} & \Sigma \frac{j^2}{\sigma^2(j)} \\ \Sigma \frac{j}{\sigma^2(j)} & \Sigma \frac{j^2}{\sigma^2(j)} & \Sigma \frac{j^3}{\sigma^2(j)} \\ \Sigma \frac{j^2}{\sigma^2(j)} & \Sigma \frac{j^3}{\sigma^2(j)} & \Sigma \frac{j^4}{\sigma^2(j)} \end{vmatrix} \tag{4.25}$$

where the summations are over j, the time indexes of the measurements. In these relationships the quantity $\sigma(j)$ is the rms noise on the measured reference value $C(j)$ at 'time' j. In the absence of any apodization or weighting σ is the same as the expected radiometer

noise on individual reference integrations, given by Equation 4.20. To attenuate the effects of signal drifts due to temperature and gain variations we choose to weight each measurement with an exponential roll-off $w_r(j)$ given by

$$w_r(j) = e^{-\left(\frac{|\delta j|}{\lambda_r}\right)} \tag{4.26}$$

where δj is the time difference between interpolation point and reference measurement j.

The parameter λ_r sets the rate at which the relative weighting given to a particular measurement drops off with its distance (time) from the interpolation point. Optimal values of λ_r will be determined from ground tests and in-flight data, and read by Level 1 software as user inputs. A nominal value of 150 MIFs has been selected initially which provides an order of magnitude reduction in weighting for the most distant reference measurements compared to the closest ones for the nominal scan/switching profile. We combine these weightings with the noise levels given by Equation 4.20 to obtain a modified estimate of the noise contribution from each measurement given by σ' where:

$$\sigma'(j) = \frac{\sigma(j)}{w_r(j)} = \frac{(C_i^S - C_i^Z)}{w_r(j)\sqrt{B_i\tau}} \tag{4.27}$$

This modified value of $\sigma'(j)$ is used in place of $\sigma(j)$ when performed the quadratic fit via Equations 4.22 through 4.25

4.4.2 Limitations of the quadratic interpolator

The quadratic fit used for reference and gain interpolation performs extremely well under nominal operating conditions, as demonstrated on UARS MLS, but can exhibit well-known minor shortcomings under certain conditions:

1. The quality of the fit is strongly influenced by bad data.

2. When used as an extrapolator, the quadratic fit exhibits large uncertainties.

The first of these deficiencies is handled by trapping bad data points and excluding them from the fit. This is done by initially excluding data which are outside prescribed limits (set by user inputs), and then rejecting data points which lie more than 6σ from a preliminary quadratic fit on the remaining data. This technique was used successfully on UARS MLS. The second issue is not actively addressed in this software for the following reason: the only condition under which the quadratic fit is used to generate an interpolate at or near one extreme of its temporal extent is when the edge of a calibration window approaches the MAF currently being processed. This will occur typically only when a gain change is commanded or a radiometer is turned on or off. Commanded gain changes have only occurred twice in the ~10 years of UARS MLS operation to date, and are not expected much more frequently on EOS MLS. Mode changes which turn radiometers on or off are planned to take place on time intervals of at least several weeks, and will be followed by a warm up period lasting several hours before science data is stable enough to be of value to Level 2, which makes the brief increase in uncertainty largely irrelevant. We thus anticipate operating the quadratic interpolator in a mode in which it exhibits relatively large errors so rarely, and for such brief intervals, that the loss in data quality will be negligible. It should be noted that when the quadratic interpolator is being operated in a mode that exhibits larger than typical uncertainties, these will be reported correctly to Level 2.

4.5   Radiance uncertainties

Appendix C provides a detailed description of noise and the calibration process as it pertains to EOS MLS, and Appendix E provides expressions for measurement covariances when the noise power spectrum contains both white and $\frac{1}{f}$ components. Radiance information in the calibrated bands output by Level 1 software is used in two distinct ways during Level 2 processing, and it is necessary to determine and catalog radiance uncertainties accordingly.

Most retrievals at Level 2 depend mainly upon the spectral contrast in one or more bands, and these results are only weakly affected by errors or uncertainties in the average values (offsets) of these radiances. For these retrievals the most important uncertainties are those which introduce channel-to-channel noise. This noise component arises from radiometer noise present on both limb and reference measurements, and the effects of gain variations are minor in comparison. We refer to this class of error as relative radiance uncertainty.

Several important measurements, particularly water vapor in the upper troposphere, are retrieved from broad spectral regions covered by a combination of one or more standard filterbanks and several broad filter channels. There are no strong spectral features in these measurements, and the dominant source of information arises from the absolute radiances in the measured spectrum. In the calculation of the relative radiance uncertainties discussed above we take care not to include the absolute uncertainty component arising from gain variations, making it necessary to compute them separately. The correlated uncertainties arise from gain variations in the front-end receivers and HEMT IF amplifiers common to all channels of each radiometer.

The methods of calculating relative and absolute radiance uncertainties are given below. Note that these uncertainties reflect only the contributions from noise on the data integrations, not systematic uncertainties due to errors in, for example, baffle transmissions or other optical properties. The algorithms for calculating the relative uncertainties reflect the method used for reference interpolation, and are modified from those used in UARS data processing only to reflect the minor differences between the two instruments (i.e., variable length MAF, different calibration sequence details). The uncertainties generated by these algorithms, as well as the radiances themselves, were validated as part of UARS Level 1 processing validation using the Optimal Calibrator (Appendix E) for comparison. Results from both methods are virtually indistinguishable, the algorithms given below producing a slightly lower estimate of uncertainty than the Optimal Calibrator, as is to be expected. Of more importance are the radiances themselves, where results from binning of zonal mean ClO data have produced undistorted spectra with channel-to-channel radiance differences of $\sim 0.001\,\mathrm{K}$, a dynamic range of 1 part in 10^6. This result strongly validates the use of the quadratic interpolator.

4.5.1   Relative radiance uncertainties

It is shown in Appendix C that the uncertainty in relative radiance, ΔT_{rel}, is given by

$$\Delta T_{rel} = \sqrt{\frac{(T_{sys} + T_{sig})^2}{B\tau} + (\Delta R)^2 + \left(T_{sig} \times \frac{\Delta g}{g}\right)^2} \qquad (4.28)$$

which combines in quadrature three separate noise terms, discussed further below. It is important to note that the right hand term inside the square root includes the noise from

just the spectral contrast (limb radiance) and gain uncertainty. The uncertainty derived for the total signal (limb plus system) and gain uncertainty is determined separately and book kept under absolute radiance uncertainty, discussed later in this chapter.

Radiometer noise contribution

The first term inside the square root of Equation 4.28 is simply the noise on an individual limb radiance, given by the radiometer equation:

$$\Delta T_{rel} = \frac{(T_{sys} + T_{sig})}{\sqrt{B\tau}} \quad \text{(radiometer noise contribution)} \tag{4.29}$$

T_{sys} is the current estimate of system temperature, determined once per MAF as a performance monitoring diagnostic (section 4.9.1), and T_{sig} is the calibrated limb radiance. Based on UARS experience and the similarity of the EOS MLS design, T_{sys} is expected to vary by <0.5% orbitally, which introduces negligible error in this component of estimated radiance uncertainty.

Interpolated reference noise contribution

The second term inside the square root of Equation 4.28 represents the uncertainty in the interpolated space reference:

$$\Delta T_{rel} = \Delta R \quad \text{(interpolated reference uncertainty contribution)} \tag{4.30}$$

This uncertainty is inferred from the estimates of uncertainty in the quadratic fit coefficients of Equation 4.21, and is given by the expression:

$$(\Delta R)^2 = \frac{1}{g^2} [\begin{array}{ccc} 1 & j & j^2 \end{array}] \, S^{-1} \begin{bmatrix} 1 \\ j \\ j^2 \end{bmatrix} \tag{4.31}$$

where g is the channel gain in units of Counts per Kelvin and the matrix S is given by:

$$S = s^2 \begin{bmatrix} \Sigma \frac{1}{w^2(j)} & \Sigma \frac{j}{w^2(j)} & \Sigma \frac{j^2}{w^2(j)} \\ \Sigma \frac{j}{w^2(j)} & \Sigma \frac{j^2}{w^2(j)} & \Sigma \frac{j^3}{w^2(j)} \\ \Sigma \frac{j^2}{w^2(j)} & \Sigma \frac{j^3}{w^2(j)} & \Sigma \frac{j^4}{w^2(j)} \end{bmatrix} \tag{4.32}$$

s^2 is the sample variance, given by:

$$s^2 = \frac{1}{(N-3)} \Sigma [C - C(j)]^2 \tag{4.33}$$

and N is the number of data points included in the fit. From UARS experience we expect the sequence of space measurements to be well behaved, and replace the determination of the sample variance with a reliable estimate given by the radiometer equation:

$$s^2 = \frac{(C^S - C^Z)^2}{B\tau} \tag{4.34}$$

where $(C^S - C^Z)$ is the count contribution from the reference radiance with the digitizer offset removed. This expression for the variance is readily converted from Counts^2 to Kelvin^2 by applying the channel radiometric gain accordingly.

Interpolated gain noise contribution

The third and final term inside the square root of Equation 4.28 adds the uncertainty due to noise on gain measurements. Channel gains are evaluated at the times of the limb views using interpolated estimates of space and ambient target counts. The expression used to determine channel gain at the times of the limb views, Equation 4.18, differences the interpolated ambient target and space reference counts at the times of the limb measurements. This differencing serves as a high pass filter which attenuates the effects of common drifts in space and ambient target measurements.

This allows us to write:

$$\left(\frac{\Delta g}{g}\right)^2 = \frac{\Delta C_T^2 + \Delta C_S^2}{(\widehat{C}^T - \widehat{C}^S)^2} \tag{4.35}$$

directly from Equation 4.18, where ΔC_T^2 and ΔC_L^2 are the mean square noise counts of the interpolated target and space reference counts at the time of the limb view. Under conditions in which $\frac{1}{f}$ noise does not have a significant impact on precision estimates (the case for most EOS MLS channels) the method we have chosen for interpolation provides us with estimates of these interpolation precisions:

$$\Delta C_T^2 = \frac{(\bar{C}^T - C^Z)^2}{B\tau} \times \frac{1}{(\Sigma w_T(j))^2} \times \Sigma w_T^2(j) \tag{4.36}$$

and

$$\Delta C_S^2 = \frac{(\bar{C}^S - C^Z)^2}{B\tau} \times \frac{1}{(\Sigma w_S(k))^2} \times \Sigma w_S^2(k) \tag{4.37}$$

where w_T and w_S are the interpolation weights for the target and space reference views. $\bar{C}^T$ and $\bar{C}^S$ are the mean target and space reference counts in the calibration window. Noting that:

$$\Sigma w_T(j) = \Sigma w_S(k) = 1 \tag{4.38}$$

and dropping the weighting indexes j and k, we arrive at the following expression for the uncertainty arising from the finite precision of the radiometric gain estimate:

$$\Delta T_{rel} = \frac{T_{sig}}{(\widehat{C}^T - \widehat{C}^S)} \times \sqrt{\frac{(\bar{C}^T - C^Z)^2 \Sigma w_T^2 + (\bar{C}^S - C^Z)^2 \Sigma w_S^2}{B\tau}} \tag{4.39}$$

Note that this component of uncertainty scales with the magnitude of the limb radiance. For in-balance[1] situations this component of uncertainty is essentially nonexistent.

4.5.2   Absolute radiance uncertainties

The atmospheric radiance signals of interest appear as noise power in the radiometer IF outputs, typically much smaller than the noise contribution from the radiometers themselves. Gain variations modulate the total IF noise power, causing the overall signal counts from each filter channel to exhibit low frequency noise characteristics even when viewing a scene of fixed radiance. The typical nature of these variations is that they have a $\frac{1}{f}$, or similar, dependence so that their magnitude increases with increasing time scale. Care is being taken

---

[1]In-balance means that scene and space reference radiances are similar.

with subsystem design and choice of components (HEMT IF amplifiers in particular) to ensure that the breakpoint frequencies of such gain variations are no higher than necessary.

The largest effect of these gain variations is on limb radiances measured most distant in time from the encompassing space reference views. For the absolute radiance uncertainty determination we require knowledge of the shape and magnitude of the post detector noise power spectrum in the instrument's orbital operating environment, which will be obtained by Fourier transforming sufficiently long (a small even integer number of orbits) time series of ambient target data (see [11] for details). These data will be acquired on occasional days (estimated at ∼2–3 during the first year of operation and approximately annually thereafter) devoted to in-orbit instrument characterization, since the data analyses require a sequence of target view data equally separated in time, a situation not achieved during nominal instrument operation. The non-spectrally flat component in these power spectra, $S_g(f)$, will be determined during off-line processing of these special data sets, not during routine Level 1 processing.

The term of interest here in the expression for limb port radiance (Equation 4.19) is the one which differences actual limb counts with interpolated space reference counts. The quadratic interpolation used to estimate the reference signal at the time of the limb measurement can be formulated as a sequence of weights applied to each reference measurement included in the fit. The (signal − reference) estimate may then be formulated as a linear combination of weighted signal and reference measurements. This sequence in the time domain is then Fourier transformed to provide the equivalent response of the interpolation and differencing process in the post-detector frequency domain, $H(f)$. This process is described in Appendix D. Using these values for S and H we can then evaluate the absolute radiance uncertainty, ΔT_{abs}, from:

$$\Delta T_{abs} = (T_{sys} + T_{sig}) \sqrt{\int_0^\infty S_g(f) H(f) \, df} \qquad (4.40)$$

This differs from the expressions in Appendix C only in normalization.

The integral inside the square root of Equation 4.40 will be evaluated for each radiometer for the nominal calibration window, measurement sequence and timings, for each MIF within the central MAF. This will be done numerically during off-line processing, resulting in a vector of multipliers for each radiometer, one for each MIF in the central MAF. These vectors will be provided to Level 1 processing as user inputs, and absolute radiance uncertainties will be determined during Level 1 processing by multiplying the sum of system and signal radiances by the component of the vector corresponding to the radiometer and MIF of the measurement.

An approximation being made in evaluating the vector of uncertainty multipliers is that a constant length MAF and fixed observing sequence is being assumed. In practice the length of the MAF will vary by $\pm\frac{1}{6}$ s to maintain synchronization between the scanning pattern and the orbit. The additional error introduced by ignoring this minor variation in timing is negligible compared to the errors themselves. It should also be noted that the error multiplier vector will be symmetric about the center of the limb observing portion of the MIF, and so only the first half of the vector will be supplied to Level 1, the last half being just a mirror image of the first half, as shown in Figure C.4. The vector supplied to Level 1 will accommodate the longest MAF sequence expected during nominal instrument operation, and for shorter MAFs the vector will be truncated to fit the actual length of the atmospheric measurement sequence.

4.6   Details of THz algorithms

The THz radiometer calibration is similar in many respects to the MLS GHz radiometer. However, the THz Laser Local Oscillator (LLO) presents special problems that influence the design of the calibration algorithm because the LLO power varies significantly with time. Changes in LLO power create approximately proportional changes in IF power level. Fortunately, the mixer bias is a measure of the LLO power and is recorded every MIF, and this bias information can be used to correct the raw radiometer counts for variations in LLO power.

4.6.1   LLO Nominal Operation

In normal operation, the RIU[2] requests telemetry data (including mixer bias voltage) each MIF by sending `command 7`. The far-infrared laser in the LLO operates in open-loop mode until a request is made to perform a re-optimization by sending `command 28` (typically in MIF 139). This command is sent before the `command 7` string. If the laser needs re-optimization, or if a certain number of MAFs have elapsed, then status is returned, and the laser is re-optimized. Otherwise, only status is returned.

4.6.2   Mixer Bias Handling

Since the mixer bias will be used for correcting the radiometric counts, it is important to check that the values are valid. Since the maximum bias voltage is less than 10 V, the value of 10 V is used to indicate an error. If the OPSTAT-A byte status message in response to `command 28` is not 1 (thereby indicating that the laser was re-optimized) the bias is set to 10 V. Usually there will be a NAK response to `command 7` if the laser is re-optimizing, and the bias is invalid anyway. If OPSTAT-A is equal to 1, the bias voltage should be retrieved from the `command 7` response. The bias voltage is $\sim$3.5 V for the flight LLO and decreases as LLO power increases. Therefore, a threshold voltage of intermediate value, e.g., 2 V, can discriminate between good LLO operation and other states that can include poor LLO operation, invalid mixer bias, and a LLO re-optimization event. For simplicity, any state that produces a bias voltage below the threshold will be designated as valid mixer bias. (The IDL procedure THzBias.pro on the GSE performs this function).

4.6.3   Correction for LLO Power and Radiometric Gain

The first step for THz calibration is to take 1 orbit of data ($\sim$100 min) and and determine boundaries where the laser has re-locked or there is a gap in the data. (The IDL procedure THzBoundary.pro on the GSE performs this function). Then perform a 2-parameter fit for LLO sensitivity and radiometric gain to the subset of the calibration data that have valid mixer bias:

$$C_{i,k} = C_{i,k}^0 + d_{LLO,i}(B_k - \hat{B}_k) + d_{CAL,i}(T_k - \hat{T}_k) \tag{4.41}$$

where $C_{i,k}$ is the calibration count for channel i and time sample k, B_k is the mixer bias and $\hat{B}_k$ is the average mixer bias within the boundary that contains time sample k. T_k is the calibration scene temperature and $\hat{T}_k$ is the average scene temperature within the boundary.

---

[2]Remote Interface Unit. See chapter 5 for further details.

By use of these dependent variables, d_{LLO} and d_{CAL} can be determined without fitting for C^0 since the correlation with C^0 is identically zero. Also note that the least-squares matrix is independent of i, and much of the least-squares solution is common to all channels. The validity of the fit depends on assuming that temporal drifts in the counts are uncorrelated with B or T. The use of local averages allows for discontinuities in counts when the LLO is re-locked.

The partially calibrated counts are then:

$$TS_{i,k} = \frac{C_{i,k} - d_{LLO,i}(B_k - \hat{B})}{d_{CAL,i}} \tag{4.42}$$

where $\hat{B}$ is the data set average of mixer bias. The correction of counts to temperature units should be applied to the whole data set, not just the calibration data subset. Clearly the LLO correction can only be applied to data with valid mixer bias. TS still contains a substantial offset which is of the order of T_{sys}. In fact, if $C_{i,k}$ is corrected for zero counts, then TS is equal to the y-factor T_{sys} plus the scene temperature. (The IDL procedure THzDel.pro on the GSE performs this function).

4.6.4 Correction for Offset

The second step is to subtract offsets so that the calibrations are equal to their respective temperatures. Like the GHz calibration, this subtraction will involve piece-wise quadratic interpolation of the fitted calibrations. Even after correction for LLO power variation, the radiometer response, TS, shows discontinuities in slope at times where there is a LLO re-optimization. Accordingly, the piece-wise fitting will use continuous segments of data with valid mixer bias (determined with the IDL procedure THzBounds). For a given MAF, choose calibration data in a window centered in the MAF at time t_c with a width, w, such that $|t_k - t_c| < w$ and fit

$$TS_{i,k} = T_k + a_i + b_i(t_k - t_c) + c_i(t_k - t_c)^2 \tag{4.43}$$

where k is limited only to calibrations within the window and within the segment with valid mixer bias. If the range of data included in the fit spans only the time interval of one MAF, fit only for a_i. If it spans a time interval of 2 MAFs, then fit for a_i and b_i, otherwise perform the full quadratic fit. Typically, $w = 2$, although larger values should be possible if the system stability justifies it. Again, the least-squares matrix is independent of i so computation speed can be improved by inverting the matrix only once. In addition, computational speed can be improved at the expense of memory storage by pre-storing computations for common configurations of the MAF within the data segment. Then,

$$TA_{i,k} = TS_{i,k} - a_i - b_i(t_k - t_c) - c_i(t_k - t_c)^2 \tag{4.44}$$

is applied to all data within the MAF. (The IDL procedure THzCal.pro on the GSE performs this function).

4.7　Additional algorithms for DACS

The DACS, described in detail in Appendix G, process signals in an entirely different manner from the filter spectrometers, resulting in quite different processing algorithms. Some details of the DACS data processing depend upon the mode chosen for their operation (e.g., constant input signal power for all measurements or constant signal chain gain). Below we describe the mode in which these spectrometers will be operated, followed by the resulting data processing algorithms.

4.7.1　Operating mode

The mode and environment in which the DACS will be operated on EOS MLS are:

1. The gains of the IFs feeding the DACS will be kept constant during limb scans – i.e., no 'automatic gain control' will be implemented to keep the input RF power to the DACS constant, a fairly common practice with DACS used to analyze radio telescope data.

2. Digitizer thresholds will be changed infrequently. Threshold levels will be logged, but are not included in the telemetry generated by the instrument.

3. The estimation of the multibit autocorrelation from the measured 2-bit autocorrelation will include corrections for changes in power level and for asymmetries in the threshold settings.

The digitizer thresholds will be set to ± 0.9 of the rms of the input signal level when viewing the Space reference, which when combined with the simplified multiplier arrangement of this implementation results in a S/N ratio 0.87 times that of a continuous correlator.

4.7.2　DACS data processing

The four DACS bands produce approximately 50% of the MLS internal instrument data traffic, and their inclusion, without compression, takes MLS $\sim$30% above its 100 kbps telemetry allocation. Fortunately, when viewing thermal noise signals, the 24-bit autocorrelation lags have many bits well below their noise floors, and these bits can be omitted with minimal degradation of signal-to-noise. Also, since the observed signals will be dominated by spectrally-flat receiver noise, autocorrelation signals will fall off, in lag, as the sinc-like Fourier transform of the DACS' bandpass. Autocorrelation in most the DACS lags will contain values that are only small multiples of the lag's noise floor and they can be coded in a limited number of bits. Note that the term 'lag' is used to refer to one of the 129 different time delays in the autocorrelation while 'channel' is reserved for the 129 different frequencies of the power spectral density after Fourier transform into the frequency domain.

　　A compression scheme for DACS data has been implemented which reduces the DACS telemetry data rate by more than a factor of two, and its use will be part of the normal operating mode. Science telemetry in this mode has all four DACS bands compressed into Science Type I packets. There are two diagnostic modes in which subsets of the uncompressed DACS channels are transmitted as Science Type II or Type III packets. Definitions of these packets and details of the compression scheme are provided in the C&DH Command and Telemetry Handbook (CTH)[13], and in Appendix H.

The DACS data are processed via the following steps:

1. uncompress compressed data (Science Type I), or normalize uncompressed data (Science Types II or III),

2. fix any errors in state counters,

3. convert measured 2-bit autocorrelation to best estimate of the continuous auto-correlation function,

4. scale normalized autocorrelation by total power

5. Fourier transform into the frequency domain, and

6. convert from relative to absolute signal intensity (i.e., perform radiometric gain calibration).

Normalization of uncompressed data consists of dividing the counts in each lag by the counts from the zero delay lag:

$$R(j) = K(j)/K(0) \tag{4.45}$$

Compressed data (Science Type I) are normalized in the compression process. Equations 4.45 and 4.46 are taken from Appendix G which should be consulted for further details. Each DACS band also has a total power measurement from its analog channel and four state counters which accumulate the number of clock ticks for which the 2-bit digitizer was in each of its four states during the data integration. The state counters have occasional single-bit errors which apparently result from a hardware bug. As the total number of clock ticks in an integration is extremely stable, the presence of an error in a set of four counters as small as four counts is easily detected. The individual counter which contains the bit error always has trailing binary zeros below an erroneous zero, as if a carry bit rippled through as the integration window ended, but never set the high bit at the end of the ripple. The signature of trailing zeros allows the identification and correction of the individual counters containing errors. This correction is described in Appendix H.

After correction of the state counters, we convert the measured 2-bit correlations in each channel to estimates of the continuous (multi-bit) correlation coefficients. The algorithm used in this conversion includes the modeling of a digitizer with slightly asymmetric thresholds, as inferred from state counter statistics. Again, the details are given in Appendix H.

Transformation of the normalized autocorrelation function into the frequency domain is accomplished via a Discrete Cosine transform (DCT):

$$P\left(\frac{j}{2M\Delta t}\right) = \frac{1}{M}\left[R(0) + 2\sum_{m=0}^{M} R(m\Delta t) \times \cos(\pi m j/M)\right] \tag{4.46}$$

The autocorrelation of the stationary Gaussian noise signals observed by MLS is even in time, and thus symmetric about the zero lag. The measured products of current and delayed signals could just as well be considered future and current signals except for details at the start and end of integration. The 129-element DCT can be implemented wiht a 256-element Fast Fourier Transform (FFT) to reduce computational burden. The implementation of a DACS with 129, rather than 128, lags allows the creation of a 256 (2^8) element real data

vector by appending to the 129 element measurement vector the 127 element vector consisting of the original 129 element vector, reversed in time order, with the first and last elements deleted. The data vector being transformed thus has a number of elements which is a power of 2, an optimal number of elements for the FFT. The Fortran module used in the production code, which is specifically for a DCT of length $2^n + 1$, is even more efficient as it does not waste time calculating the imaginary elements of the FFT.

Normalized power spectra are scaled by the total power measurements for each band and then the radiances are calibrated using views of the internal calibration target and space, as is done with filterbank channels. Each DACS band has an analog total power channel similar in implementation to a filterbank channel. Band total power may also be inferred from each band's four state counters, which provide digitizer statistics. The analog measurement does not suffer the ∼13% signal-to-noise degradation that arises from the coarse quantization in the digital signal path. On the other hand, the analog measurement's signal path includes an additional amplifier and does not include the bandpass characteristics of the comparators in the digitizer, so it is not quite the correct normalization for the digitally-derived spectrum. Also, the analog total power has a zero offset which must be determined, while the digitally-derived total power is offset free. Both total power measurements will be calculated and saved in the engineering data. Initially, the analog measurement (minus its zero offset) will be used in processing, but this choice will be revisited at a later time.

The most straightforward method of radiometric calibration of the DACS data is to scale each normalized spectrum with its corresponding total power measurement, and then to treat each channel, individually, as if it were a filterbank channel. For each DACS band, this involves the quadratic interpolation of the space and target view measurements within the calibration window to the times of the limb views. It should be noted that 1/f noise due to gain drift is almost completely isolated to the total-power measurements. Total power and normalized spectra of the calibration views will be filtered separately, as the normalized spectra may be averaged over much longer windows than is appropriate for the total-power channels. Given the stability expected in orbit, it may be appropriate to average a day's Space and Target normalized spectra, or to use constant spectral shapes, to be updated as needed. The stability of the normalized calibration views will be investigated after launch.

Ideally, the spectrally-flat Space and Target views should have identical normalized spectra. When measured, the normalized spectra of the GHz ambient target and of a liquid nitrogen load (proxy for Space views in the laboratory) are very similar, but have systematic differences on the order of 1×10^{-3}, or on the order of $1\,\mathrm{K}$ in radiance. If the normalized spectra of Space and Target were identical, a single gain per band could be calculated using only the total power measurements, significantly reducing the computational burden of interpolations. A method of making first-order corrections for the effects of the spectral differences between Space and Target on a single gain is described in Appendix H.

4.8   Spectral baseline

The finite apertures of the MLS optical systems introduce small truncations at the edges of the beams viewed by the radiometers. These truncations create diffraction lobes which vary with signal frequency (i.e., channel) resulting in small channel-dependent antenna patterns and losses through the optical paths from antenna to receivers. Although these effects are small, less than ∼0.1 K across the UARS MLS bands, they result in a channel-dependent signature

in the radiances measured through the GHz antenna which can be measured. This signature, called spectral baseline, is observed when differencing signals measured through the antenna (when observing the atmosphere with a sufficiently large tangent height that atmospheric contributions to the spectrally varying component of observed radiance are negligible) from those measured through the space port. The THz optical design uses a common scanning mirror for observing both signal and reference, and is thus less susceptible to the generation of baseline artifacts. Spectral baseline will be determined by Level 1 processing for both GHz and THz radiometers.

UARS MLS experience indicates that these small baseline signatures can be latitude dependent, and can be different for ascending and descending portions of the orbit. For EOS MLS Level 1 software we choose latitude bins similar to those used for UARS, $\sim 22.5°$, resulting in a total of 16 bins (4 north of the equator for ascending and descending portions of the orbit, and the same number south of the equator). Limb observations with tangent point altitudes above selected thresholds will be used to update the appropriate bin (selected by tangent point latitude and ascending/descending flags) by adding the limb/space port difference (in calibrated radiance units) to the data in that bin and incrementing counters which indicate the number of radiances accumulated in each bin. At the end of a processing run these information are converted into average radiances by simply dividing the accumulated radiance by the total number of accumulated radiances in that bin. This results in a spectrum for each band and bin which will be written to the radiance file for use by Level 2 processing.

The tangent point altitudes above which each channel will be included in the baseline computation will be indicated by user input, and will be initially defined by those responsible for the Forward Model and retrieval algorithms. These altitudes will likely be modified after launch based on analyses of in-flight data, as may be the selection of latitude bins. Spectral bands with strong narrow atmospheric signals at the highest altitudes scanned need only baseline data from the wing channels. The maximum nominal tangent height of the GHz radiometer observations is $\sim 90\,\mathrm{km}$, and occasional periodic scans to higher altitudes may be included to improve baseline data quality. This decision will also depend of analysis of in-flight data.

4.9 Diagnostics

Several diagnostic quantities will be routinely computed during Level 1 processing and written to the GHz and THz diagnostics files. These quantities are intended to be plotted and examined daily, to provide a clear picture of instrument performance, and hence must be limited in quantity and simple to interpret. To provide end-to-end visibility into system performance these quantities are all derived from spectrometer outputs, and are:

1. System temperatures,

2. Reference χ^2,

3. Interpolated channel gains, and

4. Channel zeros.

This selection is based on UARS MLS experience, and may change as further insight is gained into the nuances of EOS MLS behavior with analyses of EM and FM data.

4.9.1   System temperature

System temperature (T_{sys}) measurements provide an instant view of radiometer performance at a high level. This diagnostic quantity will be evaluated once per MAF since it is used in the estimation of radiometric precision. T_{sys} for each filter channel i is computed from the expression:

$$T_{sys}(i) = \frac{(\hat{C}_i^S(Z) - C_i^Z)}{\hat{g}_i(Z)} - \overset{\bullet}{P}_i(2.7) \qquad (4.47)$$

where $\hat{C}_i^S(Z)$ are the interpolated space view counts at the time of the zero measurement, C_i^Z are the zero counts, and $\hat{g}_i(Z)$ is the interpolated gain at the time of the zero measurement for channel i. $\overset{\bullet}{P}_i(2.7)$ is the radiative 'temperature' of cold space, which, as per Equation 4.1, ranges from $\sim$0 to $\sim$0.8 K for the full complement of EOS MLS radiometers. The equations given earlier in this chapter for these quantities are used in generating this diagnostic. Interpolated quantities are determined as described earlier in this chapter, and the temperature of cold space is assumed to be 2.7 K.

For UARS MLS we were able to measure C_i^Z regularly and frequently. With the current instrument there is no mechanism for reducing the IF gains of all bands to their minima concurrently (or for easily restoring them to their operational settings). We thus plan to measure C_i^Z every few weeks, an activity likely to be performed in parallel with any GHz antenna mechanism 'conditioning' actions. We expect C_i^Z to remain stable over temperature and time, and so their infrequent update is not considered to be a problem.

The IF attenuation range for FB25 and FB11 bands is 32 dB, and for the Wide Filters is only 16 dB. In practice the IF attenuators are not set for minimum attenuation during nominal observing, meaning that the IF attenuation change between observing and IF Zero measurements can be as small as $\sim$20 dB for some FB25 and FB11 bands, and $\sim$10 dB for some of the Wide Filters. This manifests during instrument testing (and operation) as clearly visible filter channel count level changes corresponding to the views to scenes at different temperatures. These errors in C_i^Z would result in overestimation of T_{sys} by $\sim$1% for the filterbanks channels, and up to $\sim$10% for some Wide Filter channels if left uncorrected. At the time of launch Level 1 software will not apply any corrections to the measured C_i^Z. During the instrument activation period we will determine the IF attenuation settings for all bands, and make the appropriate minor changes to the software to compensate for the finite additional attenuation introduced during C_i^Z measurements.

4.9.2   Reference χ^2

System temperature measurements provide a valuable, but incomplete, indication of instrument performance in regards to sensitivity. This is because the noise level on a channel is extremely sensitive to signal chain stability over timescales from a single data integration up to a calibration window ($\sim$3 minutes). A broad standard spectrometer channel (96 MHz) is subject to radiometer noise which has an rms of only 1 part in $\sim$4,000 of the digitized channel output in a single $\frac{1}{6}$ s data integration. This means that variations in channel gain of less than 0.0004 dB impart significant additional uncertainty into calibrated limb radiances.

The effects of smooth gain variations, such as those caused by orbital temperature variations, are largely removed by the Level 1 radiance calibration algorithms, but variations due to interference, gain variations over the timescales of a MAF, or degradations in signal chain

electronics, are harmful. A suitable diagnostic for revealing degradations of this nature is a plot of reference χ^2 for each filter channel. The space reference is observed for more MIFs than the ambient target, so it is chosen for this diagnostic, and determined by interpolating the reference counts onto the times of each reference measurement and computing the mean square differences between measurements and interpolates for each channel. The quantity written to the diagnostics file is the ratio of the observed mean square deviation to that predicted simply by the radiometer equation. This diagnostic has proven invaluable on UARS MLS during in-flight operation where it has provided immediate indication of such problems as vibrationally induced noise from the switching mirror, allowing rapid correction of the problem by minor changes to operating modes. This diagnostic is also currently in use for analyzing the performance of some EOS MLS breadboard radiometers where the variation of χ^2 with channel bandwidth, and its behavior as the timing of the reference measurements is changed, has led to the rapid discovery of signal instabilities due to ground loops and other test setup issues, greatly facilitating the correction of such problems.

4.9.3   Interpolated gains

The Level 1 radiometric calibration process effectively conceals potential performance changes such as substantial drifts in channels gains which are indicative of failures or degradations in electronic subsystems. We thus write the interpolated channel gains (Equation 4.18) at the times of the first calibrated limb radiance in each MAF to the Diagnostics file for daily review.

4.9.4   Channel zeros

Performance of the filter channel post-detector electronics is monitored by reviewing the offsets of the channel digitizers, measured in orbit whenever IF gains are reduced to their minima to monitor T_{sys}. This parameter reveals any problems due to DC amplifier offset drifts, and on UARS MLS was used to detect a small number ($\sim$3) of filter channel post detector amplifiers which degraded during ground testing, and were replaced prior to launch (no further channels have degraded in this manner after more than 7 years in orbit). No algorithms are necessary to determine this quantity – all channel 'zero' data are simply written to the Level 1 Diagnostics file.

4.10   Calibration and ancillary inputs to Level 1 processing

Table 4.2 lists parameters needed by Level 1 software to implement the algorithms described in this document. The parameters listed below ϵ_r are discussed further in the next chapter.

Table 4.2: Summary of parameters required by Level 1 software. PRD is an abbreviation for Platinum Resistance Device, the type of temperature sensor used to monitor the ambient calibration targets. IRU is the abbreviation for Inertial Reference Unit, the spacecraft attitude determination system.

Symbol	Units	Description	Purpose
B_i	Hz	Noise bandwidth of each filter channel	Radiometric noise determination
τ	s	Integration time	Radiometric noise determination
$S_g(f)$	$\mathrm{W\,Hz}^{-\frac{1}{2}}$	Post detector noise power spectral density for each radiometer	Absolute radiance uncertainties
$r'_l,\ r'_u$	–	Relative sideband responses from mixer to switching mirror	Radiometric calibration
ρ_r^k	–	Reflectivity of antenna element k	Antenna emission (radiance) determination
$\eta_{i,s}^{AA}$	–	Antenna beam efficiencies	Limb port to limb radiance conversion
$\eta_{i,s}^{MX}$	–	Baffle transmissions	Radiometric calibration
$\eta_{i,s}^k$	–	Optical transmission of antenna reflector k	Radiometric calibration
ϵ_r	–	Calibration target emissivities	Target radiance determination
$d\alpha$	K^{-1}	Pointing thermal coefficients	Absolute pointing. These coefficients are combined with measured MLS structural temperatures to determine thermal distortions
α, ϵ	$^\circ\,\mathrm{Count}^{-1}$	Encoder coefficients	Conversion of encoder counts to pointing angles
$\mathbf{E}$	–	Rotation matrices from instrument to spacecraft reference cubes	Absolute pointing determination
$\mathbf{D}$	–	Rotation matrix from spacecraft reference cube to IRU reference frame	Absolute pointing determination
$\mathbf{E}^T, \mathbf{D}^T$	K^{-1}	Thermal coefficients of $\mathbf{E}$ and $\mathbf{D}$	Absolute pointing. These coefficients are combined with spacecraft thermal data to correct for thermal distortions in spacecraft structure between MLS and the IRU.
R_0	Ω	$0\,$C resistances of individual PRD temperature sensors	Determination of cal target temperatures
$\mathrm{C_l, C_h}$	Ω, V	Engineering Data Hybrid internal calibration values	Conversion of engineering data 'counts' to engineering units
a, b	–	PRD conversion coefficients	Conversion of PRD resistance into inferred temperature
c, d, e, f	–	Thermistor conversion coefficients	Conversion of thermistor resistance into inferred temperature

Chapter 5

Engineering data

The MLS instrument data system comprises a redundant pair of central Command and Data Handling (C&DH) subsystems linked via serial data and synchronization busses to a network of ~30 Remote Interface Units (RIU). Each RIU contains an Engineering Data Hybrid (EDH) which is used to acquire analog engineering data. A partial list of the capabilities provided by an EDH includes:

1. multiplexing (selection) of input signals from one of 16 external or 6 calibration (internal or external) sources,

2. selection of input polarity,

3. selection of signal gain,

4. selection of source excitation current (none, 0.1 mA for thermistors or 1.0 mA for Platinum Resistance Device temperature sensors),

5. selection of signal offset, and

6. digitization via a V/F converter, with the output from the V/F recorded by logic in the RIU.

Not all combinations of signal chain attribute listed above are selectable without restriction, and the EDH is targeted towards the measurements of voltage and resistance (to support both PRDs and thermistors) as shown in Table 5.1. Resolution of the digitized result is limited by the external counter gate time and by the inherent noise of the V/F converters, but is designed to meet or exceed 16 bits for all measurements. The nonlinearity of the signal chain is dominated by the V/F converter, and is less than 0.05% of full scale signal for all measurement types. This level of performance is such that no corrections are needed in the processing software.

Figure 5.1 shows a block diagram of the EDH. One of 16 input sources is selected via an analog multiplexer which allows any input source to be either a voltage or resistance (for temperature measurements). Resistive sources are excited by a current source of either 0.1 or 1.0 mA, and the sensors may be connected in 2, 3 or 4 wire configuration. In addition, it is possible to reverse the polarity of the excitation current supplied to PRDs in order to repeat the resistance measurement. By averaging the inferred resistances measured using both polarities of excitation current, the effects of thermocouple-induced voltage errors in these

resistance measurements are eliminated. This is necessary to achieve the desired accuracies for PRD measurements of internal calibration target temperature.

Input signal source and polarity, excitation current, and channel gain and offset are all selected simultaneously via an externally-provided 20 bit control word which is generated under software control within the host RIU, allowing for considerable flexibility in measurement sequencing. The output from the EDH consists of a (nominally) square wave signal from the V/F converter which is of the same type used in all of the filter spectrometers. This V/F converter is operated over a substantially restricted portion of its potential operating range ($\sim$40 kHz to $\sim$80 kHz) in order to provide improved linearity compared to a system which operates with a low frequency limit much closer to zero; it should be noted that the operating ranges of the V/F converters in the filter spectrometers are restricted inherently by the system temperatures of the radiometers which tend to be large compared to the atmospheric signals.

An input channel is selected towards the beginning of a MIF, and the rest of the MIF is used to allow the analog circuitry to settle. In the case of resistance (temperature) measurements, some of this settling time may be required to charge up any feedthrough filters in the signal path from the EDH to the external sensor. The measurement system is designed to allow complete settling in the $\sim$1 MIF allocation. The subsequent MIF is used to measure the average frequency of the V/F converter output.

This timing scheme is illustrated in the upper half of Figure 5.2. Measurement sequences will be repeated starting on MAF boundaries, which implies that all engineering measurements made by any RIU can and will be completed in the duration of a MAF. In order not to 'waste' measurement time, some measurements may be selected more than once during a MAF, and Level 1 processing will separately process (and write to the Engineering file) measurements which are repeated during a MAF. The only exception to this is for the calibration targets PRD data; for these data Level 1 processing will additionally combine (by averaging) the 2 measurements taken of each PRD resistance in order to eliminate offsets due to thermocouple junctions in the wiring between EDH and sensor. The temperature deduced from this average will be used in radiometric calibration, but the individual temperatures

Table 5.1: Input signal types and attributes supported by the Engineering Data Hybrid. Measurements are of voltages or resistance. PRD1 and PRD2 refer to Platinum Resistance Device temperature measurements over a relatively narrow temperature range (PRD1) for the internal calibration targets, and a wider range (PRD2) for the sensors monitoring the structure external to the main modules.

Measurement Type	Minimum	Maximum	Units
Voltage	-1	$+7$	Volts
PRD1	460	640	Ω
	(-20)	$(+70)$	(C)
PRD2	300	700	Ω
	(-100)	$(+100)$	(C)
Thermistor	5.0	0.318	kΩ
	(-80)	$(+100)$	(C)
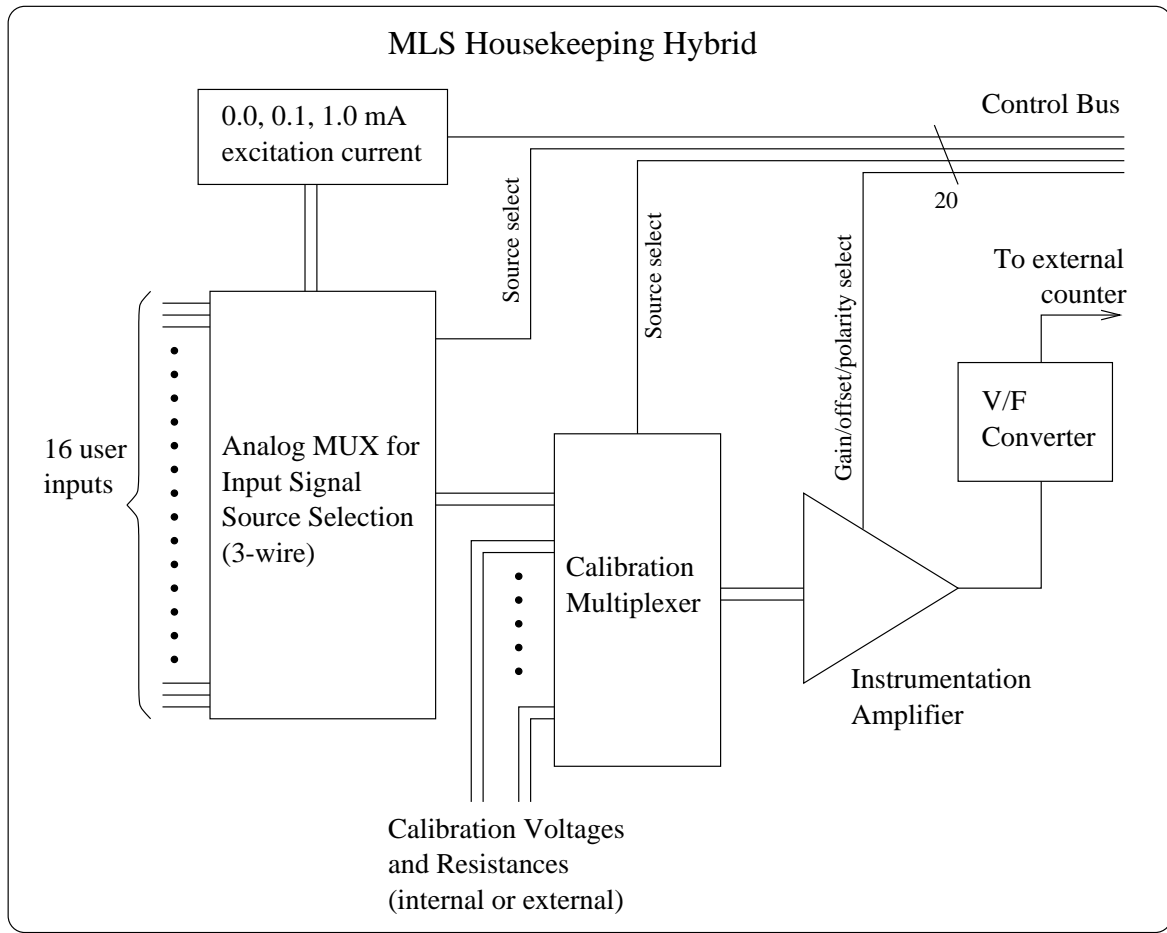
Figure 5.1: Block diagram of the Engineering Data Hybrid. See text for further details.

deduced from each excitation current polarity will also be written to the engineering file for diagnostic purposes.

Figure 5.2 shows additional details of the V/F frequency measurement scheme. The RIU generates a Gate signal to indicate when the V/F output is to be recorded. The rising and falling edges of this signal indicate to the control logic that the subsequent rising edges of the V/F output denote the actual period during which the number of cycles of both the V/F output (N_v) and of the higher frequency timebase (N_t) are recorded. This results in a variable measurement interval which is slightly delayed from the commanded one, but since the minimum V/F frequency is $\sim40\,\mathrm{kHz}$, the variation and delays are small and inconsequential. The control logic is designed so that a V/F converter which is stopped or running at a speed so low that the measurement cycle has not terminated in time for the next one to commence (due for example to a large input signal of the opposite polarity to the one assumed for that channel), the measurement cycle is forced to terminate, an error is recorded, and the next measurement cycle is started correctly and on time. The measurements of N_v and N_t are used to deduce the average frequency of the V/F converter output, f_v, from the straightforward
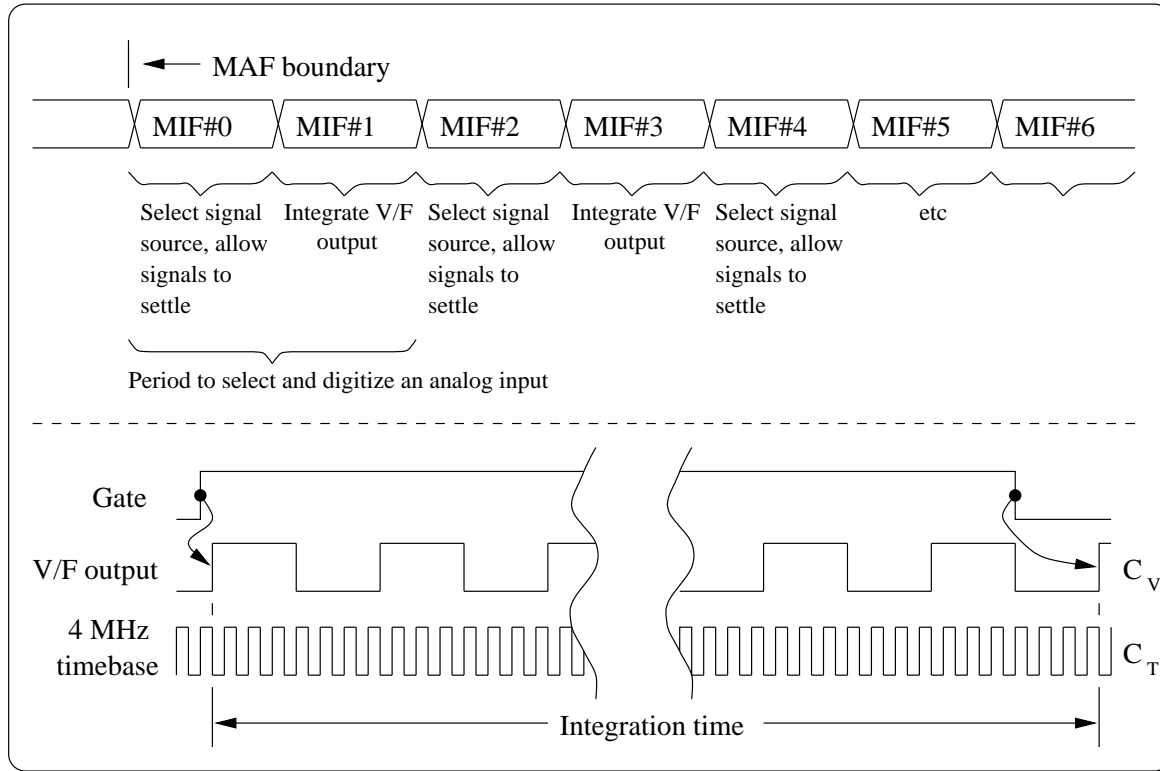
Figure 5.2: High level illustration of EDH timing. The upper portion of the figure shows timing at the MIF level, and the lower portion illustrates the relationship between commanded measurement interval (defined by the Gate signal) and that set by the V/F output. See text for further details.

relationship:

$$f_v = 4.0 \times 10^6 \times \frac{N_v}{N_t} \tag{5.1}$$

where 4.0×10^6 is the frequency of the timebase in Hz.

Advantages of this technique over the one used on UARS MLS (in which the V/F output is counted without additional information from a second counter monitoring a timebase) include:

1. the resolution of the measurement is limited by the frequency of the timebase, not the frequency of the V/F converter,

2. high resolution may be obtained even with the V/F converter run at a relatively low frequency and over a limited portion of its dynamic range (which improves linearity significantly),

3. by choosing a lower operating frequency range for the V/F converter than would be the case if the dual counter scheme were not employed, overall power consumption can be reduced, and

4. the inferred result (a frequency) is independent of the signal integration time.

Penalties for this measurement approach include:

1. larger counters are needed (40 bits total *vs* ∼16 for a UARS-like implementation),

2. the control logic is more complex, and

3. additional onboard processing is required, since we wish to telemeter the derived quantity f_v to the ground instead of the directly measured quantities N_v and N_t.

The resolution of this measurement system is ultimately limited by phase noise (jitter) in the V/F converter output signal which tends to have a nominally $\frac{1}{f}$ frequency characteristic. This means that for a substantial range of signal integration durations the S/N of the measured frequency remains essentially constant. The EDH signal conditioning electronics is designed to introduce much less noise into the measurement cycle than the V/F jitter, so that the dominant source of noise in a digitized signal measurement should be limited typically by the V/F jitter or by thermal drifts.

To make efficient use of the 16 bit telemetry words used to transfer engineering data, we offset and scale N_v and N_t to obtain the 16 bit quantity f_{16} as follows:

$$f_{16} = 12 \times 10^6 \left(\frac{N_v}{N_t} - 36 \times 10^3 \right) \times 1.35 \tag{5.2}$$

f_{16} effectively uses the full available dynamic range of the unsigned 16-bit slots assigned to each digitized engineering data quantity, with some margin for over- and under-range signals.

All analog quantities measured by an EDH are converted to engineering units in a similar manner. Measurements are classified according to 'type' by the source of the input signal:

1. a voltage (or another signal type, transformed to a voltage for digitization by the EDH),

2. a resistance consisting of a YSI 44906 thermistor in parallel with a precision $4.990\,k\Omega$ resistance, or

3. a resistance consisting of a Rosemount 118AKT2F PRD.

The PRD category is further subdivided, since PRD resistance may be read over one of two possible ranges, as shown earlier in Table 5.1. All input signals are converted into frequencies as described earlier. The frequency measurements of all non-calibration inputs are then converted into engineering units via linear interpolation using EDH measurements of calibration references. Each measurement frame (MAF) from an EDH contains at least one set of calibration pairs for each data type.

Analog data inputs are first calibrated using high and low calibration frequencies from the EDHs in each RIU:

$$x = \left(\frac{f_x - f_l}{f_h - f_l} \right) (C_h - C_l) + C_l, \tag{5.3}$$

where:

x is the desired input signal in engineering units, f_x is the frequency measured from the corresponding subchannel,

f_h is the 'high' calibration frequency for that channel type,

f_l is the corresponding 'low' calibration frequency, and

C_h and C_l are the high and low calibration parameters for this channel, which are measured during test of the EDH.

If more than one measurement of f_h and/or f_l is made during a given MAF, the values of f_h and f_l for that MAF are averaged before being applied in Equation 5.3. Multiple measurements of f_x for a given subchannel are processed independently however, and recorded in the Engineering output file as separately time tagged quantities. If no valid measurements of f_h and/or f_l are present in the data record for a given MAF, the most recent prior values are used. If no prior values exist (e.g., at the start of a daily processing run) then the values from the default file are used.

5.1   Conversion to engineering units

5.1.1   Voltages and currents

In the case of input voltages, Equation 5.3 gives the input signal to the EDH in units of Volts. For scaled voltages, and currents converted into voltages for recording by the EDH, the appropriate additional conversions need to be applied.

5.1.2   Temperature – PRDs

For resistive input sources, Equation 5.3 gives the resistance of the source in Ohms. For PRD sensors the measured resistance, R, is converted to a temperature, T, using the relationship:

$$T = \frac{a \times (R_{tlm} \times 500.0/R_0 - 500.0)}{(1.0 - b \times R_{tlm} \times 500.0/R_0)} \tag{5.4}$$

where:

T is the inferred temperature in Celsius,

a = 0.48945548411,

b = $7.20107099888 \times 10^{-5}$, and

R_0 is the resistance of the sensor at $0\,$C.

This expression is accurate to $\sim$0.15 C over the temperature range -50 C to +150 C. By customizing the coefficients a and b (not proposed here) the error is reduced to $\sim$0.08 C. The expression above is the one used in UARS MLS data processing.

Note that the calibration target PRDs are measured with both polarities of excitation current during each MAF. The inferred temperatures will likely be slightly different for each polarity, and the average of these temperatures for each sensor is the quantity to be used for radiometric gain determination and to be written to the Engineering file.

5.1.3 Temperature – thermistors

As for the PRDs, Equation 5.3 is used to determine the resistance presented by the sensor at the input to the EDH. Each thermistor is paralleled with a $4.990\,k\Omega$ precision resistor, and Equation 5.5 is used to converted the measured resistance, R_{in}, into the resistance of the thermistor sensor, R_{th}, in Ohms, as follows:

$$R_{th} = \frac{(4990.0 \times R_{in})}{(4990.0 - R_{in})} \tag{5.5}$$

The thermistor resistance is then converted into temperature (Celcius) using the relationship:

$$T = \frac{1.0}{(c + \log(R_{th}) \times (d + \log(R_{th}) \times (e + \log(R_{th}) \times f)))} - 273.16 \tag{5.6}$$

where:

$c = 1.286212 \times 10^{-3}$,
$d = 2.355213 \times 10^{-4}$,
$e = 9.826046 \times 10^{-8}$, and
$f = 8.835732 \times 10^{-8}$

This expression was derived for UARS MLS data processing using vendor supplied data.

5.2 Data quality and reasonableness

As for all telemetry processed by Level 1 software, engineering telemetry will be checked for reasonableness using available flags, CRC and checksum information. In addition, measurements of EDH calibration values will be limit checked, and appropriate estimates used in the absence of current data, together with the generation of diagnostic flags. Non-calibration inputs cannot be checked for reasonableness in most cases.

Chapter 6

Ancillary data

There are two primary classes of ancillary data in the context of Level 1 processing: those generated by the spacecraft or Flight Dynamics team, some of which are sent directly to MLS, and some generated by ground processing and made available to Level 1 software together with the instrument Level 0 data; and additional data needed by Level 2 which involves processing at Level 1, such as estimated tangent point location in an Earth referenced coordinate system and local solar time at the tangent point(s) of the observations.

The spacecraft generated/derived ancillary data listed in the Tables below are taken from the Interface Control Document for the Microwave Limb Sounder [7].

6.1 Spacecraft provided/related ancillary data

The ancillary data in Table 6.1 will be transferred to MLS via the 1553 spacecraft interface in 'real time,' while the data set in Table 6.2 will available to Level 1 during ground processing of data. All of these data will be written to Level 1 output files and hence be available to higher levels of MLS processing. X, Y and Z in the tables are the primary spacecraft axes about which all pointing information is reported. MLS observes in the XZ plane, with X being the nominal direction of flight of the spacecraft, and Z the nominal nadir direction. X, Y and Z form a conventional right-handed coordinate system.

The quaternion used to indicate spacecraft attitude and solar/lunar positions is a four element vector. Three of the elements specify a direction. The fourth element is the rotation angle (in a right handed coordinate sense) about that vector. The first three element are dimensionless, the angle is reported as the cosine of half the rotation angle.

6.2 Level 1 processed ancillary data

Table 6.3 lists those ancillary data required by Level 2 which is produced by Level 1 processing. These data will be written to an Ancillary Data file.

Each data ancillary record is tagged with the MAF count since the last instrument reset. No explicit MIF counter is included, as the data records are indexed by MIF from the start of the indicated MAF. An additional MAF counter indicates the MAF in the current orbit, and is reset to zero for the MAF following the one in which the tangent point crosses the equator heading south to north. A mission orbit number count is included in each record.

The master horizontal coordinate, ϕ, referenced in Table 6.3 is the angle between the normal to the geoid, normal to the nominal limb ray path (boresight), and the equator illustrated in Figure 3.7 of the Level 2 Theoretical Basis document [14]. This coordinate ranges between 0 and 360° (2π radians) at the start of processing, but in the ancillary data file will not be reset to 0 as it ranges beyond 360°, but allowed to increase throughout the day. Level 2 processing will convert it back to modulo 360 (or 2π) as necessary. This representation is at the request of Level 2 designers.

Table 6.1: Partial list of data sent from the spacecraft directly to MLS via the 1553 bus at a 1 Hz rate. Attitude angles are reported as a 4 element quaternion. ECI denotes Earth Centered Inertial. IRU indicates Inertial Reference Unit, the spacecraft gyro subsystem. See text for definition of the X, Y and Z axes, and of the quaternion. Packet headers have been omitted.

Description	Resolution	Range	Knowledge
Time Stamp	15.26 μs	year 1958 – 2094	10 ms
Spacecraft Position – ECI X,Y,Z	32 bits	$\pm$8,000,000 m	500 m
Spacecraft Velocity – ECI X,Y,Z	32 bits	$\pm$10,000 m s^{-1}	0.1 m s^{-1}
Attitude Quaternion (1,2,3,4)	32 bits	$\pm$1	25 arcsec
Attitude Euler Angle X,Y,Z	16 bits	$\pm$40°	65 arcsec
Attitude Rate X,Y,Z	16 bits	$\pm$0.3°s^{-1}	0.1 arcsec s^{-1},
Sun Vector X,Y,Z	16 bits	$\pm$1	0.075°
Moon Vector X,Y,Z	16 bits	$\pm$1	0.75°
Descending Node Crossing	16 bits unsigned	105 min	0.1 s
Oblateness Angle	16 bits	$\pm$40°	30 arcsec
Oblateness Rate	16 bits	$\pm$0.03°s^{-1}	0.01 arcsec s^{-1}
IRU Fault Status	16 bits	N/A	N/A

Table 6.2: Spacecraft-related data made available to Level 1 software during ground processing. Where these data are the same as those shown in the previous table, the accuracy and resolution of data provided on the ground are much higher.

Spacecraft Parameter	Description	Knowledge; Resolution	Time Tag Accuracy	Temporal Resolution
Position	ECI XYZ	500 m; 1 m	50 ms	1 Hz
Velocity	ECI XYZ rates	$0.1\,\mathrm{m\,s^{-1}}$; $1\,\mathrm{mm}$ $\mathrm{s^{-1}}$	50 ms	1 Hz
Attitude (roll/pitch/yaw)	Euler angle to orbit frame	65 arcsec; <0.2 arcsec	50 ms	8 Hz
Attitude Rate (roll/pitch/yaw)	Euler angle rates	$0.1\,\mathrm{arcsec\,s^{-1}}$; $0.01\,\mathrm{arcsec\,s^{-1}}$	50 ms	8 Hz
Sun Vector	Spacecraft to Sun XYZ	0.075°; 0.01°	50 ms	1 Hz
Moon Vector	Spacecraft to Moon XYZ	0.75°; 0.01°	50 ms	1 Hz
IRU Status and Gyro Status	IRU Configuration bits, Gyro Status Bits	Bits and gyro ID	50 ms	1 Hz
Altitude	Distance along Geocentric or Geodetic Vertical to Ellipsoid	15 m; <0.1 m	50 ms	1 Hz
IRU Gyro Angle	Accumulated angle in Gyro Coordinates	<1 arcsec; <0.1 arcsec	50 ms	8 Hz
Spacecraft Converter Voltage	SCE Voltage	<1 V; <0.1 V	50 ms	1 Hz

Table 6.3: A partial listing of spacecraft and pointing-related data to be written to a Level 1 Ancillary (LB1OA) data file. These data are primarily for use by Level 2 processing, and this table will be updated at the request of Level 2 designers. These data will be tagged with time, MAF and orbit counters.

Item	Description
Tangent points	Tangent point locations for R3 (B8) and R5H, the primary pointing radiometers for the GHz and THz modules. Reported as geocentric altitude, latitude and longitude.
Solar zenith angle	Solar zenith angle at the tangent points reported above.
Spacecraft location	Spacecraft geocentric altitude, latitude and longitude.
Elevation rate	Estimated elevation rate of the GHz and THz boresights derived from spacecraft attitude rate and actuator encoder data.
ϕ spacecraft	Spacecraft master horizontal coordinate. See text.
ϕ tangent point	Tangent point master horizontal coordinate. See text.

Chapter 7

Resource estimates

In this chapter we provide estimates for the key resource requirements of EOS MLS Level 1 processing, including file and daily I/O volumes, main memory requirements, and processing capability. Memory and processing capability are machine dependent, and only approximate estimates can be made at this time. The intent here is to bound the requirements of this software and show that they are reasonable. Since this software inherits much from its UARS MLS predecessor, many of the estimates can be checked for reasonableness by comparison. We also discuss how I/O is minimized in this processing, and how use will be made of parallel processing to reduce wall clock time of daily processing runs. To simplify the discussion we assume an operating mode which maximizes data rate while meeting the current instrument power allocation, realizing that other modes may be invoked which reduce all requirements discussed below.

7.1 Input data volume

The input to Level 1 processing is dominated by the instrument data stream, sent to the spacecraft at an average rate of 10^5 bits s^{-1}, a daily volume of $1\,\mathrm{GB}$ (GB $\equiv$ gigabyte, 2^{30} bytes). Ancillary data and overhead for the HDF (Hierarchical Data Format) file format headers and links is unlikely to raise the overall daily input data volume above $\sim 1.2\,\mathrm{GB}$.

7.2 Output data volume

DACS data input to Level 1 processing is marginally compressed within the instrument prior to packetization ($\sim 30\%$ compression) to meet the 10^5 bits s^{-1} instrument data rate allocation. The corresponding output data products are not compressed, primarily because they are in single precision floating point format for both radiances and uncertainties. If data storage ever becomes an issue (considered unlikely), these formats can be changed to scaled integers (as for UARS) with a small loss of dynamic range and increase in overhead at Level 2 to convert back to scientific format for processing.

The largest source of output data is the calibrated radiances for the filter and DACS channels, including the relative uncertainty calculated with each filter channel radiance. The daily volumes for these are computed in the following tables.

Number of filter channels:[1]	$19{\times}25 + 5{\times}11 + 8 = 538$
Readout rate:	120 times per MAF
MAFs per orbit:	240
Orbits per day:	14.6
Bytes per datum:	8 (includes radiance and uncertainty estimate)
Daily total:	**1.8 GB**

Number of DACS channels:	$129{\times}4 = 516$
Readout rate:	120 times per MAF
MAFs per orbit:	240
Orbits per day:	14.6
Bytes per datum:	4 (we assume a common uncertainty for all channels)
Daily total:	**0.9 GB**

Number of engineering channels:	500 (upper limit for analog monitors)
Readout rate:	Once per MAF
MAFs per orbit:	240
Orbits per day:	14.6
Bytes per datum:	4
Daily total:	**0.007 GB**

The daily totals are the products of all of the entries in each table, and the analog engineering data is seen to be insignificant in volume compared to the science data. Details such as the time tags for engineering data have been omitted and are likely to approximately double the daily volume for such data, but its volume still remains insignificant. The major missing category of data from the above tabulations is the diagnostic data required to monitor instrument radiometric performance. These data include the reference χ^2, interpolated channel gains and reference counts, and digital data such as phase lock status, and are likely to amount to about a quarter of the size of the radiance data volume, $\sim$0.7 GB (derived from comparison with UARS). The daily total data volume in the above categories is thus estimated to be $\sim$4.0 GB. At the time of launch, based on extensive testing and experience with the Level 1 software, we estimate a total daily output data volume of $\sim$4.1 GB. When the instrument becomes operational and we gain experience of its real characteristics and behavior, we fully expect to modify the diagnostic output product suite in order to provide clearer visibility. This will likely result in slightly larger total daily data output volumes.

7.3   I/O minimization

All filter channel data are gathered in a 6 MAF calibration window for radiometric calibration, with smaller windows for DACS and engineering data. Data are logically appended to the end of this window and deleted from its beginning as each MAF is processed. This results in

---

[1]In the primary (nominal) MLS operating mode only 8 of the 12 broad filter channels are turned on.

sequential access to the input data files, and the same for the output files, reducing file I/O to the minimum possible.

In the first versions of Level 1 software it is likely that baseline determination will be performed after all of a day's data has been processed, resulting in a second read of the output radiance file. This data can readily be determined as the radiance file is written for the first time, and this optimization will be incorporated after the algorithms for baseline determination are tested and verified.

The instrument data (Level 0) files input by Level 1 processing retain the packet structure generated by the C&DH, documented in [12]. Output files will be in HDF format, and as data are written, links will be updated and records written. A major advantage of this scheme is that files will only be of the size necessary to store actual output products, and the file records will not contain space for TBDs, spares, or data that might exist at some future time. This is a major benefit of an intelligent file structure, and also serves to minimize files sizes, and hence I/O volumes. This should be particularly evident for the EM which implements only 5 25-channel spectrometers, and none of the 11-channel, broad filter or DACS subsystems. This will result in a reduction in the radiance output file size to just over 10% its size for the full instrument in its primary operating mode.

7.4   Main memory requirements

There are three main components to the memory required by this software – the code itself, static data (such as calibration information), and workspace for the data in the calibration window and the results of computations on these data. UARS experience indicates that code size will be insignificant compared to available memory. The calibration window data structures contain 5 MAFs of instrument data and the derived output products. Instrument data for this window size amounts to 1.5 MB, and the output data (calibrated radiances, uncertainties, etc.) will increase memory requirements to ∼10 MB. Parallel processing (discussed below) requires duplication of certain working data structures since multiple threads will require some private working variables. Assuming that calibration and related data amount to a similar data volume indicates that the memory footprint of Level 1 software will be well under 100 MB. This is to be contrasted to the 8,192 MB available in the current version of the EOS MLS Science Computing Facility (SCF), indicating that main memory requirements are not an issue

7.5   Processing capability

To obtain an initial estimate of processing capability we have chosen to scale using UARS MLS Level 1 software performance as the benchmark. This is felt to be a reliable starting point because of the similarity of the algorithms for both instruments.

UARS Level 1 data processing is currently performed on a desktop Alphastation 4000 (300 MHz Alpha 21064 processor) and is I/O limited, taking ∼24 minutes of wall clock time, but only 65 seconds of CPU time, to process an entire days worth of instrument and ancillary data. The current SCF (an SGI Origin-2000 with 16 processors) benchmarks at ∼40 times the speed of the Alpha (this estimate comes from published SPECfp_rate95 figures for both machines). The I/O is also considerably faster than for the Alpha due to the direct connection

to a fast, efficient, local RAID[2] array for file storage. The number of channels to be processed is ∼10 times larger for EOS, and these channels are output at an ∼12 times higher rate.

Simply scaling the CPU time up by the increase in data volume and down by the estimated performance increase of the SGI compared to the Alpha indicates that about 3 minutes of CPU time is required to process a day's worth of EOS MLS data. We justify this simple scaling as follows. For the filter spectrometer channels the nominal UARS and EOS Level 1 calibration windows encompass a similar number (∼60) of space reference views for quadratic interpolation during radiometric calibration processing. Since all other aspects of processing for each channel are also very similar, scaling is felt to provide a highly reliable metric for estimating these processing requirements. The DACS represent the only completely new processing of significance compared to UARS. For the filter spectrometers each channel is examined individually by the Level 1 software to look for unexpected gain changes or abnormally high reference χ^2, since each channel has its own failure mechanisms. This is not the case for the DACS because of their digital implementation, and eliminates much of the processing that takes place for the filter channels before radiometric calibration is performed. Gain determination for each DACS is from a single filter channel which monitors its full RF input power. The unique processing steps performed on the DACs data consist of converting each measured autocorrelation into an estimate of the true (multi-bit) autocorrelation, and the subsequent Fourier transform into the frequency domain. The conversion is relatively straightforward, and care has been taken in the design of the DACS to ensure that the transform is efficient. This has been accomplished by providing 129 lags in each DACS which results in a 256 element vector[3] being transformed, very efficient using an FFT. We estimate that the combined overhead of the various DACS processing steps is less than that required for processing an equivalent number of analog filter channels, but for this work assume that the cost of processing a single filter and DACS channel is the same. This will be verified as soon as DACS data are available, either from future EOS MLS brassboard models or SLS prototypes currently in house.

We estimate I/O time by assuming a sustainable transfer rate to and from the local disk storage of $10\,\mathrm{MB\,s^{-1}}$ (a single 100 Mbit Ethernet channel to a local RAID system, as on the current EM SCF system). If we assume that input data are read once and output files written and read once (the read being to derive diagnostic information such as baseline spectra), then ∼10^{10} bytes total are transferred to and from the disk storage in the processing of one day's data. At a $10\,\mathrm{MB\,s^{-1}}$ transfer rate this implies ∼17 s of I/O time. We thus estimate ∼20 minutes of wall clock time to process a single day of EOS MLS data at Level 1, very similar to the current figure for UARS MLS.

The above arguments do not take into account improvements in processing power in the time between now and production processing, nor the increase in processing speed attainable through the addition of more processors. Similarly, disk I/O speed can, and will, be substantially increased by increasing the number of connections from the RAID array to the processor system from the current single 100 Mbit non-shared Ethernet path to several (up to 4 possible in the current system), or to even faster IEEE-1394 interconnects expected to

---

[2]Redundant Array of Inexpensive/Independent Disks

[3]The 129 element data vector from each DACS is converted into a 256 element vector for Fourier transforming by appending all but the first and last element of the DACS data in reverse order to the original vector. The returned transform consists of just the real part of the returned data, the imaginary part being all-zero.

be readily available in the timescale of the final SCF. We thus conclude that processing time, including waits for external I/O transactions, will not present any issues or problems.

At the time of launch, based on test results, we expect a full nominal daily Level 1 data set to require less than 2 hours to process using a single dual-processor Linux-based XEON workstation (3.2 GHz processors 2 GB total main memory). Hence we do not currently see any need to actively pursue a parallel processing approach (discussed in the next section). Since the execution time of this software can increase by an order of magnitude if data quality (or instrument characteristics) are 'bad,' we will revisit this issue if necessary based on actual operational data quality. Another potential reason for parallelization would be a later need/desire to reprocess data at a very high rate.

7.6   Speedup through parallel processing

Many areas exist in this software to achieve speedup through parallelism, but it only makes sense to parallelize the portions of the code which produce the largest return for the least effort, and to do this in a portable manner so that the software is not tied to a single processor vendor and family. All appropriate computers for this processing task in the timescale of EOS are likely to be symmetric multi-processor (SMP) systems with substantial shared memory and a small number (8 to 128) of processors. Such systems are available from SGI, HP, IBM, Sun and DEC (now Compaq), and the following discussion directly relates to the SGI Origin 2000, the version of the SCF used for development of this software. Our research indicates that changing to an alternative machine/vendor in the future would be a minor (but undesirable) perturbation, not a major hurdle.

The obvious areas for parallelization are:

1. filter channel radiance calibration and

2. DACS processing.

There are just over 500 filter channels requiring identical processing from raw data numbers into calibrated radiances and uncertainties. This can be thought of as a loop by channel in the source code, and we propose allowing several loop iterations to be performed as separate threads in parallel. There are no dependencies between threads, so this is easy to implement, and the speedup should be largely proportional to the number of available processors.

The DACS can be processed as 4 separate threads (one per DACS), or, more likely, will be processed sequentially with the parallelism at a lower level. The latter approach is likely to be more efficient since one of the main tasks of DACS processing is the FFT for which efficient parallel libraries are likely to exist for all potential computer architectures that could be used for MLS production processing.

The above methods of parallelism will be built into the software from its initial release used with the EM, and further refinements will only be included in the unlikely event that further reduction in processing time is required. This was not done prior to launch simply because it was not found to be necessary.

7.7   Summary

EOS MLS Level 1 processing time is highly dependent on the chosen computer system, but unlikely to exceed 20 minutes of 'wall clock time' to process a day's worth of data[4]. Main memory footprint[5] is likely to be well under 100 MB, daily I/O will be of order 10 GB, and daily output data volume of order 4 GB. It has been shown that I/O traffic can be readily minimized if necessary, and processing algorithms will be implemented to run in parallel where appropriate to make efficient use of available CPU resources. It has also been shown that I/O time dominates, reducing the value of optimization of CPU resources compared to the more significant gains derived from steps taken to eliminate unnecessary I/O and minimize overall I/O. It should be pointed out that the current SCF with 8 GB of RAM is capable of keeping all input and output files memory resident if necessary.

We conclude that the resource requirements of EOS MLS Level 1 software will be reasonable and acceptable, especially since the estimates generated above do not assume any increase in capability over the current version of the SCF.

---

[4]As discussed above, we chose not to parallelize the Level 1 code prior to launch, resulting in anticipated daily processing times of order 2 hours.

[5]A side effect of the decision not to parallel process in the initial launch-ready software is that the main memory requirement has increased to just over 1 GB in order to increase processing efficiency.

Chapter 8

Additional topics relevant to Level 1 data processing

8.1 Quality control and exception handling

It is essential that Level 1 processing software be robust when it encounters unexpected or absent data. Such events will arise during the instrument turn on sequence, from single event upsets which impart errors in telemetered data, and possibly from failures or degradations in instrument hardware. User inputs (from command files or the runstream command string) allow the processing of any engineering or science data to be inhibited. This provides a mechanism for eliminating the processing of data points which display characteristics of such a nature that it is impossible (or not worth) devising software workarounds to deal with them.

This is best explained by an example. Consider the case of an intermittent ambient calibration target temperature sensor which returns occasional bad data. The errors in such data could be so small that the conversion from counts to temperature units presents no problems within Level 1 processing, but since these data are used in conjunction with the data from the other temperature sensors on the target, the radiometric gain calibration algorithms could output incorrect results at a level which impacts science data quality. The approach taken on UARS to handle data hits in calibration target temperature telemetry, and which will be used in this software, is to compare the temperatures reported by all related temperature sensors and reject any readings which lie outside of a predetermined scatter range. This action is also reported in the Level 1 log file so that the situation can be examined off-line to determine whether the sensor should be declared bad. To date no engineering sensors have failed or even noticeably degraded on UARS, but occasional data hits, attributed to single event upsets, have been observed in such data as that from the calibration target temperature sensors and the antenna shaft angle encoder.

Engineering data is generally processed by a limited set of software procedures (functions) which perform conversions of calibration and monitor point data sets into engineering units such as Volts, Amps and Celsius. For each specific monitor point there will exist a database entry which defines the upper and lower limits for both the calibration readings and the datum being converted. If any of these limits are violated, the data point will be marked as 'bad' and a log file entry generated.

For limb radiance measurements Level 1 processing makes no sophisticated attempts to

determine data validity other than declaring radiances outside the approximate range -80 to +400 K to be 'bad,' and rejecting baseline radiances outside of ranges set by user inputs. Note that the range of the expected noise on individual calibrated limb radiances is large due to the wide range of channels noise bandwidths (~ 0.2 to $500\,\mathrm{MHz}$), and the 'acceptance limits' for calibrated radiances will be set on a channel-by-channel basis after early in-flight data has been reviewed. It is possible, and indeed necessary, to perform quality checks on reference measurements before they are used for calibration of the associated limb data. Space view reference measurements are processed to determine their χ^2, a valuable indicator of system stability. This is done by calculating the rms scatter of these measurements against the quadratic fit performed during radiance calibrations. These data have proven extremely valuable on UARS MLS. Space reference measurements which occur more than 6 standard deviations from the interpolating quadratic are rejected, and the fitting process repeated without these data. Ambient target measurement sequences are filtered for data data points similarly.

Other instrument performance parameters which will be determined routinely include system temperatures and time series of interpolated channel space counts and gains. These, together with the full complement of engineering data, serve as valuable quality control information which will be plotted and examined on a daily basis once the instrument is in orbit.

8.2   In-orbit 'tuning' of algorithms

In addition to use of in-orbit data for validation of instrument operation and validation of Level 1 processing discussed further below, in-orbit data provides vital information necessary for fine tuning of some parameters obtained from prelaunch estimates. Important examples of data/algorithms which will be tuned using in-orbit data include:

1. Antenna loss and scattering parameters (ρ and η),

2. gain variation ($\frac{1}{f}$ noise) parameters (breakpoints and slopes),

3. radiometer-to-radiometer relative boresights,

4. instrument frame of reference with respect that of the spacecraft, and

5. baseline characteristics.

Experience with UARS indicates that in most cases simple refinements to prelaunch parameters will arise from analysis of in-orbit data. Relative boresights of the radiometers will be enhanced from study of both routine atmospheric radiances, and signals obtained from those occasions when the moon traverses the antenna FOV. Special scan sequences will be employed to maximize the data return from the moon scans, which only happen a few times a year, and this refinement is likely to improve incrementally as new data are acquired. Refining the algorithms which predict instrument pointing in the Earth's reference frame is also likely to be an incremental process. Baseline characterization is an example where we will assume that EOS MLS behaves much like its UARS predecessor, and careful study of in-orbit data will be required to characterize any idiosyncrasies in the observed data, with relevant algorithms updated based on observations of true instrument behavior.

Another major area in which algorithm tuning may be required concerns unanticipated behavior in instrument data. The approach taken with this software is to build in resilience against expected or likely events such as:

1. a non-standard scan sequence which does not produce enough (or any) radiometric calibration sequences within the calibration window for the algorithms described in Chapter 4,

2. data 'hits' (e.g., from cosmic ray induced single event upsets in electronic components) which create temporary data inconsistencies, and

3. data out of prescribed limits, as will happen during turn-on sequences.

With UARS MLS data characteristics were found to change after more that a year of in-orbit operation due to wear in the bearings of the switching mirror and antenna scanning mechanism. The changes to science data were not handled in an optimal manner by the pre-launch Level 1 software, and changes were eventually made to both on-board instrument software and the ground processing software to minimize, and in some cases eliminate, any impact to science data quality. Such quirks cannot be predicted in advance, and the approach taken here is not to try to anticipate and program against the unlikely, but design and build robust software which can be cleanly and safely enhanced when such behavioral anomalies have been analyzed and characterized.

8.3   Use of Level 1 algorithms in instrument testing

The primary motivations for using Level 1 software with the EM and FM versions of the instrument during instrument integration and testing are to test both the software and the instrument. The EM does not implement the full radiometer or spectrometer complement, but generates every data type to be processed by this software with the exception of that from the DACS. This allows the filter spectrometer radiometric calibration algorithms and all engineering data processing algorithms to be extensively exercised relatively early in the program. Level 1 software will be used to routinely calibrate and catalog the instrument engineering data for both versions of the instrument. Functional verification tests of system noise levels and sensitivity will also exercise the radiometric calibration algorithms for the filter channels, but the 'science' data from many tests will require off line processing unavailable in this software. Such tests include end-to-end spectral sweeps and relative sideband measurements.

We anticipate that the instrument ground test environment will be far more volatile than that seen routinely in orbit, and thus provide an excellent robustness test for this software.

8.4   Validation

Instrument testing is likely to uncover most errors in algorithms or coding of this software, but in-flight data will provide a rich environment for validating many aspects of the instrument, and also many output data products from Level 1, as was the case for UARS MLS. By implication, the validation of data products is also a validation of the algorithms and implementation used to generate them, and the calibration parameters used in the processing algorithms.

Certain features of atmospheric radiances are highly predictable and dependable, providing ideal data for validating both instrument operation and the associated software. When observing the limb at tangents heights of 100 km or more, most filter channels should report radiances close to that of cold space. Conversely, when observing with tangent heights close to, or slightly below, the Earth's surface, most channels will return saturated radiances.

Appendix A

Significant differences from UARS MLS

One of the more significant differences between UARS and EOS MLS is the choice of a continuous scan. This was implemented on EOS MLS to provide radiance measurements more densely spaced in the vertical than for UARS MLS, and thus allow better vertical resolution in retrieved geophysical parameters. The EOS MLS nominal integration time is chosen to provide negligible or acceptable 'smearing' of the FOV during individual integrations. The limb scan is slower in the troposphere and lower stratosphere to provide more observation in these regions of the atmosphere which are currently of greater scientific interest than in the middle and upper stratosphere. The $\frac{1}{6}$ s integration time corresponds to FOV vertical movement at the tangent point of ~ 0.4 km in the troposphere and lower stratosphere, ~ 1 km in the middle and lower stratosphere, and ~ 2.5 km in the mesosphere.

The continuous scan has no impact on Level 1 processing algorithms, but the following instrumental differences result in changes or additions to the software:

1. Two radiometric calibration targets are included in the GHz module instead of a single target as on UARS MLS. One of these targets is thermally well-coupled to the GHz structure and serves as the primary warm reference during in-flight operation. The other target, which is similar in construction (i.e., is not intended to have degraded emissivity), is thermally decoupled from the structure and attached to a radiator patch so that during in-orbit operation it floats to a temperature ~ 20 K below the primary target. This target also contains resistive heaters which allow its temperature to be raised 20–30 K above the temperature of the primary target during ground testing. The power to heat this target is provided internally from the instrument, but this capability will be removed prior to launch. The secondary target thus provides a valuable aliveness test during all phases of ground testing which was not available on the prior instrument. In addition, it serves as a in-flight backup should there be any problem with either the primary target or the Switching Mirror system which prevents use of the primary target.

2. A frequency synthesizer is included in the instrument to allow in-flight spectral calibration of the 11 and 25-channel filterbank spectrometers. This addition is included because of the long design life of EOS MLS (5 years in orbit) compared to UARS MLS (18 months).

3. Four high resolution digital autocorrelator spectrometers (DACS) are included on EOS MLS for accurate mesospheric and upper stratospheric measurements. Although minor in terms of instrument construction, these devices provide approximately half of the data generated by the instrument, and are a significant workload for the Level 1 processing software and hardware.

4. The data transferred from the instrument to the spacecraft for processing on the ground is packet oriented (conforming to CCSDS packetization conventions[1]) as opposed to the fixed timing, fixed record structure generated by UARS MLS. This means that the fixed length record (with fixed location contents) file structure used for the prior instrument at Level 1 is inappropriate, and an HDF structure[2] conforming to EOS Project guidelines will be used for EOS MLS.

From the viewpoint of Level 1 processing the differences between UARS and EOS MLS are generally small. The most significant differences arise from (1) the introduction of the DACS with their completely new processing requirements, (2) the slightly variable length MAF which eliminates some algorithm performance optimizations possible with the fixed length UARS MAF, and (3) the THz radiometer with its unique radiometric gain calibration algorithms which account for LO power changes.

---

[1]Consultative Committee for Space Data Systems.
[2]Hierarchical Data Format.

Appendix B

Heterodyne radiometers and black body radiation

This chapter is taken from Appendix B from [4], modified slightly for inclusion in this document.

The MLS heterodyne radiometers receive power $h\nu/\{exp(h\nu/kt) - 1\}$ per unit frequency range when viewing a black body source which completely fills their FOV, where ν is frequency, h is Planck's constant and k is Boltzmann's constant. Our objective here is to relate the power received by a coherent (heterodyne) radiometer to the temperature of a black body which completely fills its FOV. By 'coherent' we mean that electromagnetic radiation is coupled to the radiometer in a manner which preserves its phase — this places constraints on the modes which are received and influences the effective area of the aperture which 'collects' the radiation. Let $I_\nu(\theta, \phi)$ be the intensity (Watts Hz^{-1} m^{-2} ster^{-1}) of unpolarized radiation incident upon a collecting aperture from direction (θ, ϕ). The power in frequency interval $d\nu$ delivered through the aperture to a single-polarization radiometer can then be written

$$dP_\nu = \frac{1}{2} d\nu \int_\Omega I_\nu(\theta, \phi) A_e(\theta, \phi) d\Omega ,$$
(B.1)

where $A_e(\theta, \phi)$ is the effective collecting area, the factor of $\frac{1}{2}$ is due the radiometer accepting only one polarization, and the integral is over solid angle Ω.

A general expression for $\int A_e(\theta, \phi) d\Omega$ is derived from considerations of a thermodynamic equilibrium situation. Let the collecting aperture be immersed in a cavity of black body radiation, and let thermal equilibrium be established at temperature T between the black body and the radiation in the transmission line which matches the aperture to the radiometer. If V is volume of the cavity, then the black body radiation intensity is given by

$$I_\nu^{BB} = \left\{ \frac{\mathcal{N}_3(\nu) \langle E \rangle_T}{V} \right\} \left\{ \frac{c}{4\pi} \right\} .$$
(B.2)

The first factor in braces in (B.2) is the average energy per unit volume; the second is the conversion to isotropic radiation intensity with c being the speed of light. $\mathcal{N}_3(\nu)$ is the number of modes per unit frequency interval in the 3-dimensional cavity, and $\langle E \rangle_T =$

$h\nu / \{exp(h\nu/kT)-1\}$ is the average energy in a single mode at temperature T and frequency ν [e.g., Vol. 3, chap 4 of *Feynman et al.*, 1963]. The thermal equilibrium power in the transmission line within the frequency interval $d\nu$ which is moving <u>toward</u> the aperture is

$$dP_\nu^T \quad = \quad \left\{\frac{\mathcal{N}_1 \langle E\rangle_T}{L}\right\}\left\{\frac{v}{2}\right\} d\nu \quad ,\tag{B.3}$$

where L is the line length. The first factor in braces in (B.3) is the average energy per unit length in the line, and the second converts it to power moving toward the aperture where v is propagation speed in the line (in equilibrium, half the power moves toward the aperture and half moves away from it). $\mathcal{N}_1$ is the number of modes per unit frequency, and $\langle E\rangle_T$ is the same as in (B.2) since the average energy per mode at thermal equilibrium depends only on temperature and frequency. In thermal equilibrium the transmission line power moving toward the aperture will equal that collected from the radiation field by the aperture and delivered to the line. Setting (B.3) equal to (B.1), and using (B.2) for $I_\nu(\theta,\phi)$ which can be taken outside the integral since the black body radiation is isotropic, leads to

$$\int_\Omega A_e(\theta,\phi)\, d\Omega \quad = \quad 4\pi\, \frac{v}{c}\, \frac{\mathcal{N}_1/L}{\mathcal{N}_3(\nu)/V} \quad .\tag{B.4}$$

Using (B.2) and (B.4) in (B.1) gives, for a black body source,

$$\frac{dP_\nu^{BB}}{d\nu} \quad = \quad \langle E\rangle_T \frac{\mathcal{N}_1}{L} \frac{v}{2} \quad .\tag{B.5}$$

The significant difference between (B.5) and (B.3) is that (B.3) requires the transmission line to be in thermal equilibrium with the black body, whereas (B.5) does not. Heterodyne radiometers, such as in MLS, use a 'single mode' transmission line for which $\mathcal{N}_1 = 2L/v$, so (B.5) becomes

$$\frac{dP_\nu^{BB}}{d\nu} \quad = \quad \langle E\rangle_T \quad ,\tag{B.6}$$

$$= \quad h\nu / \{exp(h\nu/kT) - 1\} \quad ,\tag{B.7}$$

which is the relation between the black body temperature and the power per unit frequency received by a heterodyne radiometer whose FOV is completely filled by the black body.

Although it is not needed for the above derivation, the number of modes per unit frequency for a 3-dimensional blackbody cavity of volume V is $\mathcal{N}_3(\nu) = 8\pi\nu^2 V/c^3$. When this and the expression given above for $\mathcal{N}_1$ are used in (B.4), we obtain

$$\int_\Omega A_e(\theta,\phi)\, d\Omega \quad = \quad c^2/\nu^2 \quad = \quad \lambda^2 \quad ,\tag{B.8}$$

where λ is wavelength of the radiation. By invoking detailed balancing at thermal equilibrium (the principle that equilibrium must apply to *each* frequency, direction and polarization [e.g., section 9-15 of *Reif*, 1965]), and using the preceding arguments leading to equation (B.4), the effective aperture area for collecting radiation from direction (θ,ϕ) is shown to be given by

$$A_e(\theta,\phi) \quad = \quad \frac{\lambda^2}{4\pi} G(\theta,\phi) \quad ,\tag{B.9}$$

where $G(\theta, \phi)$ is the aperture's angular 'gain'. (If unit power is delivered to the aperture by the line, the amount radiated within solid angle $d\Omega$ in direction (θ, ϕ) is $G(\theta, \phi)\, d\Omega/4\pi$). Note that $\int G(\theta, \phi)\, d\Omega = 4\pi$, as follows from using (B.9) in (B.8). Combining (B.1) and (B.9) gives

$$dP_\nu \;\; = \;\; d\nu \, \frac{1}{4\pi} \, \int_\Omega \dot{I}_\nu(\theta, \phi)\, G(\theta, \phi)\, d\Omega \;\; , \tag{B.10}$$

where

$$\dot{I}_\nu \;\; = \;\; \frac{1}{2} \lambda^2 \, I_\nu \;\; . \tag{B.11}$$

Equation (B.10) is applied several places in this document. Equations (B.8), (B.9) and (B.10) describe general properties of coherent radiometer systems. The derivations given here are based on notes from classes taught by A.H. Barrett and D.H. Staelin at the Massachusetts Institute of Technology.

References

Feynman, R. P., R. B. Leighton, and M. Sands, *The Feynman Lectures on Physics*, Addison-Wesley, New York, 1963.

Reif, F., *Fundamentals of Statistical and Thermal Physics*, McGraw-Hill, New York, 1965.

Appendix C

Calibration and noise

In this appendix we discuss the effects of noise on a total power measurement system such as EOS MLS. The familiar expressions for the sensitivity of an individual measurement are derived, and extended to allow for the effects on calibration measurements of gain variations which increase in spectral density with decreasing frequency, usually referred to as '$\frac{1}{f}$' noise. The following discussion builds largely on a prior work describing the sensitivity of total power radiometers with periodic calibration [5], and retains similar terminology. It should be noted that the description which follows does not relate exclusively to total power measurements systems, but is applicable to *any* measurement system which combines discrete calibration/reference and scene measurements.

In the interests of keeping the mathematical expressions compact and comprehensible, the assumptions are made that gain variations between calibration measurements are small compared to the random noise on an individual measurement, and that the noise on a single reference measurement is of the same magnitude as the noise on a single Limb measurement. The first assumption is reasonable for an instrument with the characteristics expected for EOS MLS, and the second is removed in the algorithms implemented for Level 1 processing.

In the latter part of this appendix we discuss the partitioning of the uncertainties in calibrated radiance into two components: a random component which appears as noise on the spectral contrast in a measured spectral feature; and a correlated component which appears as an overall gain variation which primarily serves to create uncertainty in the absolute value (offset) of an observed spectrum. These two components are determined separately during Level 1 processing to suit the needs of Level 2 retrieval algorithms.

C.1   Description of the measurement system

MLS integrates and digitizes observed radiances with constant integration times, equally spaced in time. A nominal measurement sequence consists typically of a set of Limb (L) integrations lasting 20 s followed by measurements viewing the Space port (S) and internal ambient Calibration Target (C). Space measurements are of duration $\sim$2 s, and Target measurements $\sim$1 s. All measurements are broken into short, regularly spaced and fixed duration intervals called Minor Frames (MIF) of nominal duration $\frac{1}{6}$ s, and the entire measurement sequence is repeated once every Major Frame (MAF), of nominal duration 24.7 s. MAFs are of sightly varying duration (but always comprise an integer number of MIFs) to accommodate their synchronization to the spacecraft orbital period, and there is a delay consisting of

a small integer number of MIFs as scan and switching mechanisms transition between Limb, Space and Target views. Further details were provided in Chapter 1 of this document.

This timing is shown in Figure C.1 which indicates a single Limb observation together with the most recent preceding and succeeding calibration measurement pairs. Note that all data integrations are of constant duration, and that calibration measurements consist of a sequence of consecutive views. The period between successive data integrations is very small ($\sim 5\,$ms) compared to the data integration time ($\frac{1}{6}\,$s nominal). The start of the first limb data integration following a calibration measurement sequence denotes the start of a MAF. During Level 1 processing we need to determine the estimated reference[1] and gain for each channel at the times of the Limb observations.

It is common practice to express the sensitivity of a total power radiometer in terms of noise equivalent temperature difference, ΔT, given by:

$$\Delta \text{T} = \text{T}_{\text{sys}} \sqrt{\frac{1}{B\tau} + \left(\frac{\Delta G}{G}\right)^2} \tag{C.1}$$

where:

T$_{\text{sys}}$ is the system temperature, commonly provided by a Y-factor (hot/cold load) measurement,

---

[1]For this discussion we assume that only the Space reference measurements are to be interpolated to the times of the Limb measurements, but in practice the software is structured to allow either Space or Target views to be selected as the primary reference to be differenced from the Limb measurements.
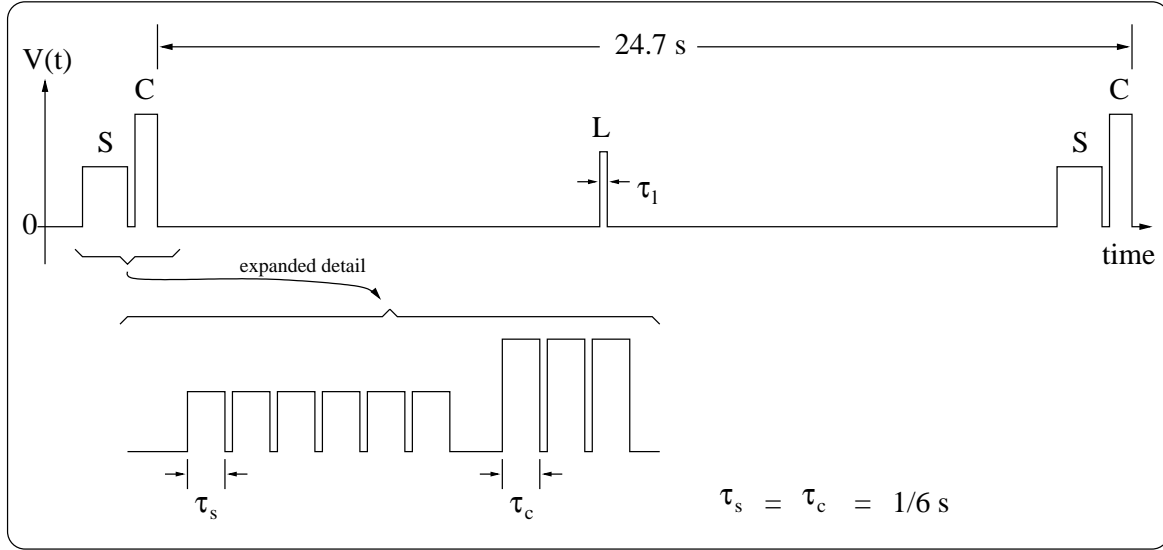
Figure C.1: Figure showing the relative output voltages and nominal timings for a single Limb observation (L) and adjacent sequences of Space (S) and ambient Calibration Target (C) reference observations. The vertical axis represents the output from a spectrometer channel, which in the case of EOS MLS is a digitized quantity. The lower portion of the figure expands the calibration views to show that they consist of sequences of data integrations, all of which are of the same duration (i.e., $\tau_l = \tau_s = \tau_c$). The interval between successive data integrations is greatly exaggerated.

B is the predetection noise bandwidth of the measurement channel,

τ is the postdetection integration time of the measurement, and

$\frac{\Delta G}{G}$ represents the normalized rms fluctuation of radiometer power gain.

Although this equation indicates the noise on an individual signal integration, it ignores completely the effects of low frequency noise on the calibration measurements used in the determination of calibrated radiance. For a system with $\frac{1}{f}$ noise the full relationship between ΔT and T_{sys} clearly needs to include details of the timing of the calibration measurements with respect to the limb measurement, and also details of the noise power spectrum.

A simple illustration of this measurement system is shown in Figure C.2 in which the radiometer response function (H) and channel noise power (S_r) are shown as a function of frequency. Two points must be clearly understood in this figure; the horizontal axis indicates frequency in spectrometer post-detector *output* domain, not the radiometer input domain, and $H(f)$ is a power response function derived from the function which provides the estimate of the difference between a Limb measurement and its surrounding reference measurements (calibration filter).

To illustrate this more clearly, consider the simple measurement sequence shown in Figure C.3 in which a single limb measurement is differenced from the next Space reference measurement. Both measurements are single MIF integrations (i.e., $\tau_l = \tau_s = \tau$) with the Limb measurement centered at $t = 0$ and the reference measurement at $t = T$. These measurements are combined to determine their difference by subtracting the reference signal from the Limb signal, shown by the weightings in the lower half of the figure. The estimate of Limb minus reference signal difference is given by the filter shown in the lower half of the figure. These weightings also represent the integration periods for both measurements, and
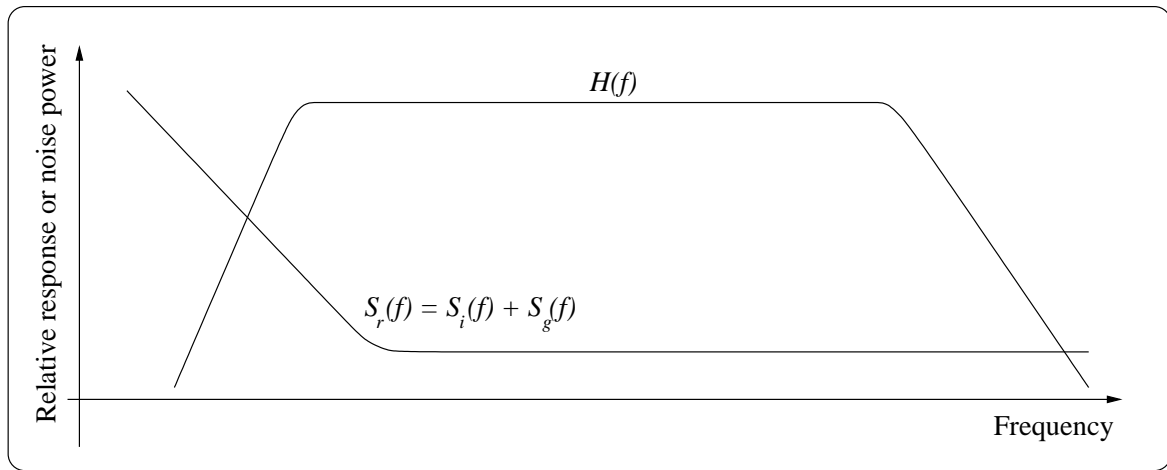
Figure C.2: Simplified representation of the noise power spectrum, $S(f)$, and the calibration filter power response function, $H(f)$, in the post-detector frequency domain. The noise power spectrum has 2 components; a frequency independent (white noise) component $S_i(f)$ and a '$\frac{1}{f}$' component $S_g(f)$. The calibration filter response function, $H(f)$, is highly idealized, but displays the essential characteristics that its response falls to zero at DC and as frequency tends to infinity.

for an input signal $e^{2\pi ift}$, the output, $R(f)$, of the calibration filter is given by:

$$R(f) = \frac{1}{\tau} \left(\int_{-\frac{\tau}{2}}^{+\frac{\tau}{2}} e^{2\pi ift} \, dt - \int_{T-\frac{\tau}{2}}^{T+\frac{\tau}{2}} e^{2\pi ift} \, dt \right) \tag{C.2}$$

The normalization factor $\frac{1}{\tau}$ is included to indicate that we require unity DC input to an integrator for unit time produces unity output. The right hand side of this equation evaluates to produce

$$R(f) = \frac{\sin(\pi f\tau)}{(\pi f\tau)} - \frac{\sin(\pi f\tau)}{(\pi f\tau)} e^{2\pi ifT} \tag{C.3}$$

where the sinc functions arise from the integrator responses and the phase factor is a result of the temporal separation (by time T) of the two integrations.

The desired radiometer response function for noise power, $H(f)$, is simply the squared magnitude of $R(f)$, or $R(f)R^*(f)$.

To be useful the calibration filter must include more information than just that from the closest reference view. In practice we combine the data from several reference views enclosing the Limb measurement to obtain a lower noise estimate of the reference at the time of the Limb view.
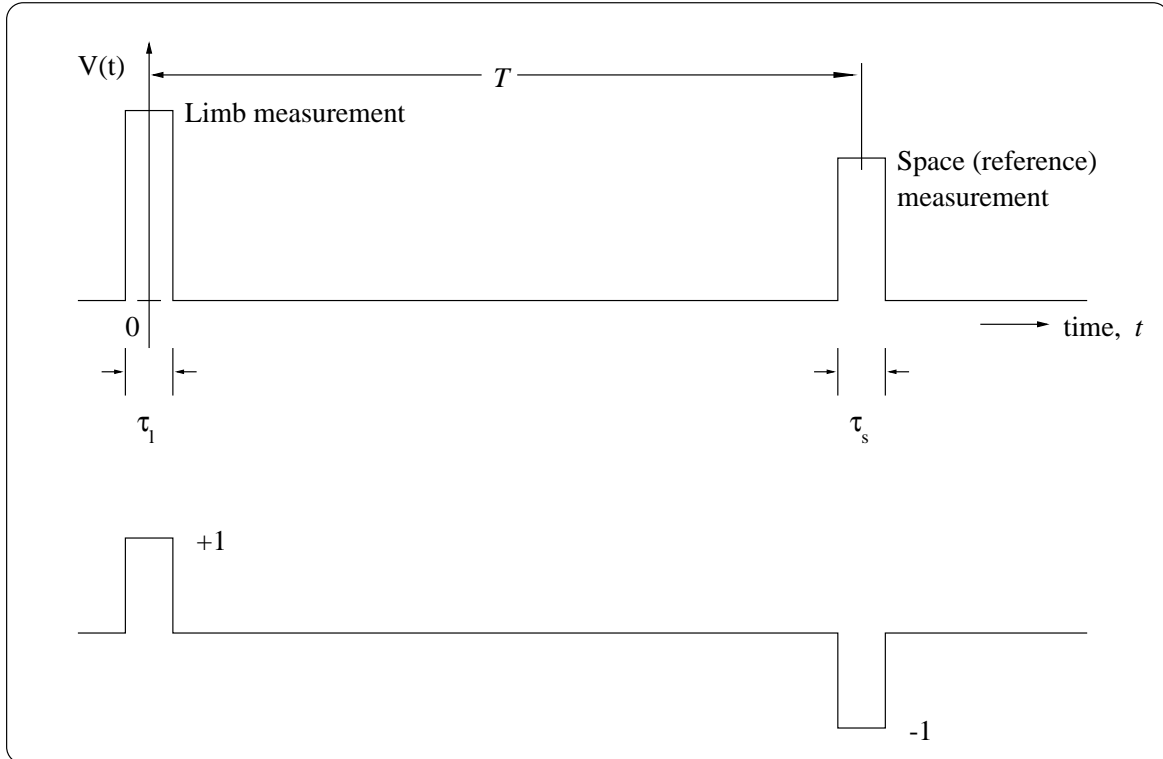

Figure C.3: The upper plot indicates the output of a channel while viewing the Limb (at $t = 0$) followed by a view to the Space reference (at $t = T$). The lower plot indicates the relative weightings applied to the two measurements by a simple calibration filter which merely differences the two measurements.

Equation C.2, and the corresponding expression for $H(f)$, are readily extended for the case in which multiple reference views are combined and differenced from a single Limb measurement:

$$H(f) = \left| \text{sinc}(\pi f \tau) - \text{sinc}(\pi f \tau) \sum_k w(t - kt_c) e^{2\pi i f(t - kt_c)} \right|^2 \qquad (C.4)$$

where the factors w represent the weighting applied to each reference measurement, and for convenience of representation we have assumed that all reference measurements are equally spaced in time (by time t_c) and symmetrically disposed about the single Limb measurement. The weights are subject to constraints which ensure that they produce the desired interpolate, discussed in the next chapter.

The noise power, $(\Delta T)^2$, in a single Limb measurement is given by the convolution of the post detector noise power spectrum, $S(f)$, and the power response of the post-detector system, $H(f)$:

$$(\Delta T)^2 = c^2 \int_0^\infty S_r(f) H(f) \, df \qquad (C.5)$$

where c is the channel gain, usually expressed in units of Kelvin per volt, or, in the case of EOS MLS, Kelvin per count. Minor assumptions which have been made, both of which are reasonable for EOS MLS, are:

1. the noise in c has been neglected, and

2. the noise power spectrum has been assumed to be the same for both signal and reference views.

From the Radiometer Equation we can directly infer $S_i(f)$, the 'white noise' component of radiometer noise:

$$S_i(f) = \frac{2T_{sys}^2}{B} \quad \text{for } 0 \le f \ll B \qquad (C.6)$$

In this representation $S_i(f)$ is in units of K^2, and the factor of 2 in the numerator accounts for the relationship between post-detection integration time and post-detection noise bandwidth ($B = \frac{1}{2\tau}$). The condition on bandwidths given to the right of this equation is discussed further in Appendix F. Combining previous results gives:

$$\left(\frac{\Delta T}{T_{sys}} \right)^2 = \frac{1}{B\tau} + \frac{1}{B\tau} \sum_k w^2(t - kt_c) + \left(\frac{\Delta G}{G} \right)^2 \qquad (C.7)$$

where the left hand term on the right hand side of this equation gives the white noise contribution from the Limb measurement, the center term gives the white noise term on the combined reference measurements, and the right hand term gives the '$\frac{1}{f}$' contribution to the Limb/reference difference. The gain variation term is given by:

$$\left(\frac{\Delta G}{G} \right)^2 = \left(\frac{c}{T_{sys}} \right)^2 \int_0^\infty S_g(f) H(f) \, df \qquad (C.8)$$

where $S_g(f)$ represents the noise component with non-white spectral density.

C.2   Correlated and uncorrelated noise

For Level 2 processing needs it is convenient to separate the uncertainty contributions generated by the spectrally flat and $\frac{1}{f}$ components of $S(f)$. Analyses of radiances which rely solely on spectral contrast are influenced almost entirely by the spectrally flat noise component, while analyses which depend upon accurate knowledge of absolute radiances need to include the uncertainty contribution arising from gain variations, given by the $\frac{1}{f}$ component.

We refer to the uncertainty generated by spectrally flat noise as 'uncorrelated noise,' and compute this during Level 1 processing for each individual limb radiance. The 'correlated noise' arising from gain variations is assumed to be identical for all channels of a given radiometer (this will be tested on the EM and FM versions of the instrument), and computed as an uncertainty vector for each active radiometer. The elements of this vector are single numbers for each MIF of the current MAF record, and the correlated noise for a given limb radiance is determined by multiplying the sum of the system temperature and calibrated limb radiance by the vector element corresponding the the MIF during which the limb measurement was made.

The form of correlated and uncorrelated uncertainties during a MAF is similar, shown in Figure C.4. The uncertainties are smallest for limb radiances measured close to reference measurements, and largest for measurements made approximately mid-way between reference measurements. For analyses which rely upon the absolute values of observed radiances it is necessary to combine both sources of error (in quadrature) to obtain the total estimated uncertainty. In order to determine these noise contributions separately we make some minor approximations, discussed below.
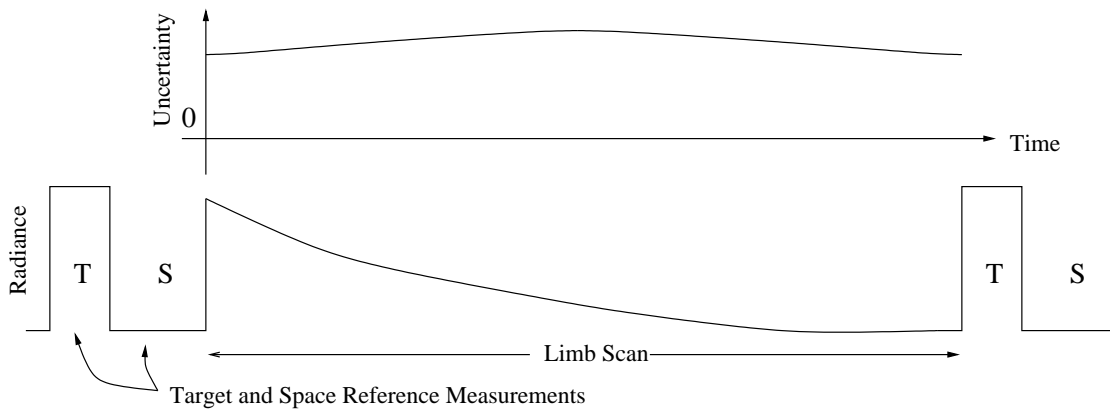
Figure C.4: Figure showing the behavior of radiance uncertainties arising from both correlated and uncorrelated sources. The uncertainties are seen to be smaller for limb radiance measurements made closest to the reference measurements, and largest for measurements mid-way between reference measurements. It is assumed for this figure that T_{sys} is much larger than any observed radiance, resulting in an uncertainty plot symmetric about the center of the limb scan. This approximation is not made in Level 1 processing.

C.2.1 Uncorrelated noise

The random noise, ΔT, on an individual radiance measurement is given by

$$\Delta T \approx \frac{(T_{sys} + T_{sig})}{\sqrt{B\tau}} \tag{C.9}$$

The interpolation scheme used to calibrate each limb radiance also includes the noise on the reference measurements, and additional uncertainty due to the interpolation process. These additional noise contributions are much smaller than the noise on an individual limb observation, but are included in the final estimate of the random (spectral) component of uncertainty.

Including these additional sources of noise gives for the estimate of uncertainty:

$$\Delta T = \sqrt{\frac{(T_{sys} + T_{sig})^2}{B\tau} + (\Delta R)^2 + \left(T_{sig} \times \frac{\Delta G}{G}\right)^2} \tag{C.10}$$

This noise estimate is calculated for all channels each measured limb radiance. ΔR is the noise on the interpolated space reference, derived from the error covariances in the quadratic fit used for interpolation, and ΔG is the noise on the interpolated channel gain. It is important not to confuse the right hand term inside the square root which contains the noise-induced uncertainty in channel gain with the similar looking gain variation term discussed earlier (see Section 4.5.1). It is similarly important to note that this expression for uncertainty scales the signal radiance by the noise on interpolated gain, not the sum of signal and system generated signals. The reason for this is that the interpolation of space references has essentially removed the gain variation effects from the data processing to determine spectral contrast. The gain variation component of uncertainty is not ignored, but evaluated and included as part of the determination of absolute radiance uncertainties, described later. The main assumptions made in expressing relative radiance uncertainty using Equation C.10 are

1. that the apodizing function applied to the measurement variances during the quadratic fit used for reference interpolation serves as a low enough bandwidth filter to allow radiometer noise to dominate any $\frac{1}{f}$ components, and

2. that gain variations over the timescale of a MAF introduce scaling errors small compared to ΔT on an individual data integration.

For EOS MLS to meet its sensitivity requirements both of the above conditions will also have to be met. Tests performed on brassboard radiometers and IF subsystems indicate that these requirements will be satisfied.

Each individual calibrated limb radiance produced by Level 1 software and written to the output radiance file includes an estimate of the random component of uncertainty arising from front end radiometer noise calculated using Equation C.10 above.

C.2.2 Correlated noise

The correlated noise determination depends upon knowledge of the $\frac{1}{f}$ characteristics (breakpoint frequency and slope) of the post-detector outputs of the channels of a given radiometer. UARS experience indicates that this can only be determined accurately in the final orbital

operating environment, and [11] describes a method for determining these parameters which separates the effects of orbital harmonics arising from periodic thermal variations from the underlying random gain variations. The expressions for covariance derived in Appendix E (Equations E.13 in particular) then allow the magnitude of this uncertainty source to be computed.

Appendix D

Quadratic interpolation of reference radiance signals

This appendix provides additional material to augment that presented in Section 4.4.1, and in particular clarifies the need for a common weighting function and calibration window for the quadratic reference interpolation used with all channels of a radiometer.

A significant computational task of the Level 1 software is the interpolation of space reference measurements onto the times of the limb and target reference measurements. We ideally require that this interpolation be performed in a manner which minimizes the uncertainty in the interpolated results for each measurement channel. In practice however we must not allow the interpolation to introduce any biases which may create spectral artifacts. This prevents use of an Optimal Calibrator such as the one developed for use with UARS MLS and described in Appendix E. An Optimal Calibrator is one which implements an interpolation scheme which minimizes the variance on the reference interpolates when the measurements are contaminated by $\frac{1}{f}$ noise (typical for gain variations). The description of the Optimal Calibrator is included in this document since it provides a precise description of how to determine the uncertainty (noise) on a calibrated measurement for data with noise characteristics expected for this instrument

The total power measurement scheme used by EOS MLS is described in Appendix C. Key points of relevance to the following discussion are (1) reference measurements are taken periodically in groups, and (2) the temporal separation of these reference measurement groups is of order half a minute.

In order to ensure that the noise on the interpolated reference is substantially lower than that on each individual limb radiance measurement we need to combine the information from several reference measurements during interpolation. The ideal situation is to have reference measurements disposed symmetrically about the limb measurement being calibrated, a situation not achievable in reality, but which is approximated closely enough by combining data from several groups of reference measurements on either side of the limb radiance being calibrated.
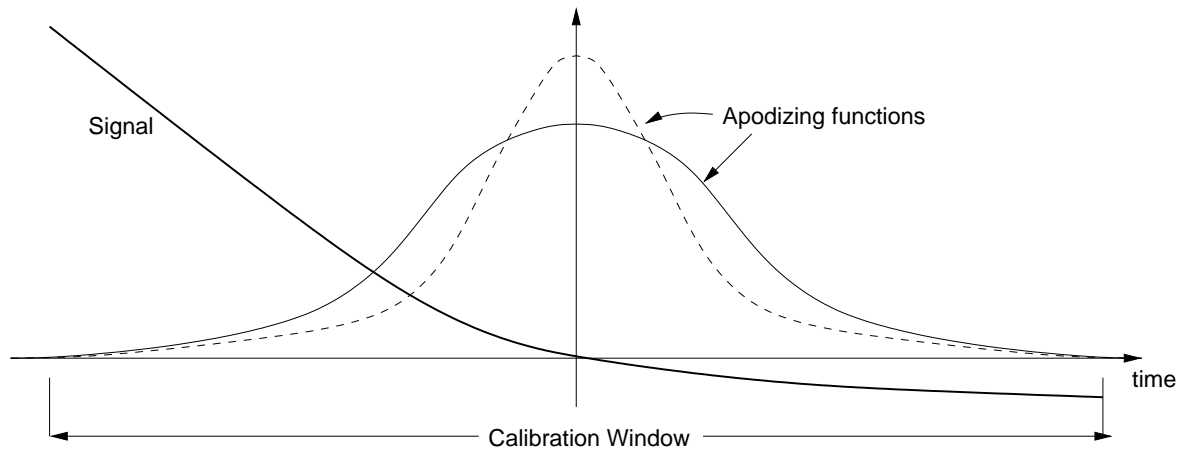
Figure D.1: Figure illustrating a signal with drift and two possible apodizing functions to be applied prior to fitting for interpolation. The vertical axis corresponds to either signal 'counts' or relative apodizing magnitude. See text for details.

D.1   Interpolation and spectral bias

Consider Figure D.1 in which the thick solid curve represents the 'true' reference signal as a function of time, and two different apodizing functions are shown. The two apodizing functions shown differ in halfwidth, the difference in magnitude representing appropriate normalization. The magnitudes of the apodizing functions signify the relative weights applied to the reference measurements during the fitting of the interpolation function to the data. The references are being interpolated onto the time at the center of the plot (i.e., at the location of the y axis), and we size the Calibration Window so that it spans several groups of reference measurements[1].

Assuming that the thick curve labeled 'Signal' represents a contiguous sequence of reference measurements, it can be seen that the mean value of the apodized signal is different for the two different apodizing functions. Both apodizing functions result in a mean signal above the horizontal axis of the example plot, the narrower function giving in a mean signal much closer to the horizontal axis than the broad one. The noise on each measurement comes predominantly from two sources, (1) a spectrally flat random component mainly from the radiometer front-ends, and (2) a component arising from gain variations in the signal chains. The gain variations arise both from thermal changes in the signal paths during the period of the Calibration Window, and from $\frac{1}{f}$ type gain variations in the HEMT amplifiers used as first IF amplifiers in all radiometers. We anticipate that the gain variations will be highly correlated in all channels of a given band, and well correlated even between bands of a given radiometer. This hypothesis is felt to be well founded based on discussions with experts in the field, and will be verified using EM, FM and in-flight data.

An optimal interpolator will select broad apodizing functions for the channels with narrowest predetection bandwidths and narrow ones for the wide channels. For the example

---

[1]The Calibration Window is the maximum time interval over which reference measurements are included when performing the fit to these measurements for interpolation purposes.

illustrated in the figure above the optimal interpolator would bias the estimate of the signal at the time represented by the intersection of the two axes more for narrow than for broad channels. Since individual limb measurements are not interpolated, the limb/reference differences would thus look like an inverted emission spectrum for this example if both signals were spectrally flat (or even if they were both taken looking at a common reference and merely relabeled for analysis purposes). Since most MLS measurements are derived from the spectral contrast in the observed spectrum, this is clearly unacceptable. Note that these biases only arise if the order of the drift in the signal is higher than the order of the fitting polynomial (or constraint order in the case of the Optimal Interpolator). Such drift characteristics may arise for instance when the sun impinges on a previously eclipsed portion of the MLS containing sensitive signal chain electronics.

D.2 Apodizing functions and the length of the Calibration Window

The previous discussion makes it clear that measurements which are derived from spectral contrast of the observed radiances require the use of a common apodizing function for all measurements which are to be used as an ensemble in subsequent data processing (i.e., bands which are 'stand-alone' require use of a single apodizing function for all channels within the band, and bands whose spectral data are combined in some sense require use of a common apodizing function for all channels of those bands).

We strongly desire that the random component of uncertainty on an individual limb radiance be dominated by radiometric noise, and not significantly degraded during radiometric calibration processing by noise on the associated reference measurements. Based on the discussions on noise and calibration in Appendix C, if gain variations do not contribute significantly to uncertainty, we have for the noise on an individual calibrated measurement:

$$\Delta T = T_{sys} \sqrt{\frac{1}{B\tau} + \frac{1}{B\tau} \sum_k w^2(t - kt_c)} \tag{D.1}$$

Space reference measurements occur in contiguous groups of twelve meaning that 24 space reference measurements are used to generate the interpolated estimate of space signal at the time of a limb measurement in the simple case that a linear fit is used with data from adjacent calibration measurement groups. In the equation above this means that a common weighting, w, of $\frac{1}{24}$ is used, resulting in a signal to noise degradation due to noise on the reference measurements of only 2%.

Experience with UARS MLS indicates that we wish to use a larger calibration window than this, and wish to fit to the space references with a quadratic, in order to capture second order components in the signal drifts. The previous arguments also indicate that a short calibration window is appropriate since this minimizes any deleterious effects of $\frac{1}{f}$ noise, and a longer window makes scarcely any improvement in the noise of the calibrated limb radiance. An apodizing function strongly favors calibration measurements closest to the measurement being calibrated, and tapers to a low value for the most distant calibrations is appropriate. The chosen scheme is shown in Figure D.2 below. Further details of measurement timing are given in Appendix C.
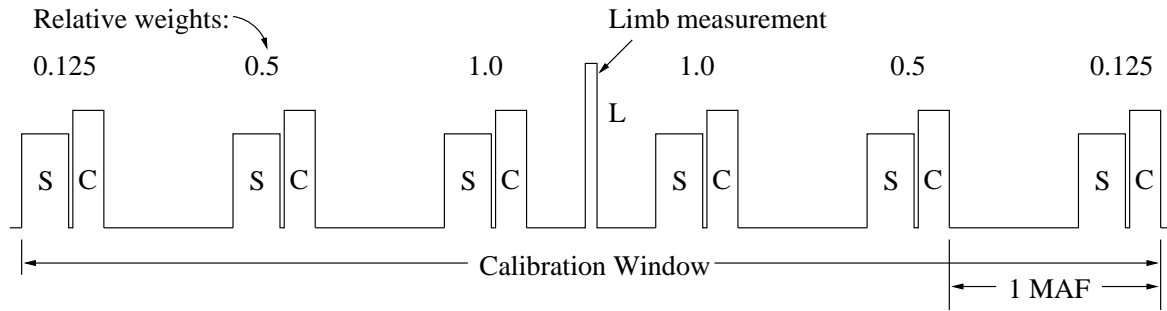
Figure D.2: Figure illustrating relative timings of calibrations used with a given limb radiance measurement. S, C and L represent Space, Calibration Target and Limb views respectively. The Central MAF is the one containing the Limb view being processed. Relative weights are the weightings applied to each calibration measurement when fitting to the calibration sequence for interpolation. Figure is not to scale. See text for additional details.

As shown in Figure D.2, we choose a Calibration Window of 6 MAFs since this provides 3 reference measurement groups in either side of the central MAF of limb radiances being processed. The relative durations of all measurements in the figure are exaggerated for clarity. Relative weightings of 1 and 0.125 are applied to the calibration measurements closest and furthest from the limb measurement being processed, with a weighting of 0.5 for the intermediate calibrations. These weightings may change slightly after data from the EM and FM have been analyzed, but the algorithms given below are unlikely to change.

The short duration of the proposed Calibration Window relative to the one used for UARS MLS data processing ($\sim$1.5 minutes *vs* $\sim$12 minutes) justifies the assumption above that the noise on individual calibrated radiances will be dominated by the spectrally flat component.

D.3 The quadratic interpolator formulated as a sequence of weights

In order to determine absolute radiance errors (Section 4.5.2) it is necessary to express the operation of generating the difference between limb and interpolated reference counts as a sequence of weights applied to each measurement. This calculation is performed off-line as part of the determination of the absolute radiance error multipliers supplied to Level 1 as user inputs, but described here so that the process is documented in a convenient place.

The quadratic least squares fit consists of minimizing the function f given by:

$$f(a, b, c) = \sum_j (a + bx_j + cx_j^2 - y_j)^2 \tag{D.2}$$

where a, b and c are the quadratic coefficients, and x_j are the 'times' at which the measurements y_j were made. To use this equation as an interpolator at 'time' zero we need only determine the value of coefficient a. Note that any measurement sequence can be interpolated onto any time simply by offsetting the time coordinates to define the interpolation point to occur at time zero. The solution for a which minimizes the rms difference between

measurements and model is given in section 4.4.1, and reproduced here in slightly modified form:

$$a = \frac{1}{\Delta} \begin{vmatrix} \Sigma C(j)W(j) & \Sigma jW(j) & \Sigma j^2 W(j) \\ \Sigma jC(j)W(j) & \Sigma j^2 W(j) & \Sigma j^3 W(j) \\ \Sigma j^2 C(j)W(j) & \Sigma j^3 W(j) & \Sigma j^4 W(j) \end{vmatrix} \tag{D.3}$$

where $C(j)$ are the counts and $W(j)$ are the relative weightings given to the measurement at time j, and Δ is a constant for any given measurement sequence. From this relationship we may directly write:

$$\begin{aligned} a'(j) \quad = \quad & \frac{C(j)}{\Delta} \left(W(j) \times \left(\Sigma j^2 W(j) \times \Sigma j^4 W(j) - \Sigma j^3 W(j) \times \Sigma j^3 W(j) \right) - \right. \\ & \Sigma jW(j) \times \left(jW(j) \times \Sigma j^4 W(j) - j^2 W(j) \times \Sigma j^3 W(j) \right) + \\ & \left. \Sigma j^2 W(j) \times \left(jW(j) \times \Sigma j^3 W(j) - j^2 W(j) \times \Sigma j^2 W(j) \right) \right) \end{aligned} \tag{D.4}$$

where

$$a = \Sigma a'(j) = \Sigma w(j)C(j) \tag{D.5}$$

Note that we have now expressed a as a sequence of weights $w(j)$ which can be applied directly to the measurements $C(j)$ (as a dot product) to determine the interpolate of C at time zero (i.e., $j = 0$). A further simplification arises from the recognition that a simple normalization applies to the weights:

$$\Sigma w(j) = 1 \tag{D.6}$$

since we require unit result when applying the weights to a uniform input. The removes the need to evaluate Δ, a significant computational saving.

An important point to note in the expression for w is that the weights do not depend upon the input data at all, only on their position with respect to the interpolation point, and on the relative weighting given to each measurement when performing the fit. Since all measurements in a module (GHz or THz) share the same reference timing, and the arguments given earlier show that a common relative weighting must be given to related measurements, once the vector of weights to be applied to the measurements has been determined, the same vector is then used with the data from all channels sharing the same input weighting to determine the interpolate at a given MIF. This is in sharp contrast with the more conventional approach in which the data dependent coefficients a, b and c are determined for each channel and then used to generate the desired interpolates at each MIF. The conventional approach requires a complex calculation initially, followed by a set of relatively trivial calculations to determine the interpolates. The 'vector of weights' approach described above substitutes a simple calculation that must be repeated for each MIF onto which we are interpolating, but has the additional saving that many channels can share vector w in determining the interpolates.

D.3.1 Relative radiance uncertainty estimate

The noise variance on an individual limb integration, $(\Delta T_{limb})^2$, is given by:

$$(\Delta T_{limb})^2 = \frac{(T_{sys} + T_{limb})^2}{B\tau} \tag{D.7}$$

The noise variance on the interpolated reference measurement, $(\Delta R)^2$, is given by:

$$(\Delta R)^2 = \frac{(T_{sys} + T_{ref})^2}{B\tau} \times \Sigma w^2 \tag{D.8}$$

In Chapter 4 it is shown that the variance contribution from noise on the interpolated gains, $(\Delta T_g)^2$, is given by:

$$(\Delta T_g)^2 = \frac{T_{limb}^2}{B\tau} \times \left(\frac{T_{tgt} + T_{sys}}{T_{tgt} - T_{ref}}\right)^2 \times \Sigma w_g^2 \tag{D.9}$$

where w_g are the normalized weights used to quadratically interpolate the gain measurements onto the times of the limb measurements.

We thus arrive at the following expression for the relative uncertainty on an individual calibrated limb measurement:

$$\Delta T_{rel} = \sqrt{\frac{1}{B\tau}\left((T_{sys} + T_{limb})^2 + (T_{sys} + T_{ref})^2 \times \Sigma w^2 + T_{limb}^2 \times \left(\frac{T_{tgt} + T_{sys}}{T_{tgt} - T_{ref}}\right)^2 \times \Sigma w_g^2\right)} \tag{D.10}$$

Note that T_{ref} is very small compared to the other temperatures in the above expression, allowing it to be ignored without significant loss of accuracy. As a final refinement to this expression, note that in Chapter 4, when determining the gain noise contribution to the radiance error, we omitted the effect of noise on the Space reference interpolates onto the times of the Target measurements. We can readily add this contribution by including the noise on the interpolated Space reference views into the gain uncertainty term as follows:

$$\Delta T_{rel} = \tag{D.11}$$
$$\sqrt{\frac{1}{B\tau}\left((T_{sys} + T_{limb})^2 + (T_{sys})^2 \times \Sigma w^2 + T_{limb}^2 \times \left(\frac{T_{tgt} + T_{sys}}{T_{tgt}}\right)^2 \times (1 + \Sigma w^2) \times \Sigma w_g^2\right)}$$

where we have omitted the small T_{ref} contributions. We may write this expression in terms of Counts as follows:

$$\Delta T_{rel} = \frac{1}{g\sqrt{B\tau}}\left((C_{limb} - C_{zero})^2 + (C_{ref} - C_{zero})^2 \times \Sigma w^2 + \right.$$
$$\left. (C_{limb} - C_{ref})^2 \times \left(\frac{C_{tgt} - C_{zero}}{C_{tgt} - C_{ref}}\right)^2 \times (1 + \Sigma w^2) \times \Sigma w_g^2\right)^{\frac{1}{2}} \tag{D.12}$$

where g is the estimate of channel gain in Counts per Kelvin at the time of the Limb measurement, and we have used C_{ref} as a convenient surrogate for the Counts to be expected when viewing a hypothetical scene of zero radiance. Note that C_{limb} is the actual channel count at the time of the Limb measurement, whereas all other counts (C_{zero}, C_{ref} and C_{tgt}) are interpolates of these measurement types at the time of the Limb measurement. The expression above is the one used in Level 1 software to estimate radiance uncertainty. Space and Target measurements are interpolated onto the times of each Limb measurement, and Σw^2 and Σw_g^2 are the sum of the squares of the Space and Target interpolation weights respectively.

D.4   Some examples

The operation of the weights-based interpolator is best clarified by some examples of the weight sequences arising for anticipated interpolation scenarios. Figure D.3 closely simulates the nominal measurement sequence planned for EOS MLS with consecutive groups of 12 MIFs devoted to observation of cold space. These reference groups repeat every 149 MIFs, and, as can be seen from the figure, 6 groups of reference measurements are included in the fit for the interpolation. The relative weighting given to the input data falls off exponentially with temporal distance from the MIF onto which the references are being interpolated with a $\frac{1}{e}$ length of 150 MIFs, corresponding to the description in Section 4.4.1.

The upper left panel shows the absolute weights applied to the reference measurements when interpolating onto the MIF in the precise center of the reference measurement sequence. The quantity Σw^2 in the panel is the sum of the squares of the interpolation weights, and indicates the square of the noise contribution from the interpolated reference (where unity would indicate that the reference noise contribution was of the same magnitude as the noise on a single low radiance limb measurement). The upper right panel shows the weights applied to the reference measurements to generate the interpolate for a MIF adjacent to one reference measurement group. Note that the noise on the interpolated reference is slightly larger than in the previous case.

The lower two panels give the weights for generating an interpolate just beyond and well beyond the rightmost reference measurement respectively. Note the huge increase in the uncertainty on the interpolate as the quadratic is used as an extrapolator instead of an interpolator.

D.5   Non-standard measurement sequences

It is necessary for Level 1 software to operate robustly even when the measurement sequence departs radically from nominal. Non standard sequences will occur during pre-launch instrument testing and characterization, and will occur in flight when scan programs are being updated or special test are being performed. Experience with UARS MLS indicates that the primary conditions that must be accounted for are:

1. a continuous sequence of measurements of one type (e.g., as when staring at the Space or Calibration Target port for extended periods in order to derive stability characteristics from off-line analyses, and

2. a Calibration Window containing insufficient (or no) reference measurements for processing of Limb data in the Central MAF.

It is imperative that Level 1 software be robust under all instrument operating conditions, i.e., that it continue to run even when the instrument is operating in a mode such that limb data cannot be calibrated (e.g., when staring at the internal calibration target for an extended period such as when characterizing signal chain stabilities).

This is handled primarily by performing extensive sort and qualify operations on all data within the calibration window prior to processing the central MAF. Once this has been done radiometric calibration is only performed if adequate calibration data exists within the calibration window. If insufficient or no calibration data is present, previous calibration data

(if present) are extrapolated and used. When the estimated uncertainty on the extrapolated data exceeds preset thresholds (set by default data files), default data are used instead, and the radiance data flagged as 'bad' by being tagged with a negative radiance error.

The instrument has a range of operating conditions which represent a 'standard operating mode,' and for which Level 1 processing will operate seamlessly. This range is set by the allowable range of MIF and MAF durations, and by the presence of a radiometric calibration sequence at least once per MAF. Non-standard measurement sequences may violate these conditions, typically by the absence of the full radiometric calibration sequence for an extended period of time. These sequences are intended to provide data which will be derived directly from the Level 0 data files using analysis tools developed expressly for that purpose.
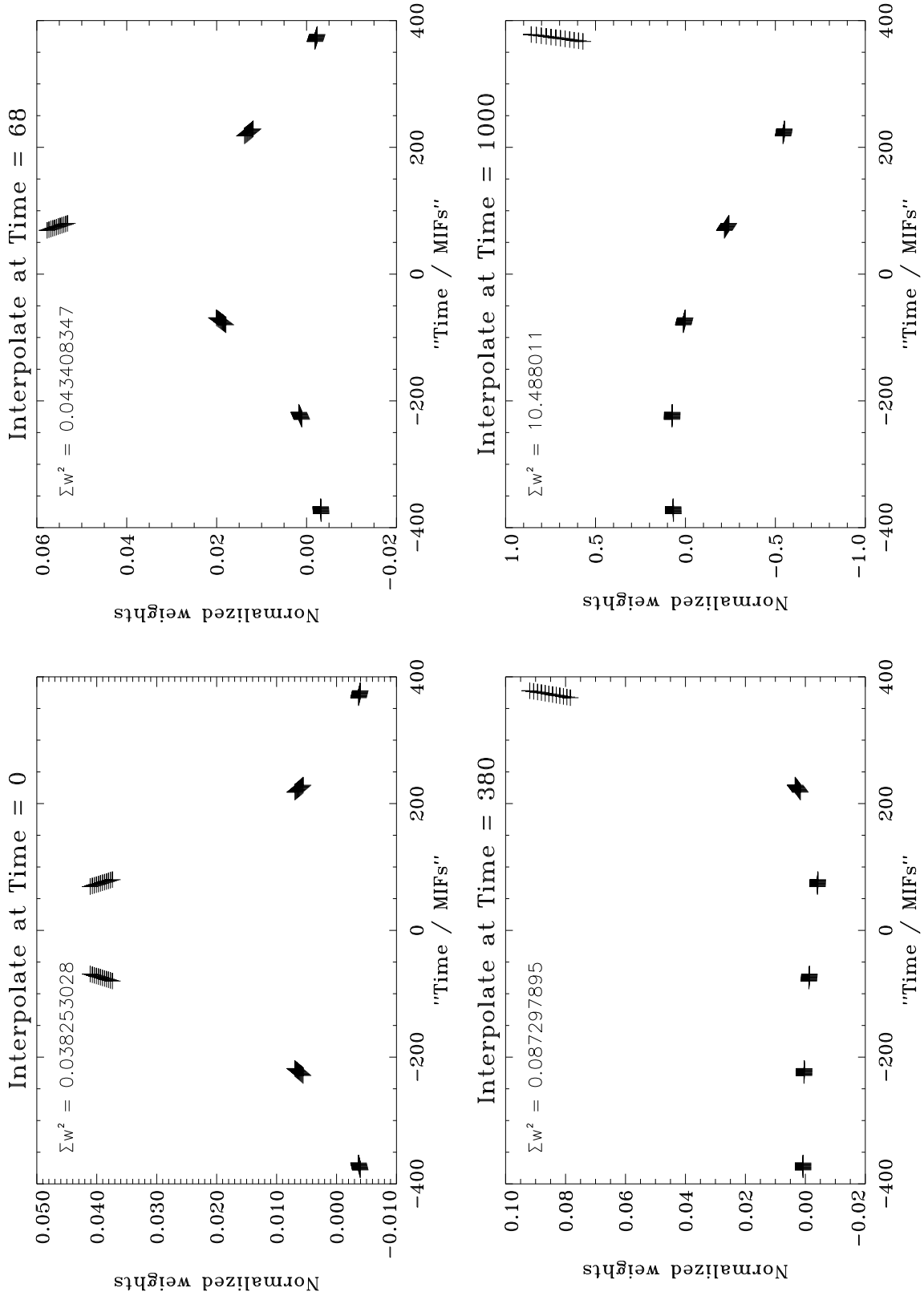
Figure D.3: These panels show the weights applied to reference measurements (as a dot product) to determine interpolates at 'times' 0, 68, 380 and 1000. See text for additional details.

Appendix E

Optimal interpolation of reference radiance signals

The appendix describes the Optimal Calibrator developed by Peckham, described in [6], and adheres closely to the content and terminology used therein. This work led to the development of algorithms, given below, which evaluate calibrated limb radiances with minimum variance. It was shown in the previous appendix that such algorithms can lead to spectral bias, precluding their use with EOS MLS data during routine Level 1 data processing. The description below is included in this document because it provides the key algorithms necessary for determination of the coefficients to be used in Level 1 processing to determine the magnitude of the absolute radiance uncertainties. These coefficients will be determined with off-line (non-production) analyses of in-orbit data, and presented to Level 1 software as user inputs.

E.1 Filter weights and constraints

Combining Equations C.7 and C.8 gives

$$\left(\frac{\Delta \mathrm{T}}{\mathrm{T_{sys}}}\right)^2 = \underbrace{\frac{1}{B\tau}}_{1} + \underbrace{\frac{1}{B\tau}\sum_k w^2(t - kt_c)}_{2} + \underbrace{\left(\frac{c}{\mathrm{T_{sys}}}\right)^2 \int_0^\infty S_g(f)H(f)\,df}_{3} \tag{E.1}$$

For a given channel noise bandwidth and integration time, the noise on a single uncalibrated Limb integration (term 1) is set by the system temperature, $\mathrm{T_{sys}}$. The noise on the interpolated reference views due to system temperature (term 2) is dictated by the relative weights (w) applied to each reference measurement. In the absence of low frequency noise and gain fluctuations we would choose to interpolate using a large number of reference measurements, allowing the noise on the interpolated reference to be very small compared to the noise on the Limb integration. The power response of the calibration filter in term 3, $H(f)$, is of course a function directly related to the weights. As the temporal span covered by the calibration filter increases, the filter accepts more of the noise which increases in spectral density with decreasing frequency. The goal is to determine the set of weights, w, which minimize the right hand side of Equation E.1 while simultaneously providing the desired interpolates of the reference sequence.

E.2 Constraints

Before the set of weights which minimize the right hand side of Equation E.1 can be determined, it is necessary to determine the constraints to which they are subject. In the general case in which we wish to determine the difference, D_T, between a set of M Limb measurements (S_m) and K reference measurements (C_k), we define the following filter

$$D_T = \sum_{m=1}^{M} v_m S_{m+T} - \sum_{k=1}^{K} w_k C_{k+T} \tag{E.2}$$

where D_T represents the smoothed output sequence (at time T) with any zero level (offset) removed. It should be noted that the reference sequence is typically chosen to be longer than the scene measurement sequence, and disposed as symmetrically as possible about it. In the case that all signals are time independent, and $S_m = C_k$, the output of the filter should be zero, requiring

$$\sum_{m=1}^{M} v_m = \sum_{k=1}^{K} w_k. \tag{E.3}$$

Since we require drifts and low frequency gain variations to cause only slow variations in signal levels over timescales of several MAFs, it is appropriate to approximate drifts by a low order polynomial of order R in time, where $R = 2$ or 3 is likely to suffice. We may represent the signal S (or C) by

$$S = \sum_{i=0}^{R} a_i t^i \tag{E.4}$$

(where t is the time of the center of the integration for measurement i) which combines with E.2 to give

$$\sum_{m=1}^{M} v_m \sum_{i=0}^{R} a_i t_m^i = \sum_{k=1}^{K} w_k \sum_{i=0}^{R} a_i t_k^i. \tag{E.5}$$

The summations may be rearranged to give (my thanks to Dr. Nathaniel Livesey for this suggestion):

$$\sum_{i=0}^{R} a_i \sum_{m=1}^{M} v_m t_m^i = \sum_{i=0}^{R} a_i \sum_{k=1}^{K} w_k t_k^i \tag{E.6}$$

which implies

$$\sum_{m=1}^{M} v_m t_m^r = \sum_{k=1}^{K} w_k t_k^r \quad \text{for} \quad r = 0 \,..\, R \tag{E.7}$$

This result is readily obtained for the case $R = 2$ by subtracting Equation E.3 from the appropriate expansion of Equation E.6. The proof for successively higher orders of R is obtained by incrementally increasing the value of R in the expansion of Equation E.6 and subtracting the constraints determined by the prior evaluations for lower orders.

For EOS MLS we have chosen to calibrate each Limb radiance individually, with no binning at Level 1. This leads to the reduced requirement that

$$\sum_{k=1}^{K} w_m t_k^r = t_m^r \quad \text{for} \quad r = 0..R. \tag{E.8}$$

In the derivations which follow we continue to derive the expressions for both the case of calibrating each Limb radiance individually (the baseline), and the case of calibrating multiple Limb radiances together, should the need for this ever be required at a later time. Binned radiances are typically generated during non-production analyses (e.g., for zonal mean data of species with small atmospheric signals), and it must be recognized that the noise levels estimated for the binned products will be incorrect if the covariances between adjacent limb measurements are not taken into account.

E.3   Variance and the noise spectrum

From Equation E.2 we can express the variance of the filter output, $E\{D^2\}$, where E is the expectation operator, as

$$E\{D^2\} = \sum_{mn} v_m v_n E\{S_m S_n\} + \sum_{kl} w_k w_l E\{C_k C_l\} - 2 \sum_{mk} v_m w_k E\{S_m C_k\} \tag{E.9}$$

where m and n cover the range from 1 to M, and k and l cover the range from 1 to K. The reduced expression for the case of a single Limb measurement with surrounding reference measurements is given by

$$E\{D^2\} = E\{S^2\} + \sum_{kl} w_k w_l E\{C_k C_l\} - 2 \sum_{k} w_k E\{SC_k\}. \tag{E.10}$$

For a unit amplitude input signal at frequency f the term $S_m C_k$ may be written

$$S_m C_k = \frac{1}{\tau_c \tau_l} \left(\int_{-\frac{\tau_l}{2}}^{+\frac{\tau_l}{2}} e^{2\pi i f t}\, df \int_{T-\frac{\tau_c}{2}}^{T+\frac{\tau_c}{2}} e^{2\pi i f t}\, df \right) \tag{E.11}$$

where T is the interval between the centers of the two integrations (indexed by the subscripts m and n), with similar expressions for the other covariances. For UARS MLS the low frequency post-detector noise power spectrum varied as $\frac{1}{f^\alpha}$, with α ranging from ~ 1 to ~ 2.5, with breakpoint frequencies[1] of $\sim \frac{1}{10}$ Hz and lower [11]. Similar characteristics are expected for EOS MLS. For such noise characteristics the covariance $E\{S_m C_k\}$ may thus be written

$$E\{S_m C_k\} = \frac{1}{\tau_l \tau_c} \int_0^\infty \left(1 + \left(\frac{f_c}{f} \right)^\alpha \right) \operatorname{sinc}(\pi f \tau_l) \operatorname{sinc}(\pi f \tau_c) \cos(2\pi f T_m k)\, df \tag{E.12}$$

where f_c is the breakpoint frequency of the $\frac{1}{f}$ noise and T_{mk} is the time between the centers of the two data integrations.

Following the work of Peckham [6] we convert the expressions for the covariances into dimensionless forms by means of the substitutions $f' = \frac{f}{f_c}$, $\tau_l' = 2\pi f_c \tau_l$, $\tau_c' = 2\pi f_c \tau_c$, $T_k' = 2\pi f_c T_k'$, etc. Full expressions for the covariances then become

$$
\begin{aligned}
E\{S_m S_n\} &= \frac{f_c}{\tau_l^2} \int_0^\infty (1 + f'^{-\alpha}) \operatorname{sinc}^2\left(\frac{f' \tau_l'}{2} \right) \cos(f' T_{mn}')\, df' \\
E\{C_k C_l\} &= \frac{f_c}{\tau_c^2} \int_0^\infty (1 + f'^{-\alpha}) \operatorname{sinc}^2\left(\frac{f' \tau_c'}{2} \right) \cos(f' T_{kl}')\, df' \\
E\{S_m C_k\} &= \frac{f_c}{\tau_l \tau_c} \int_0^\infty (1 + f'^{-\alpha}) \operatorname{sinc}\left(\frac{f' \tau_l'}{2} \right) \operatorname{sinc}\left(\frac{f' \tau_c'}{2} \right) \cos(f' T_{mk}')\, df'
\end{aligned}
\tag{E.13}
$$

---

[1] The breakpoint frequency, f_c, is the frequency at which the $\frac{1}{f}$ and spectrally flat noise power spectral densities are equal.

where T_{ab} is the time difference (in the appropriate units) between the centers of integrations a and b.

E.4 Minimum variance estimate

Equation E.9 may be rewritten

$$E\{D^2\} = c + \sum_{kl} A_{kl} w_k w_l - 2 \sum_k b_k w_k \tag{E.14}$$

where

$$c = \sum_{mn} v_m v_n E\{S_m S_n\}, \qquad A_{kl} = E\{C_k C_l\}$$

and

$$b_k = \sum_m v_m E\{S_m C_k\}$$

Introducing Lagrange multipliers, λ_r, the minimum of $E\{D^2\}$, subject to the constraints of Equation E.7, occurs when w_k satisfy

$$\sum_{l=1}^{K} A_{kl} w_l + \sum_{r=1}^{R+1} k^{r-1} \lambda_r = b_k \tag{E.15}$$

for $k = 1$ to K. Note that the range of r has been changed from 0 to R (in Equation E.7) to 1 to $R+1$ to conform to the usual matrix notation. These equations, together with the constraints themselves, may be summarized in matrix form as

$$\begin{pmatrix} \mathbf{A} & \mathbf{P} \\ \mathbf{P^T} & \mathbf{O} \end{pmatrix} \begin{pmatrix} \mathbf{w} \\ \lambda \end{pmatrix} = \begin{pmatrix} \mathbf{b} \\ \mathbf{q} \end{pmatrix} \tag{E.16}$$

Here, $\mathbf{A}$ is a square matrix of dimension K, $\mathbf{O}$ is the null matrix of dimension $R+1$, $P_{kr} = k^{r-1}$ and

$$q_r = \sum_{m=1}^{M} (m + \beta)^{r-1} v_m$$

The minimum variance corresponding to these values is given by

$$E\{D^2\} = c - (\mathbf{b^T q^T}) \begin{pmatrix} \mathbf{w} \\ \lambda \end{pmatrix} \tag{E.17}$$

Efficient evaluation of the integrals in Equations E.13 is described in [6]. Since we will only evaluate these expressions during off-line processing to obtain the data needed for determination of absolute radiance offsets for EOS MLS, efficiency is not paramount. As discussed in Chapter 4, for determination of the absolute radiance uncertainties we only need to evaluate the right hand term of Equation E.1. This is readily accomplished using Simpson's rule.

E.5 Notation

The symbols used in this Appendix occasionally duplicate those used with different meanings elsewhere in this document. The table below lists the first occurrence of each symbol here, together with a brief description.

Notation used in this chapter

Symbol	units	Equation	description
f	Hz	E.12	post-detector signal frequency
f_c	Hz	E.12	breakpoint frequency of post-detector $\frac{1}{f}$ noise component
i		E.4	'order' index
i		E.11	the square root of minus one
k		E.2	target measurement index
m		E.2	reference measurement index
$\mathbf{q}$		E.16	vector – see text
t	s	E.12	time
t^i	s	E.4	time raised to the power i
v_m		E.2	sample weighting applied to Space reference measurement m
w_m		E.2	sample weighting applied to Target reference measurement m
$\mathbf{A}$		E.16	covariance matrix
C_k	Counts	E.11	Target counts at time index k
D_T	Counts	E.2	Smoothed time sequence of signal minus reference counts
E	Counts^2	E.9	variance of output interpolate
K		E.2	total number of Target reference measurements used in an interpolation
M		E.2	total number of Space reference measurements used in an interpolation
$\mathbf{O}$		E.16	null matrix
$\mathbf{P}$		E.16	matrix – see text
R		E.4	order of interpolating polynomial
S	Counts	E.4	a sequence of reference measurements
S_m	Counts	E.11	Space counts at time index m
T	s	E.2	the time onto which the interpolate is being determined
α		E.12	slope of $\frac{1}{f}$ component of noise power spectrum
λ_r		E.15	vector of Lagrange multipliers
τ_c	s	E.11	integration time of each target reference measurement
τ_l	s	E.11	integration time of each limb measurement
$\tau'\ T'$		E.13	time multiplied by $2\pi f_c$

Appendix F

Integrator and detector noise relationships

In this appendix we discuss the noise bandwidth of an integrator and the noise characteristics at the output of a square law detector. The assumptions that are conventionally made in the derivation of the standard results are also elaborated.

F.1 Noise bandwidth of an integrator

The noise bandwidth, f_n, of an electronic filter with frequency response in the voltage domain of $A_v(f)$ is given by

$$f_n = \frac{1}{A_v(f_0)A_v^*(f_0)} \int_0^\infty A_v(f)A_v^*(f)\,df \tag{F.1}$$

where $A_v(f_0)$ is the maximum gain of the filter (at frequency f_0). This noise bandwidth is the equivalent bandwidth of a hypothetical filter (i.e., a rectangular one with infinitely sharp cutoffs) which passes the same noise power as the 'real' filter represented by A_v. For integrators such as those used in MLS as the post-detector filter-digitizers we have the situation that the voltage gain of the filter is a maximum at zero frequency, and is directly proportional to the integration time. Consider the basic integrator circuit shown in Figure F.1. For an
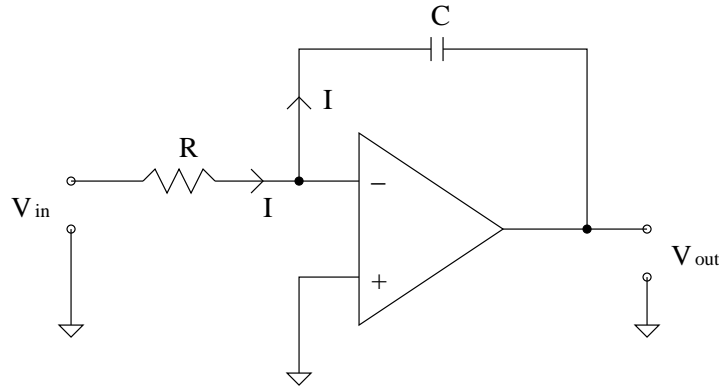

Figure F.1: Schematic of an electronic integrator.

91

integrator in which RC $= 1$ we may define the voltage gain (which is obtained with a DC input signal) as unity per unit integration time. Using the expression for integrator response derived in Appendix C, the noise bandwidth is then given by

$$f_n = \int_0^\infty \frac{\sin^2(\pi f \tau)}{(\pi f \tau)^2} \, df = \frac{1}{2\tau} \tag{F.2}$$

where integral is evaluated directly using the relationship

$$\int_0^\infty \frac{\sin^2(px)}{x^2} \, dx = \frac{\pi p}{2} \tag{F.3}$$

which may be obtained from any reasonable mathematical handbook with tabulations of integrals.

An alternative method of deriving this result is by use of Parseval's theorem which formalizes the equivalence of power expressed in the frequency and time domains:

$$w_n = \int_0^\infty |H(jw)|^2 \, dw = \pi \int_0^\infty h^2(t) \, dt = \pi E \tag{F.4}$$

An input signal consisting of a unit impulse ($1\,\text{V}$ for $1\,\text{s}$) compressed to an infinitesimally small time leads to an output voltage $\frac{-1}{RC}$ for the integrator shown in Figure F.1. If a $1\,\Omega$ resistor is presented as a load at the output of the integrator, the energy dissipated in this load is $\frac{1}{(RC)^2}\,\text{W}$. Normalizing by the power gain of the integrator, $\frac{\tau}{(RC)^2}$, gives

$$E = \left(\frac{RC}{\tau}\right)^2 \times \frac{\tau}{(RC)^2} = \frac{1}{\tau}$$

Thus

$$w_n = 2\pi f_n = \frac{\pi}{\tau}$$

or

$$f_n = \frac{1}{2\tau}$$

as before.

F.2   The detection process

The following sections are based on prior work by Robinson [8]. Most practical detectors fall into one of two categories: square law or linear detectors, characterized by the law relating their output current to their input voltage. For a square law detector we have:

$$I = \alpha V^2, \tag{F.5}$$

and for a linear detector:

$$\begin{aligned} I &= \alpha V, & V \geq 0 \\ I &= 0, & V < 0 \end{aligned} \tag{F.6}$$

At sufficiently low input levels, all detectors exhibit square law characteristics, and at high enough input levels, all behave approximately like linear detectors. The tunnel diode detectors used in EOS MLS filter channels are chosen to exhibit close to ideal square law behavior over the full range of input signals, and we shall concentrate on detectors with this characteristic below.

A typical system involving a detector is shown in Figure F.2. The input signal consists of $V(t)$ containing both noise and signals[1] in a band of width B centered at B_0, and the output of interest is at low frequencies from DC to B. The bandwidth B need not be well defined, but we require that the signal power be negligible at frequencies outside the limits, say $B_0 \pm 2B$, and that B is less than approximately $B_0/4$ (which is true for all MLS filter channels). The low frequency output from the detector contains components from DC to B arising from difference beats between input components. There are also sum components near $2B$ which are rejected by MLS post detector electronics, which we shall neglect.

The properties of the low frequency output are discussed most conveniently in terms of the envelope of the input. Let the input be expanded as a Fourier series in an interval T so that, adopting units of time $t = T/2\pi$, we have

$$V(t) = \sum_{n=0}^{\infty} a_n \cos(nt + \phi_n), \tag{F.7}$$

for which only those coefficients a_n for which

$$B_0 - \frac{B}{2} < \frac{n}{T} < B_0 + \frac{B}{2} \tag{F.8}$$

have values appreciably different from zero. We may manipulate the previous expressions to obtain

$$V(t) = A\cos(n_0 t) - B\sin(n_0 t) \tag{F.9}$$

where

$$\begin{aligned}
A &= \sum a_n \cos((n - n_0)t + \phi_n), \tag{F.10} \\
B &= \sum a_n \sin((n - n_0)t + \phi_n),
\end{aligned}$$

and

$$n_0 = B_0 T \tag{F.11}$$

---

[1]For systems such as MLS measuring thermal emission, the input signal ideally comprises just thermal noise.
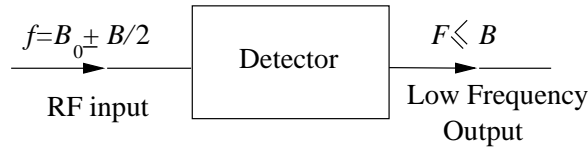
Figure F.2: Basic detector configuration. F is used to denote post detector frequencies, and f RF input signal frequencies.

corresponds to the center frequency of the RF input signal band.

We can then write $V(t)$ as

$$V(t) = R(t)\cos(n_0 t + \theta), \tag{F.12}$$

where

$$R(t) = \sqrt{(A^2 + B^2)} \tag{F.13}$$

and

$$\tan(\theta) = A/B. \tag{F.14}$$

Since n ranges only over the limited interval $(B_0 \pm B/2)T$, no component of A or B varies more rapidly with t than $B/2$, and no component of $R(t)$ more rapidly than B. Thus $R(t)$ is a slowly varying function of t compared with $\cos(n_0 t)$, and is the envelope of $V(t)$ shown in Figure F.3.
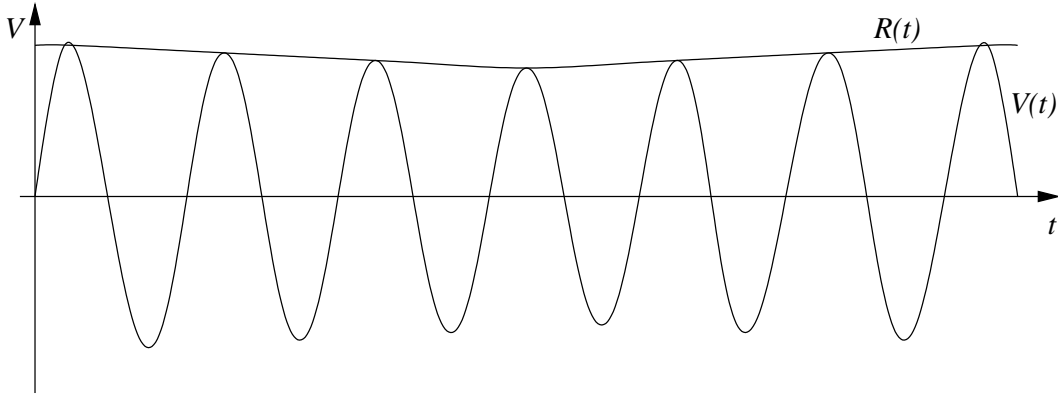
Figure F.3: The envelope $R(t)$ of an amplitude modulated signal $V(t)$.

F.3 Noise characteristics of a square law detector

A signal $V_0 \cos(n_0 t)$ applied to a square law detector results in an output current I where

$$I = \alpha V_0^2 \cos^2(n_0 t) = \frac{1}{2}\alpha V_0^2 (1 - \cos(2n_0 t)) \tag{F.15}$$

and α is a constant representing the 'efficiency' of the detector. We are normally just concerned with the DC term in this expression:

$$I_{dc} = \frac{\alpha}{2}V_0^2. \tag{F.16}$$

If we apply an input signal $R(t)\cos(n_0 t + \theta)$, the low frequency output of the square law detector is clearly given by

$$I_{lf} = \frac{\alpha}{2}R^2(t) \tag{F.17}$$

We may rewrite this equation as

$$I_{lf} = \frac{\alpha}{2}(A^2 + B^2) = \frac{\alpha}{2}\sum_n\sum_m a_n a_m \cos((n-m)t + \phi_n - \phi_m), \tag{F.18}$$

or in the form of a Fourier series

$$I_{lf} = \sum_k C_k \cos(kt + \phi_k). \tag{F.19}$$

recognizing that terms of frequency k arise only when $m = n \pm k$. In particular, the DC term is

$$I_{dc} = C_0 = \frac{\alpha}{2}\sum_n a_n^2. \tag{F.20}$$

If the input is a noise process with a power spectrum $w(f)$ over a predetection bandwidth B centered at $F = 0$ we have

$$\sum\langle a_n^2\rangle = 2\int_{f_0-B/2}^{f_0+B/2} w(f)\,df, \tag{F.21}$$

and so

$$I_{dc} = C_0 = \alpha\int_{f_0-B/2}^{f_0+B/2} w(f)\,df. \tag{F.22}$$

The term of frequency k is given by

$$C_k \cos(kt + \theta_k) = \frac{\alpha}{2}\left(\sum_n a_n a_{n-k}\cos(kt + \phi_n - \phi_{n-k}) + \sum_n a_n a_{n+k}\cos(kt + \phi_{n+k} - \phi_n)\right). \tag{F.23}$$

The two terms in this expression yield identical results, for they differ only for terms with $n < k$, i.e., $f < B$, where the input is in any case zero. We therefore have

$$C_k \cos(kt + \theta_k) = \alpha\sum_n a_n a_{n+k}\cos(kt + \phi_{n+k} - \phi_n). \tag{F.24}$$

The phases ϕ_{n+k} and ϕ_n are independently and randomly distributed, and so the ensemble average of this expression is zero. Thus

$$\langle C_k\rangle = 0, \quad k \neq 0. \tag{F.25}$$

If we square Equation F.24 we have

$$C_k^2 \cos^2(kt + \theta_k) = \alpha^2\sum_n\sum_m a_n a_m a_{n+k}a_{m+k}\cos(kt + \phi_{n+k} - \phi_n)\cos(kt + \phi_{m+k} - \phi_m). \tag{F.26}$$

In an ensemble average the cross-terms with $m \neq n$ drop out, again because of the independence of the phases, and we are left with

$$\langle C_k^2\rangle = \alpha^2\sum_n\langle a_n^2 a_{n+k}^2\rangle. \tag{F.27}$$

Since the a_n and a_{n+k} $(k \neq 0)$ are independent, this is equivalent to

$$\langle C_k^2\rangle = \alpha^2\sum_n\langle a_n^2\rangle\langle a_{n+k}^2\rangle. \tag{F.28}$$

We now express $\langle C_k^2 \rangle$ in terms of a power spectrum $W(F)$, where $F = k/T$, giving

$$
\begin{aligned}
\langle C_k^2 \rangle &= (\text{limit } T \to \infty)\ 2W(F)/T, & \text{(F.29)} \\
\langle a_n^2 \rangle &= (\text{limit } T \to \infty)\ 2w(f)/T.
\end{aligned}
$$

Sums over n then become T times integrals over f, i.e.,

$$
\sum_n \to T \int df, \tag{F.30}
$$

so that

$$
W(F) = 2\alpha^2 \int_{f_0 - \Delta f_0/2}^{f_0 + \Delta f_0/2} w(f)w(f + F)\, df. \tag{F.31}
$$

We thus have now expressed the output spectrum in terms of input spectrum.

F.3.1 White noise input to a square law detector

It is normally an implicit assumption the that RF signal into a spectrometer power detector consists of white noise with constant power spectral density w within a well defined bandpass B, giving

$$
I_{dc} = \alpha w B \tag{F.32}
$$

and the power spectrum

$$
W(F) = 2\alpha^2 w^2 B \left(1 - \frac{F}{B} \right). \tag{F.33}
$$

The noise spectrum is thus seen to have its maximum intensity near DC, falling to zero at B.

The total low-frequency output noise is obtained from Equation F.33 by integrating from DC to $F \geq B$, and is given by

$$
\Delta I^2 = \alpha^2 w^2 B. \tag{F.34}
$$

If the bandwidth Δf of the measurement system is very much less than B, a measurement of the DC current can be made to a resolution of $I_{dc} \pm (w\Delta F)^{\frac{1}{2}}$. The signal to noise of the measurement is therefore $(2\Delta F/B)^{\frac{1}{2}}$. In terms of system temperature and ΔT we have:

$$
\frac{\Delta T}{T_{\text{sys}}} = \left(\frac{2\Delta F}{B} \right)^{\frac{1}{2}}. \tag{F.35}
$$

We showed earlier in this appendix that the noise bandwidth of an integrator is given by the reciprocal of twice the integration time τ, i.e.,

$$
\Delta F = \frac{1}{2\tau} \tag{F.36}
$$

leading to the more familiar expression

$$
\frac{\Delta T}{T_{\text{sys}}} = \sqrt{\frac{1}{B\tau}}. \tag{F.37}
$$

F.3.2 White noise with a continuous wave (CW) signal

A situation likely to arise in several filter spectrometer channels on EOS MLS is that the atmospheric and electronic noise signal input to the power detector will be contaminated by an unmodulated continuous wave signal S via leakage from local oscillators used for 2nd and 3rd IF downconversion. These contaminating signals will be very stable in both frequency and amplitude. Proceeding as before, the resulting expression for the DC term at the output of the detector for a contaminating signal $S\cos(2\pi f t_0)$ at the center of the predetection passband may be shown to be

$$I_{dc} = \frac{\alpha}{2}(S^2 + 2wB), \tag{F.38}$$

meaning that the signal and noise are detected independently.

The power spectrum is rather less simple than before since noise between DC and $F = B$ can arise either from beats between noise components or between noise and the CW signal, whereas noise between $B/2$ and B arises solely from noise beats alone. This results in

$$W(F) \;=\; 2\alpha^2 w\left(S^2 + wB\left(1 - \frac{F}{B}\right)\right) \quad \text{where } 0 < F < \frac{B}{2} \tag{F.39}$$

$$W(F) \;=\; 2\alpha^2 w^2 B\left(1 - \frac{F}{B}\right) \quad \text{where } \frac{B}{2} < F < B$$

This spectrum is illustrated in Figure F.4. The total low frequency noise obtained by integrating Equations F.39 from DC to $F \geq B$ is

$$\Delta I^2 = \alpha^2 wB(S^2 + wB). \tag{F.40}$$

The presence of a steady signal within the predetection passband which significantly contributes to the detector DC output is thus seen to also increase the noise output power.
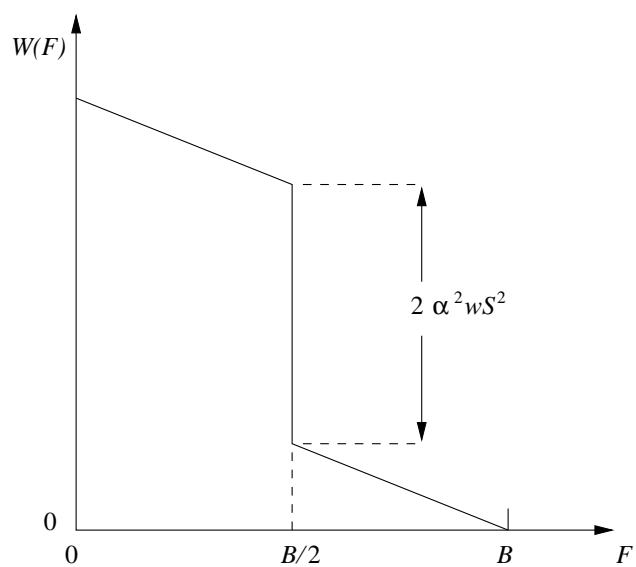
Figure F.4: Power spectrum, $W(F)$, of the low frequency output of a square law detector with white noise input in bandwidth B and a signal S at the center of the passband.

Appendix G

Digital Autocorrelator Spectrometers

Digital autocorrelators (DACS) similar to the ones implemented in EOS MLS have been used elsewhere, and their implementation and theory of operation is described in the literature (e.g., [9] and [10]). For EOS MLS they provide relatively narrow bandwidth ($\sim$10 MHz) and high resolution (120 kHz FWHM with no apodization) spectrometers with uniform 98 kHz channel spacing. Due to their largely digital implementation, DACS tend to be compact, easy to fabricate, and have uniform channel-to-channel characteristics, when compared to analog filterbank spectrometers.

The signal flow through an EOS MLS DACS is illustrated in Figure G.1. The signal band of interest is down-converted from $905-892.5$ MHz in the center of a 25-Channel Filterbank to baseband, $0-12.5$ MHz, and then bandpass filtered to $\sim 0.1-10$ MHz. This signal is coarsely digitized to 2 bits on each cycle of a 25 MHz clock and fed into a CMOS autocorrelator ASIC (application specific integrated circuit.) The ASIC has a pair of 129-element shift registers, one with a single-clock-cycle delay between lags and the other with a two-clock-cycle delay between lags. Each clock cycle, corresponding elements in the two shift registers are multiplied and accumulated so that the first counter sums products of two undelayed inputs and the last counter sums products in which the element in the doubly-delayed shift register is 128 clock cycles older than the element in the singly-delayed shift register. Apart from start-up transients, this is equivalent to multiplying an undelayed input with all of the elements of a singly-delayed shift register, but is easier to implement.

The output of each multiplier is added to a 4-bit, fast accumulator, with the carry being fed to a slower, 24-bit counter. The accumulator effectively performs as a divide by 16 (i.e., 4 bits of equivalent prescale). The digitizer, shift registers, multipliers and prescalar are synchronous with an extermal, 25-MHz clock while the 24-bit counters are implemented as ripple counters to minimize logic area and power consumption. Additional data buffers (not shown in the figure) are implemented to allow the 24-bit counter array contents to be saved, and the counters themselves cleared, to start the next data integration before the data readout is complete. A control input allows the data accumulation to be suspended so that the asynchronous counters can settle prior to being loaded into the readout registers and cleared. The data path out of the DACS ASIC is one byte wide, and the output register auto-increments each time it is read.

The DACS restart their integrations very early in the 5 ms blanking pulse between MIFs
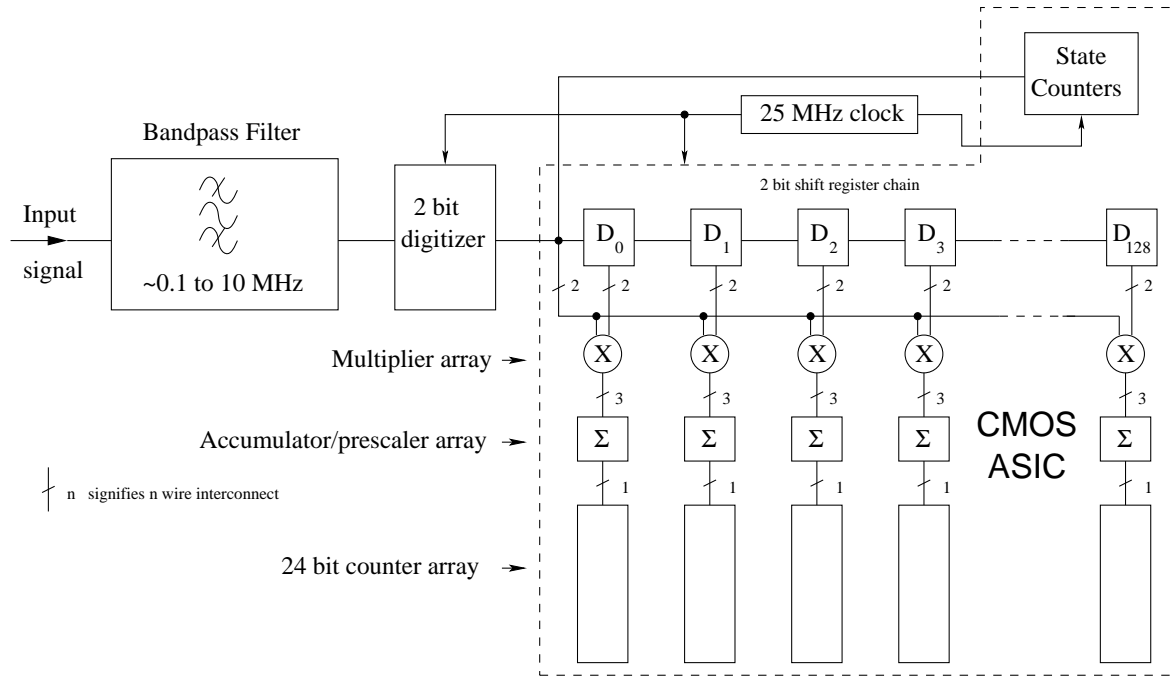
Figure G.1: Simplified schematic of the 2-bit DACS used on EOS MLS. The portion enclosed in the dashed box is fabricated on a single CMOS chip, and includes control logic for enabling/disabling and clearing the counter array, and a byte serial readout interface to read the 24-bit counter array into an accompanying RIU. The state counters record the total number of occurrences of each of the four possible digitizer output states during each data integration, and are used to determine total input RF signal power.

(also called the real-time interrupt or RTI) so there is a small difference between the DACS integration window and that of the filterbank channels. The extra 5 ms at the beginning of each 1/6-second integration causes the MIF-averaged DACS integration time to be shifted forward by 1.5% of the MIF spacing. This results in a pointing bias as large as 30 m in the mesosphere, where the nominal scan is fastest. If such a bias is found to have a significant impact on retrievals, a first-order correction may be easily implemented in the forward model. Calculated radiances can be replaced by 1.5% of the radiance from the previous MIF and 98.5% of the current MIF for all limb-viewing MIFs except the first (where the previous MIF's average may not be appropriate, but the scan is slowest.)

G.1   Digitizer and multiplier operation

We start the description of the 2-bit autocorrelator by discussing a 'conventional' implementation, followed by minor modifications used in the EOS MLS DACS which result in a simplified unit with similar performance characteristics. The 2-bit digitizer has 4 output states ($\overline{2}$, $\overline{1}$, 1, 2) which are assigned values of $-n$, -1, $+1$ and $+n$ respectively. When two voltages digitized as shown in Table G.1 are multiplied, the products shown in Table G.2 are generated.

Consider a particular "lag" in the autocorellator which has, as input, a series of voltage

Table G.1: The 2-bit quantization scheme implemented in an 'ideal' 2-bit digital autocorrelator. The digitizer thresholds are set at voltages of $-V_0$, 0 and $+V_0$.

Input Voltage Range:	$-\infty < v \leq -V_0$	$-V_0 < v \leq 0$	$0 < v \leq V_0$	$V_0 < v \leq \infty$
Sign bit	1	1	0	0
Magnitude bit	1	0	0	1
State designation	$\bar{2}$	$\bar{1}$	1	2
Weighting factor	$-n$	-1	$+1$	$+n$

pairs sampled with the same fixed time offset relative to one another. Let P_{11}, $P_{1\bar{1}}$, ..., $P_{\bar{2}\bar{2}}$ be the probabilities of finding the two noise voltages jointly in the states designated by the associated P subscripts, and T be the number of samples summed in the accumulators during an integration. The expected value of counts in an add-subtract counter at the multiplier output is the weighted sum over Table G.2.

$$\langle N_{2\text{bit}} \rangle = n^2(\langle N_{22} \rangle - \langle N_{2\bar{2}} \rangle) + n(\langle N_{12} \rangle - \langle N_{1\bar{2}} \rangle) + \langle N_{11} \rangle - \langle N_{1\bar{1}} \rangle \tag{G.1}$$

where

$$\langle N_{11} \rangle = 2P_{11}T, \qquad \langle N_{1\bar{1}} \rangle = 2P_{1\bar{1}}T, \qquad \langle N_{12} \rangle = 4P_{12}T,$$
$$\langle N_{1\bar{2}} \rangle = 4P_{1\bar{2}}T, \qquad \langle N_{22} \rangle = 2P_{22}T, \qquad \langle N_{2\bar{2}} \rangle = 2P_{2\bar{2}}T.$$

Here we have assumed that the two samples being multiplied (the two subscripts of P_{ij}) are of a zero-mean, symmetric, stationary process, and that the digitizer thresholds are symmetrically place at $\pm V_0$ and zero, permitting us to equate probabilities $P_{ab} = P_{\bar{a}\bar{b}}$, $P_{\bar{a}b} = P_{a\bar{b}}$ and $P_{ab} = P_{ba}$.

Maximum count rate occurs with two fully correlated voltages ($\rho = 1$), under which condition the only nonzero probabilities are P_{11} and P_{22}. Hence a two-bit correlation coefficient, $\rho_{2\text{bit}}$, can be defined

$$
\begin{aligned}
\rho_{2\text{bit}} &= \frac{\langle N_{2\text{bit}} \rangle}{N_{\max}} \\
&= \frac{(P_{22} - P_{2\bar{2}})n^2 + 2(P_{12} - P_{1\bar{2}})n + (P_{11} - P_{1\bar{1}})}{(P_{22}n^2 + P_{11})_{\rho=1}}.
\end{aligned}
\tag{G.2}
$$

Table G.2: Two bit multiplication table for the quantization scheme of Table G.1. Table entries are the outputs of each DACS multiplier for all possible combinations of delayed (v_1) and undelayed (v_2) digitized signals.

v_2 state	v_1 state			
	$\bar{2}$	$\bar{1}$	1	2
2	$-n^2$	$-n$	$+n$	$+n^2$
1	$-n$	-1	$+1$	$+n$
$\bar{1}$	$+n$	$+1$	-1	$-n$
$\bar{2}$	$+n^2$	$+n$	$-n$	$-n^2$

Now, assume that the two input voltages are a pair of unit variance, jointly Gaussian random variables with probability ditribution parameterized by ρ:

$$F(\rho, v_1, v_2) = \frac{1}{2\pi\sqrt{1-\rho^2}} \exp\left(\frac{-v_1^2 + 2\rho v_1 v_2 - v_2^2}{2(1-\rho^2)}\right). \tag{G.3}$$

Integrals of probabilities appearing in Equation G.2 are

$$P_{11} = \int_0^{V_0} \int_0^{V_0} F\, dv_1\, dv_2$$

$$P_{1\bar{1}} = \int_0^{V_0} \int_{-V_0}^0 F\, dv_1\, dv_2$$

$$P_{12} = \int_0^{V_0} \int_{V_0}^\infty F\, dv_1\, dv_2$$

$$P_{1\bar{2}} = \int_0^{V_0} \int_{-\infty}^{-v_0} F\, dv_1\, dv_2$$

$$P_{22} = \int_{V_0}^\infty \int_{V_0}^\infty F\, dv_1\, dv_2$$

$$P_{2\bar{2}} = \int_{V_0}^\infty \int_{-\infty}^{-V_0} F\, dv_1\, dv_2 \tag{G.4}$$

For $\rho \ll 1$, we can expand the exponential in F to first order in ρ.

$$P_{11} = \frac{1}{4}\phi^2 + \frac{\rho}{2\pi}(1-E)^2 \;,$$

$$P_{1\bar{1}} = \frac{1}{4}\phi^2 - \frac{\rho}{2\pi}(1-E)^2 \;,$$

$$P_{12} = \frac{1}{4}\phi(1-\phi) + \frac{\rho}{2\pi}E(1-E) \;,$$

$$P_{1\bar{2}} = \frac{1}{4}\phi(1-\phi) - \frac{\rho}{2\pi}E(1-E) \;,$$

$$P_{22} = \frac{1}{4}(1-\phi)^2 + \frac{\rho}{2\pi}E^2 \;,$$

$$P_{2\bar{2}} = \frac{1}{4}(1-\phi)^2 - \frac{\rho}{2\pi}E^2 \;. \tag{G.5}$$

where

$$E = \exp(-\frac{1}{2}v_0^2),$$

and

$$\phi(v_0) = (2\pi)^{-\frac{1}{2}} \int_{-v_0}^{v_0} \exp(-\frac{1}{2}v^2)dv \;. \tag{G.6}$$

Probabilities appearing in the denominator of Equation G.2 are the probabilities of finding, for perfectly correlated v_1 or v_2, either v_1 (and v_2) in the range 0 to v_0 or v_0 to ∞, that is,

$$P_{11} = \tfrac{1}{2}\phi(v_0), \qquad P_{22} = \tfrac{1}{2}(1 - \phi(v_0)), \qquad \text{for} \quad \rho = 1 \ .$$

Substituting these results in Equation G.2 leads to

$$\frac{\rho_{2\mathrm{bit}}}{\rho} = \frac{2}{\pi}\left(\frac{(1 - 2n^{-1} + n^{-2})E^2 + 2(n^{-1} - n^{-2})E + n^{-2}}{1 - \phi + \phi n^{-2}}\right) \quad \text{for} \quad \rho \ll 1 \qquad (\mathrm{G.7})$$

The signal to noise of the two-bit correlator, R_2, is given by

$$\begin{aligned} R_2 &= \langle N_{2\mathrm{bit}}\rangle(\langle N_{2\mathrm{bit}}^2\rangle - \langle N_{2\mathrm{bit}}\rangle^2) \\ &= (N_{2\mathrm{bit}}/N_{max})N^{\frac{1}{2}} \\ &= \rho_{2\mathrm{bit}}N^{\frac{1}{2}}, \quad \rho_{2\mathrm{bit}} \ll 1 \end{aligned} \qquad (\mathrm{G.8})$$

If the same number of samples were multiplied in a continuous correlator and averaged, the signal to noise ratio R_c would be given by

$$R_c = \rho N^{\frac{1}{2}} \qquad (\mathrm{G.9})$$

and hence

$$R_2/R_c = \rho_{2\mathrm{bit}}/\rho, \quad \rho \ll 1 \qquad (\mathrm{G.10})$$

Thus the sensitivity of the two-bit correlator relative to a continuous correlator is also given by the right hand side of Equation G.7. The maximum value of R_2/R_c is 0.88 for $n = 3$ and $v_0 = 1.0$.

G.2 The modified two-bit autocorrelator

If the products in Table G.2 which have values ± 1 are set to zero, a significant simplification in implementation may be realized for a small cost in noise performance. The signal-to-noise ratio of such a modified correlator, R_{2a}, may be expressed

$$\frac{R_{2a}}{R_c} = \frac{2}{\pi}\frac{E^2 + 2E(1 - E)n^{-1}}{((1 - \phi)^2 + 2\phi(1 - \phi)n^{-2})}, \qquad \rho \ll 1 \ . \qquad (\mathrm{G.11})$$

The ratio R_{2a}/R_c has a maximum of 0.87 for $n = 3$ and $V_0 = 0.9$ for a band-limited, Nyquist-sampled input signal. The 2-bit digitization of the input signal may be regarded as the addition of a noise signal which is the difference between the digitized and analog versions of the input. Although the analog input may be band-limited, the noise introduced by digitization will not be, so oversampling of the input can provide additional information. Oversampling of the input by a factor of two increases the signal-to-noise of the modified 2-bit autocorrelator to 0.933 of the continuous autocorrelator. [10] The MLS DACS have an input bandwidth of approximately 10 MHz and are sampled at 25 MHz (12.5 MHz Nyquist rate) so they are oversampled by a factor of 25 percent. Their signal to noise will be something between these two values.

G.3 The EOS MLS implementation

The multiplication table for the modified 2-bit correlator is shown on the left-hand side of Table G.3. The multiplication table implemented in the DACS hardware, shown on the right-hand side of Table G.3. It has $n = 3$ and is divided by 3 and shifted by three so that counter bits are minimized and up-down counters are not needed. The divide-by-3 has no impact on the information content and $3T$ can be subtracted before post-processing to remove the effect of the shift-by-3.

G.4 Estimate of true autocorrelation

Before the measured autocorrelation can be Fourier transformed into the frequency domain it is necessary to converted the measurements into an estimate of the continuous autocorrelation of the input signal. For the system described, the continuous autocorrelation, R_c, may be approximated from the the measured two-bit one, R_{2a}, using

$$
\begin{aligned}
R_c &= 1.146 R_{2a} - 0.049 R_{2a}^2 \quad \text{for } 0.0 \leq R_{2a} < 0.9 \\
&= 1.340 R_{2a} - 0.340 R_{2a}^2 \quad \text{for } 0.9 \leq R_{2a} \leq 1.0.
\end{aligned}
\tag{G.12}
$$

These expressions have been derived from fits to Equation G.11. These equations assume that the signal is small compared the system temperature contribution to the signal input power to the digitizers. They apply to an ideal digitizer with thresholds at -0.9σ, 0σ, and 0.9σ.

In practice, thresholds will not be perfectly set with the positive and negative thresholds at $\pm 0.9\sigma$, and the zero-crossing threshold at the exact center of the distribution. Furthermore, they may not be perfectly stable with input level, due to digitizer imperfections. A set of four "state counters" is included in the DACS to record the number of instances of each of the four digitizer states in an integration. These counters can be used to estimate the position of the three digitizer thresholds in units of input sigma (t_N, t_Z, t_P), as discussed in Section H.3.2, and these values can be used to correct the estimate of the continuous autocorrelation.

A bivariate-Gaussian probability distribution may be integrated over the correlator multiplication table, as is shown in Figure G.4. For a range of thresholds ($t_N \to N$, $t_P \to P$, $t_Z \to Z$ in the figure), and for a range of correlations ρ, the modified 2-bit autocorrelation

		v_1							v_1			
		$\bar{2}$	$\bar{1}$	1	2				$\bar{2}$	$\bar{1}$	1	2
	2	$-n^2$	$-n$	$+n$	$+n^2$			2	0	2	4	6
v_2	1	$-n$	0	0	$+n$	$\Longrightarrow$	v_2	1	2	3	3	4
	$\bar{1}$	$+n$	0	0	$-n$			$\bar{1}$	4	3	3	2
	$\bar{2}$	$+n^2$	$+n$	$-n$	$-n^2$			$\bar{2}$	6	4	2	0

Table G.3: Modified two-bit multiplication table. On the left, low-magnitude entries to Table G.2 have been set to zero. On the right is the MLS multiplication table for $n = 3$, with outputs divided by 3 and zero shifted.
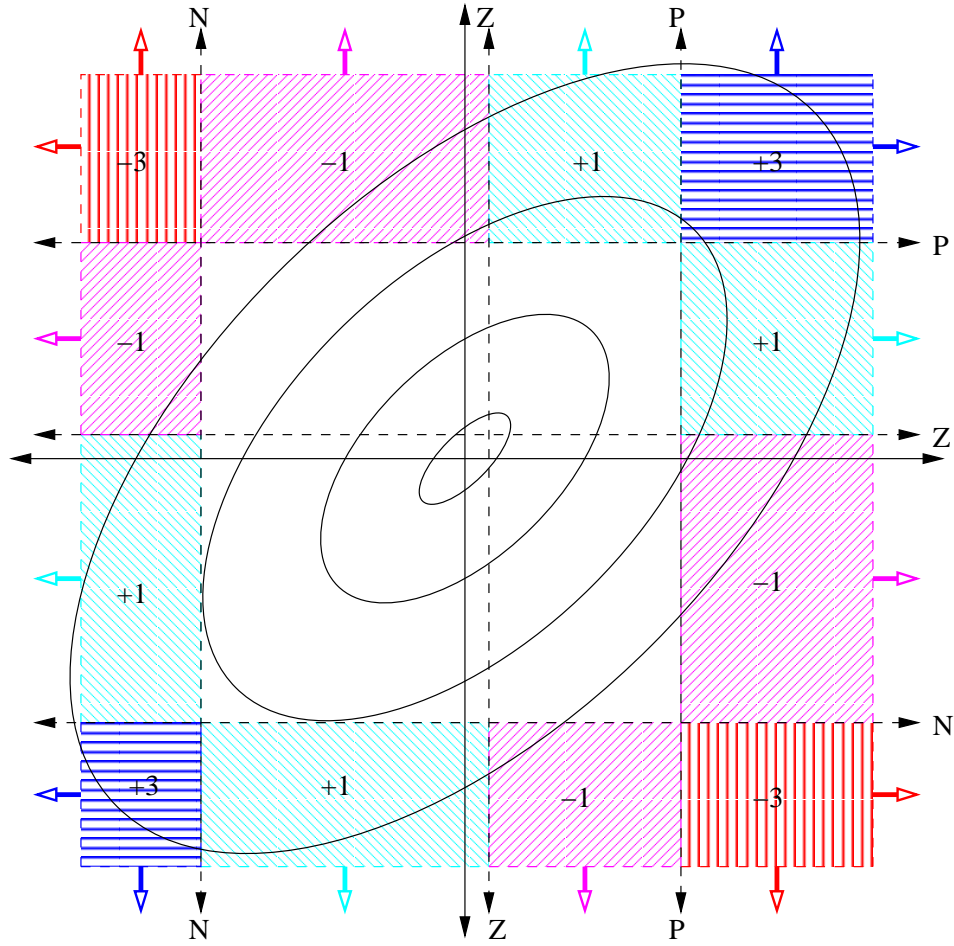
Figure G.2: The modified-two-bit autocorrelator. The contours which are shown are an example of a jointly-Gaussian distribution with positive correlation.

ρ_{2a} may be evaluated:

$$
\begin{aligned}
\rho_{2a}(t_N, t_Z, t_P; \rho) =\ & +3 \int_{t_P}^{\infty} \int_{t_P}^{\infty} F(\rho; x, y)\, dx\, dy + 3 \int_{-\infty}^{t_N} \int_{-\infty}^{t_N} F(\rho; x, y)\, dx\, dy \\
& -3 \int_{t_P}^{\infty} \int_{-\infty}^{t_N} F(\rho; x, y)\, dx\, dy - 3 \int_{-\infty}^{t_N} \int_{t_P}^{\infty} F(\rho; x, y)\, dx\, dy \\
& + \int_{t_Z}^{t_P} \int_{t_P}^{\infty} F(\rho; x, y)\, dx\, dy + \int_{t_P}^{\infty} \int_{t_Z}^{t_P} F(\rho; x, y)\, dx\, dy \\
& - \int_{t_N}^{t_Z} \int_{t_P}^{\infty} F(\rho; x, y)\, dx\, dy - \int_{t_P}^{\infty} \int_{t_N}^{t_Z} F(\rho; x, y)\, dx\, dy \\
& - \int_{t_Z}^{t_P} \int_{-\infty}^{t_N} F(\rho; x, y)\, dx\, dy - \int_{-\infty}^{t_N} \int_{t_Z}^{t_P} F(\rho; x, y)\, dx\, dy \\
& + \int_{t_N}^{t_Z} \int_{-\infty}^{t_N} F(\rho; x, y)\, dx\, dy + \int_{-\infty}^{t_N} \int_{t_N}^{t_Z} F(\rho; x, y)\, dx\, dy \qquad \text{(G.13)}
\end{aligned}
$$

where:

$$F(\rho; x, y) = \frac{1}{2\pi\sigma^2\sqrt{1-\rho^2}} \exp\left(\frac{-(x^2 - 2\rho xy + y^2)}{2\sigma^2(1-\rho^2)}\right)$$

This expression may be simplified by exploiting the symmetries of the bi-variate gaussian distribution and those of the multiplication table. It is the inverse of the above function, $\rho(t_P, t_N, t_Z; \rho_{2a})$, which will provide the estimate of the true autocorrelation given the DACS measurements.

The function $\rho_{2a}(t_P, t_N, t_Z; \rho)$ was evaluated on a grid of values of t_Z, $\alpha \equiv t_P + t_N)/2 - 0.9$ and $\beta \equiv t_P - t_n$ from 0σ to 5σ with spacing of 0.1σ and steps of 0.01 in ρ. This function was inverted by spline interpolating to an evenly spaced grid of ρ_{2a}. A single function was found which adequately covers the ranges of t_N, t_P, t_Z and ρ_{2a} which we expect to encounter in the MLS DACS data (excluding the zero lag.) Values of this fit are given in Section H.4.

G.5   Gain calibration

An analog power measurement channel (with data integrations synchronous with all other filter channel and DACS measurements) is implemented to provide a measure of the total average RF signal power being analyzed during each MIF as described in Chapter 4. In Appendix H we describe the use of the counters implemented in the DACS to monitor the 2-bit A/D converter thresholds and measure input signal power.

G.6   Transformation to the frequency domain

The power spectrum, $P(f)$, of the DACS input signal is calculated by performing a discrete Fourier transform on the estimate of the continuous autocorrelation function, obtained from the measured 2-bit measurement of the autocorrelation function as discussed above. The M channels (corresponding the $M = 128$ delay values in the shift register) are transformed into M points in the frequency domain via the relationship:

$$P(\frac{j}{2M\Delta t}) = \frac{1}{M}\left[R(0) + 2\sum_{m=0}^{M} R(m\Delta t) \times \cos(\pi m j/M)\right] \tag{G.14}$$

where
$P(\frac{j}{2M\Delta t})$ is the signal power at DACS input frequency $\frac{j}{2M\Delta t}$
$R(0)$ is the correlation coefficient of the zero delay channel (after normalization), and
$R(m\Delta t)$ is the normalized autocorrelation for delay $m\Delta t$.

G.7   Notation

In this Appendix, symbols which are conventional in the literature of autocorrelation spectrometers have been used for most quantities. In some cases, the same symbols have been used to signify different quantities elsewhere in this document (e.g., ρ is used here to signify correlation coefficient, and in Chapter 4 to signify reflector reflectivity). Table G.4 below lists the symbols used in this Appendix and gives their meanings.

Table G.4: Notation used in this chapter

Symbol	units	1st. occurrence	description
Δt	–	G.14	time between DACS data samples (40 ns)
$\phi(v_0)$	–	G.6	probability integral of v_0
ρ	–	G.2	correlation coefficient
$\rho_{2\text{bit}}$	–	G.2	2-bit correlation coefficient
E	–	G.5	$\exp(-\frac{1}{2}v_0^2)$
j	–	G.14	frequency index (1..128)
m	–	G.14	delay channel index (1..128)
M	–	G.14	number of delay channels (128)
n	–	Table G.2	weighting given to highest order multiplier products
N	Hz	G.1	Sampling rate (25 MHz)
$N_{2\text{bit}}$	Hz	G.1	Rate of counts accumulation for 2-bit DACS
N_{lm}	Hz	G.1	Rate of counts accumulation for state lm
P_{lm}	–	G.1	Probability of undelayed and delayed signals being in states l and m respectively
R_c	–	G.9	Signal to noise of a continuous correlator
R_2	–	G.8	Signal to noise of the 2-bit correlator
R_{2a}	–	G.11	Signal to noise of the modified 2-bit correlator
v_0	–	G.6	Normalized (*wrt* rms) non-zero digitizer thresholds
v_1, v_2	–	G.6	Normalized (*wrt* rms) signal voltages
V	V	Table G.1	Signal voltage or digitizer threshold
V_0	V	Table G.1	Modulus of non-zero digitizer thresholds
V_1, V_2	V	Table G.2	Digitized undelayed and delayed signals
$\overline{2}, \overline{1}, 1, 2$	–	Table G.1	The four possible digitized signal states

Appendix H

DACS-Specific Level 1 Processing

This appendix presents the DACS-specific Level 1 algorithms as they will be used to process EOS MLS data. It begins with a brief outline which serves to set its the notation and structure. For each DACS band, the Level 1 processing consists of the following steps:

1. Unpack science data packets (uncompressed Science Type I or normalized Science Types II, III) and construct normalized, raw lag data:

$\rho_{2a}(\tau)$	$\tau = 0 \dots 128$	Measured 2-bit autocorrelation
$N_{\bar{2}}, N_{\bar{1}}, N_1, N_2,$	(called D in CTH [13])	2-bit state counters
p	(called T in CTH)	Total power channel

2. Fix lost carry bits in state counters.

3. Calculate state counter statistics, t_P, t_N and t_Z, which are estimates of a digitizer's positive, negative and zero-crossing thresholds in units of the input gaussian noise signal's standard deviation for a given MIF.

4. Derive estimate of continuous autocorrelation from 2-bit autocorrelation and state counter statistics:

$$\rho(\tau) = \rho(t_P, t_N, t_Z; \rho_{2a}(\tau))$$

5. Scale ρ by zero-offset-corrected total power, $p - p_z$:

$$G = (p - p_z)\rho$$

6. Perform cosine transform:

$$A(j) = \mathbf{dct}(G(i))$$

7. Calibrate similarly to filterbank channels:

   - Interpolate/filter total power measurements of Space and Target to observation times.
   - Obtain averaged, normalized, blackbody spectra of Space and Target. These spectral shapes have small, systematic differences but are, individually, very stable.
   - Calibrate limb radiances including first-order effect of Space/Target shape differences.
   - Estimate uncertainties, as for filterbank channels.

Table H.1: DACS band designations.

Assembly	Hardware Band	DACS band	Filterbank Band	Receiver
2026DACS1	dacs-1 (SW1:1)	Band 25 (CO)	Band 9	R3
2026DACS1	dacs-1 (SW1:2)	Band 26 (PT)	Band 21	R1B
2026DACS1	dacs-2	Band 23 (H_2O)	Band 2	R2
2026DACS2	dacs-3	Band 24 (O_3)	Band 7	R3
2026DACS2	dacs-4	Band 22 (PT)	Band 1	R1A

H.1 Definition of Science Packets

This section pulls together, for convenience, DACS-related definitions from the EOS MLS Instrument Flight Software Command and Telemetry Handbook [13] and the EOS MLS PFM Block Diagram (EOS MLS drawing number 10190369).

There are five DACS bands at the centers of five of the 25-channel filterbank bands. They are processed in four hardware bands (one with a switchable input) on two assemblies, as shown in Table H.1.

The CTH defines six science data packets which have fields containing DACS data. Type I packets contain compressed data. Type II packets contain data only from bands dacs-1 (Packet 1) and dacs-2 (Packet 2, truncated). Type III packets contain data only from bands dacs-3 (Packet 1) and dacs-4 (Packet 2, truncated).

1. Field 'SM11 DACS 1' in Science Type I Packet 1 (Byte offset 654) contains compressed data from bands dacs-1 and dacs-2, which are on assembly 2026 DACS1 (Assembly 2026 DACS1 was formerly called SM11 DACS1).

$C_1(1) \ldots C_1(32)$	32 x 12 bits	unpack to signed int16
$C_1(33) \ldots C_1(128)$	96 x 8 bits	unpack to signed int16
$D_1(0) \ldots D_1(3)$	4 x 24 bits	unpack to unsigned int32
T_1	16 bits	unpack to unsigned int16
$C_2(1) \ldots C_2(32)$	32 x 12 bits	unpack to signed int16
$C_2(33) \ldots C_2(128)$	96 x 8 bits	unpack to signed int16
$D_2(0) \ldots D_2(3)$	4 x 24 bits	unpack to unsigned int32
T_2	16 bits	unpack to unsigned int16
DIO Counter Status	8 bits	unpack to byte
Zero Lag Status	8 bits	unpack to byte
LO lock status	8 bits	unpack to byte
Spare	8 bits	

2. Field 'SM12 DACS 2' in Science Type I Packet 2 (Byte offset 654) contains compressed data from bands dacs-3 and dacs-4, which are on assembly 2026 DACS2 (Assembly 2026 DACS2 was formerly called SM11 DACS 2).

$C_3(1)\ldots C_3(32)$	32 x 12 bits	unpack to signed int16
$C_3(33)\ldots C_3(128)$	96 x 8 bits	unpack to signed int16
$D_3(0)\ldots D_3(3)$	4 x 24 bits	unpack to unsigned int32
T_3	16 bits	unpack to unsigned int16
$C_4(1)\ldots C_4(32)$	32 x 12 bits	unpack to signed int16
$C_4(33)\ldots C_4(128)$	96 x 8 bits	unpack to signed int16
$D_4(0)\ldots D_4(3)$	4 x 24 bits	unpack to unsigned int32
T_4	16 bits	unpack to unsigned int16
DIO Counter Status	8 bits	unpack to byte
Zero Lag Status	8 bits	unpack to byte
LO lock status	8 bits	unpack to byte
Spare	8 bits	

3. Field 'SM11 DACS 1 band dacs-1' in Science Type II Packet 1 (offset 580B)
   or

4. Field 'SM12 DACS 2 band dacs-3' in Science Type III Packet 1 (offset 580B)
   These fields contain uncompressed data, including status bytes, for the first band on
   the selected assembly. All data from the other assembly is discarded in the C&DH.

$K_i(0)\ldots K_i(128)$	129 x 24 bits	unpack to unsigned int32
$D_i(0)\ldots D_i(3)$	4 x 24 bits	unpack to unsigned int32
T_i	16-bits	unpack to unsigned int16
DIO Counter Status	8-bits	unpack to byte
LO lock Status	8-bits	unpack to byte

where subscript i denotes band 1 or 3.

5. Field 'SM11 DACS 1 band dacs-2' in Science packet Type II Packet 2 (Byte offset 590)
   or

6. Field 'SM12 DACS 2 band dacs-4' in Science packet Type III Packet 2 (Byte offset 590)
   These fields contain uncompressed data for the first 82 lags of the second band on the
   selected assembly. Status bytes for these bands are those of the corresponding Packet 1.
   All data from the other assembly is discarded in the C&DH.

$K_i(0)\ldots K_i(81)$	82 x 24 bits	unpack to unsigned int32
$D_i(0)\ldots D_i(3)$	4 x 24 bits	unpack to unsigned int32
T_i	16-bits	unpack to unsigned int16
Spare	8-bits	

where subscript i denotes band 2 or 4.

H.2   Unpacking of DACS data in Science Packets

H.2.1   Type I: Compressed data unpacking

A table of signed 16-bit integer compression parameters, $A[128], L$, is hard-coded into the
flight software, and will be referenced by the software version number. The values are used

in the decompression of Type I science packets. In the current software, a single set of 129 constants is used for all of the DACS bands.

Compressed lag data for each band are unpacked into an array of signed 16-bit integers, $C_i[128]$. These lag data are loaded into the lowest 12 bits (for lags $1 \ldots 32$), and into the lowest 8 bits for lags $33 \ldots 128$, with the sign bit extended. These data are then decompressed into ρ_{2a}, an array of 129 floats:

$$
\begin{aligned}
\rho_{2a}[0] \;\; &= \;\; 1; \\
\rho_{2a}[j] \;\; &= \;\; (C[j-1] + A[j-1])/L \\
&\quad \text{where} \\
j \;\; &= \;\; 1 \ldots 128 \quad \text{is the lag index.}
\end{aligned}
$$

State counters, called $D(0) \ldots D(3)$ in the CTH, and $N_{\bar{2}}$, $N_{\bar{1}}$, N_1, N_2 in this document, are unpacked to an array of four unsigned, int32. The total power counter, called T in the CTH and p in this document, is unpacked to an unsigned int16.

H.2.2 Type II and III: Uncompressed data unpacking

Science types II and III will only be used in diagnostic modes. These packets contain a subset of the DACS data without compression. Type II contains all lags of dacs-1 and the first 82 lags of dacs-2. Type III contains all lags of dacs-3 and the first 82 lags of dacs-4. The first step in unpacking of these data is to subtract off the offset $3N_{\text{tot}}$, which is an artifact of the up-only counter implementation, and to normalize the autocorrelation by its zero lag. For Packet 1:

$$
\begin{aligned}
\rho_{2a}[0] \;\; &= \;\; 1 \\
\rho_{2a}[j] \;\; &= \;\; (K_i[j] - 3N_{\text{tot}})/(K_i[0] - 3N_{\text{tot}}) \\
&\quad \text{where} \\
j \;\; &= \;\; 1 \ldots 128 \quad \text{is the lag index.}
\end{aligned}
$$

Divide-by-zero exceptions should be avoided:

$$
\text{If} \quad K[0] = 3N_{\text{tot}}, \quad \rho_{2a}[j] = 0 \quad \text{for all} \quad j = 0 : 128.
$$

State counter data, $D(k)(\text{CTH}) \to N_k$ (this document), and the total power counter, $T(\text{CTH}) \to p$ (this document), are int32 and unsigned int16 respectively, just as they were with compressed data. For Packet 2:
These data packets are handled the same as Packet 1 except that $\rho_{2a}(j) = 0$ for $82 \le j \le 128$. Lags which have been explicitly set to zero should not be modified in the next section.

H.3 Fix Lost Carry Bits in State Counters

The state counters, N_k, accumulate the number of instances in which a 2-bit digitized input to an autocorrelator chip was in each of its four states. With the digitizer thresholds set at

-0.9σ, 0σ and 0.9σ, the low-magnitude counters, $N_{\bar{1}}$ and N_1, have values[1] near 82,000 with random noise components of about 60 counts rms. The high-magnitude counters, $N_{\bar{2}}$ and N_2, are near 48,000 with rms random noise components of about 50 counts.

Each of the four state counters from each of the four DACS bands have occasional single-bit errors. These errors are uncorrelated among counters and consist of a bit erroneously set to zero followed by a string of trailing zeros, as if a bit rippling through a counter is lost as the integration window ends. These errors are likely due to a hardware bug in the correlator chips.

The sum, N_{tot}, should be nearly constant, as it is the number of 25 MHz clock ticks in a 1/6 s data integration divided by 16 (only 24 bits of the correlator's internal 28-bit counters are readable). The standard deviation of this total should be less than one count, but bit-errors give the error distribution a tail of negative errors.

The observed errors are consistent with a carry-bit being lost at a rate one per 210 MIFs per band. Half of these errors are in the least significant bit, which is flipping most often. Error rates for successive bits drop by a factor of two, giving errors as large as 2^n at a rate of 1 per $210 * 2^n$ MIFs. For errors larger than the standard deviations of the counters, error statistics become skewed. For example, if the mean value of a state counter happens to be close to a large power of two, errors in the corresponding bit will be more likely.

Ignoring these possibly skewed statistics, single-bit errors as large as 1024 are expected in each band at a rate of approximately one every ten hours. An error of 1024 in a state counter is of the order 1–2% of a typical value in a counter. When using the counters in the 2-bit nonlinearity correction, errors of this magnitude in a state counter result in correlated fractional errors in channel radiances of less than $4*10^{-4}$ over useful DACS channels (100 kHz – 10.5 MHz). For a 200 K scene and a 1500 K receiver temperature, the resulting error in brightness temperature is on the order of 0.7 K.

Fortunately, significant counter bit errors are easily identified and corrected. A power-of-two glitch in the sum of the four counters identifies a bit-error's presence. A tail of trailing zeros up, and including the miss-set bit in one of the counters is the signature which identifies the particular counter needing correction. The errors will be identified after subtracting off a median counter sum, which will typically be calculated over the day's worth of data being processed. In the absence of MIF duration adjustments for orbital synchronization, these values should be nearly constant, and unexplained changes will be an indication of problems with the 25 MHz DACS clock, the instrument Master Oscillator, or the Master RIU.

H.3.1   State Counter Correction Algorithm

This processing is done on the state counters of each band, separately.

- Sum state counters: $N_{\text{tot}} = N_{\bar{2}} + N_{\bar{1}} + N_1 + N_2$.

- Median filter: $\bar{N}_{\text{tot}} = median(N_{\text{tot}})$. The median will typically be taken over the one-day block of data being processed.

- Calculate errors: $E = \bar{N}_{\text{tot}} - N_{\text{tot}}$.

- Find MIFs, j, for which E exceeds a threshold, (e.g., 48 to find bit-errors of 64 or larger).

---

[1]The count and noise values presented here are for the nominal MIF duration of $\frac{1}{6}$ s.

- For these MIFs, find the bit in which a single error could account for E: $b = round(log_2(E))$.

- Count the trailing zeros for each of the counters in MIF j:

  - If only one counter has b_j or more trailing zeros, this is the counter with the bit error. Add 2^{b_j} to this counter.

  - If more than one counter has b_j or more trailing zeros, compare the candidate counters to corresponding counters in the adjacent MIFs. Add 2^{b_j} to the candidate counter for which $N_{k,j} - (N_{k,j+1} + N_{k,j-1})/2$ is minimum.

  - If no counter in MIF j has b_j trailing zeros, check if two counters have $b_j - 1$ trailing zeros. If so, add 2^{b_j-1} to each of these counters. If not, add 2^{b_j-2} to all four counters and flag the MIF/band.

H.3.2 Calculate State Counter Statistics

The state counters are used to estimate the position of the digitizer thresholds in units of the standard deviation of the Gaussian noise input. In these units, the threshold magnitudes will decrease as the input power increases. These statistics are intermediate steps both for the estimation of multi-bit correlation from modified 2-bit correlation and in the estimation of signal total power from the state counters.

The positive threshold, in units of the Gaussian noise input signal standard deviation measured from the center of the input distribution, is given by

$$t_P = \sqrt{2} \cdot \mathbf{erfinv}(1 - 2 \cdot N_{\bar{2}}/N_{\text{tot}}). \tag{H.1}$$

The absolute value of the negative threshold, in units of the input signal standard deviation measured from the center of the input distribution, is given by

$$t_N = \sqrt{2} \cdot \mathbf{erfinv}(1 - 2 \cdot N_2/N_{\text{tot}}). \tag{H.2}$$

The Zero-cross threshold, in units of the input signal standard deviation measured from the center of the input distribution, plus 0.5 is given by

$$t_Z = \sqrt{2} \cdot \mathbf{erfinv}(1 - 2 \cdot (N_{\bar{2}} + N_{\bar{1}})/N_{\text{tot}}). \tag{H.3}$$

In the definitions above,

$$x = \mathbf{erfinv}(y) \quad \text{satisfies} \quad y = \mathbf{erf}(x),$$
$$\text{for} \quad -1 \le y < 1, \quad -\infty \le x \le \infty$$

where

$$\mathbf{erf}(x) \equiv \frac{2}{\sqrt{\pi}} \cdot \int_0^x \exp(-t^2)\, dt.$$

H.4   Estimation of multi-bit autocorrelation function ($\hat{\rho}$) from the 2-bit autocorrelation function (ρ_{2n})

Continuous autocorrelation is estimated from the measurement of the modified 2-bit autocorrelation and the counter statistics, as discussed in Section G.4. The fit is given by Equation H.4

$$\alpha = (t_P + t_N)/2 - 0.9$$
$$\beta = t_P - t_N$$
$$
\begin{aligned}
\rho(\rho_{2a}, M, A, t_Z) \cong & + 0.97523832394051 \cdot \rho_{2a} \\
& - 0.02380373485444 \cdot \rho_{2a}^3 \\
& + 0.02319837842563 \cdot \rho_{2a}^5 \\
& - 0.13041441630665 \cdot \alpha \cdot \sin(2.65669554475991 \cdot \rho_{2a}) \\
& + 0.07972045694408 \cdot \alpha^2 \cdot \sin(2.53913134278926 \cdot \rho_{2a}) \\
& + 0.00584883449926 \cdot \alpha \cdot \sin(5.41377429222816 \cdot \rho_{2a}) \\
& - 0.06240191899064 \cdot \beta^2 \\
& + 0.18411511458856 \cdot \beta^2 \cdot \rho_{2a} \\
& + 0.36609609800433 \cdot t_Z^2 \cdot \rho_{2a} \\
& - 0.37590269144600 \cdot t_Z \cdot \beta
\end{aligned}
\tag{H.4}
$$

These coefficients were fit with a nonlinear solver in Matlab over $-0.15\sigma \leq \alpha \leq 0.15\sigma$, $-0.05\sigma \leq \beta \leq 0.05\sigma$, $-0.10\sigma \leq t_Z \leq 0.10\sigma$, and $-0.40 \leq \rho_{2a} \leq 0.40$, and provide an average inversion error of 2.25e-5, and worst-case errors of 1.32e-4. Errors are smaller near the nominal values of $t_Z = 0$, $\beta = 0$, $\alpha = 0$.

The zero lag of the normalized autocorrelation function is identically one and should not be corrected. For Types II and III packet 2 data (uncompressed, truncated to 82 lags), lags 82 . . . 128 should be left as zeros.

H.5   Apodization

The DACS have a sharp cutoff in the time domain after lag 128. Their outputs are equivalent to sampled autocorrelations with an infinite number of lags multiplied by a boxcar. In the frequency-domain, this is an impulse train convolved with a $\sin(n\pi)/(n\pi)$ where n is the channel number offset. Individual channels have responses which ring, falling off only as (lag offset)$^{-1}$. Weighting the lags with a function which decreases approaching the cutoff smooths this sharp edge ('cuts off the feet') of the channel responses in the frequency domain. The resulting apodized individual channel responses in the frequency domain have broader main lobes, but reduced side lobes. Apodization makes the individual channel responses more local, but throws away some high-frequency information.

H. Pickett has suggested that subtleties involving non-locality of channels in frequency, and nonlinearity of the calibration, should be considered. Lower sidelobe responses may reduce the effects of the sharp anti-aliasing filter in the DACS IF upon channels some distance from this edge. This may, in turn, simplify forward model calculations by reducing the required frequency resolution for a given error. This is a topic for further research.

H.6   Scale by Total Power

Up to this point, the autocorrelation ρ has been normalized so that the zero lag has value one. For each band, the normalized autocorrelation function, ρ, should be scaled by the best estimate of band total power, $\hat{p}$:

$$G(j) = \hat{p} \cdot \rho(j).$$

Then zero lag in the time domain will correctly be the integrated power of all of the channels of the power spectral density after transformation into the frequency domain.

A total power measurement, p, will be provided by the analog total power circuit. The units of the total power measurement are not important as they will be removed in calibration, however the measurement must be proportional to total power, so the analog channel's zero offset, p_z, must be removed.

$$\hat{p} = p - p_z. \tag{H.5}$$

As is the case with the filter spectrometers, zero offset, p_z, will be measured periodically by increasing IF attenuation. Care must be taken not to leave the comparators of the digitizers in unstable states as the input signals are reduced, as oscillations on the DACS boards can leak noise into the analog channels.

An alternative total power measurement may be inferred from the statistics of the state counters of the digitizers. For fixed threshold voltages, the statistics t_P and t_N, which were defined in Section H.3.2, are the ratio of the positive and negative threshold magnitudes to the noise signal input standard deviation. Since Gaussian noise signal power is proportional to the square of signal standard deviation, we can define a quantity p_d which is proportional to input power:

$$p_d = t_P^{-2} + t_N^{-2}. \tag{H.6}$$

Quantization noise makes p_d an inherently noisier quantity than p, and longer integration times are needed to match the precision of calibrated measurements obtained using p. Unfortunately, the comparators used in the DACS digitizer have significant roll-off with frequency, so the analog channel's total power measurement is not really the correctly-weighted average of band power to be used in normalizing the correlator output. Initial versions of the Level 1 software will use the analog channel's total-power measurement. Comparison with results using the digital data will be a research topic. The relation between p and p_d will also provide a consistancy check of measurement linearity and an additional way to measure the zero offset, p_z.

H.7   Discrete Cosine Transform

The power-spectral-density (PSD) of a stationary, ergodic process is the Fourier transform of its autocorrelation function. We estimate the autocorrelation function for 129 lags with non-negative delays ($\tau \in 0 \ldots 5.12\,\mu s$) and assume that the autocorrelation function is even in time lag, as is the case for these noise signals. Over the time scale of our integrations, the noise statistics do not change and the autocorrelation is the same forward and backward in time.

The PSD may be written explicitly as a discrete cosine transfer (DCT) of the 129 measured lags:

$$A(k) = G(0) + G(N) \cdot (-1)^k + 2 \sum_{j=1}^{N-1} G(j) \cos(\frac{\pi k j}{N})$$

$$\text{for}$$
$$J = 1 \ldots (N-1).$$

Equivalently, the 129-point DCT may be implemented with a 256-point Fast Fourier transform (FFT):

$$\tilde{A} = \mathbf{FFT}([G(0) \ldots G(N), G(N-1) \ldots G(1)])$$
$$A = \tilde{A}(0 \ldots N).$$

$A(k)$ is the power at frequency $\nu_k = k \times 97.656$ kHz. Here, we are still dealing with uncalibrated radiances. They have been scaled by total power measurements which have, as yet, unknown gains and offsets.

H.8   DACS Calibration

As was discussed in Section 4.7, one method of calibrating the DACS is to treat each channel separately, calibrating A as if it were a 129-channel filterbank. This involves 129 sets of interpolations of Space and Target views to times of Limb views. There are, however, advantages to maintaining normalized spectra $G(j)$ and total power p of the space and target observations as separate quantities during the initial stages of the calibration process.

The normalized spectra of the calibration views, A_{space} and A_{target}, have almost no 1/f noise due to gain drift, and can be averaged over extremely long time windows. The 1/f noise is almost exclusively in the total-power measurements. Total power and normalized spectra of the calibration views will be filtered separately. Given the stability we expect in orbit, it may be appropriate to average a day's Space and Target normalized spectra, or to use constant spectral shapes to be updated as needed. The total power channels will have noise statistics very similar to the 12 MHz and 8 MHz wide channels of the corresponding filterbanks (see Table H.1), and should be interpolated similarly.

While normalized spectra of the ambient target and of a liquid nitrogen load (proxy for space in the lab) have been measured to be very similar, they have systematic differences on the order of 1×10^{-3}, or on the order of 1 K in radiance. If the normalized spectra of Space and Target views were identical, a single gain per band could be calculated, reducing the computational burden of interpolations. A first-order correction for the effects of the spectral differences between Space and Target permits a single gain per band to be interpolated to the times of limb observations.

Assume that the normalized spectrum when viewing the target, A_t, differs only slightly from that seen when viewing space, A_s. We can write $A_t(i) = A_s(i) + X(i)$, where $X(i) \ll$

$A_s(i)$ for all channels, i. The gain for channel i may be written

$$
\begin{aligned}
g(i) &= \frac{T_t - T_s}{A_t(i)(p_t - p_z) - A_s(i)(p_s - p_z)} \\
&= \frac{T_t - T_s}{(A_s(i) + X(i))(p_t - p_z) - A_s(i)(p_s - p_z)} \\
&= \frac{T_t - T_s}{A_s(i)(p_t - p_s) + X(i)(p_t - p_0)} \\
&\cong \left(\frac{T_t - T_s}{A_s(i)(p_t - p_s)} \right) \left(1 - \frac{X(i)}{A_s(i)} \frac{(p_t - p_z)}{(p_t - p_s)} \right)
\end{aligned}
\tag{H.7}
$$

where T_t and T_s are Target and Space brightness temperatures (power/k_B), and p_z is the total-power measurement zero offset. Treating A_s and A_t as constant, at least over the block of data being calibrated, this expression for gain only requires interpolation of scalar quantities constructed with band total-power measurements. The first term on the righthand side of Equation H.7 is band total-power gain divided by the Space view normalized filter shape $A_s(i)$. Band total-power gain will be interpolated as for a filterbank, while $A_s(i)$ will be a longer-term average (details pending stability studies.) The second term on the right hand side of Equation H.7 is a linear correction term to account for changes in the filter shape between Target and Space views. $X/A_s(i)$ is of order 10^{-3}, and $(p_t - p_z)/(p_t - p_s)$ is $(T_{\mathrm{sys}} + T_t)/T_t$ and of order 5, so higher powers of this correction term may be neglected. In the expressions for noise given in Appendix C, the correction term will be dropped altogether.

Appendix I

Notation

The first occurrence of each symbol in this document is indicated in the table below, together with a brief description. If a symbol has more than one use, the first occurrence with each usage is included. To minimize confusion where the same symbol may have more than two meanings in this document, separate Notation tables are provided at the ends of the Appendixes discussing Optimal Interpolation and the DACS. Appendix F which describes the noise characteristics of integrators and detectors, and Appendix B which discusses heterodyne radiometers, both use several symbols which have slightly different meanings than elsewhere in this document, and since both are largely self-standing and fairly brief, they are not covered by the following Notation table.

Symbol	Unit	Eqn.	Description
a		4.21	quadratic fit coefficient
a		5.4	conversion coefficient for PRD data processing
b		4.21	quadratic fit coefficient
b		5.4	conversion coefficient for PRD data processing
c	ms^{-1}	B.2	speed of light
c		4.21	quadratic fit coefficient
c		5.6	conversion coefficient for thermistor data processing
d		5.6	conversion coefficient for thermistor data processing
e		5.6	conversion coefficient for thermistor data processing
f		5.6	conversion coefficient for thermistor data processing
f$_\mathrm{h}$	Hz	5.3	V/F converter output frequency during low calibration measurement
f$_\mathrm{l}$	Hz	5.3	V/F converter output frequency during high calibration measurement
f$_\mathrm{v}$	Hz	5.1	V/F converter output frequency
g_i	Counts K^{-1}	4.17	radiometric gain of channel i at the switching mirror
$\hat{g}_i(L)$	Counts K^{-1}	4.19	interpolated gain of channel i at time of limb view
h	Js	4.1	Planck's constant, $6.62606891{\times}10{-}34$
i,s		4.5	channel i, sideband s (s is one of l or u)
j		4.21	MIF (time) index for quadratic fit
k	JK^{-1}	4.1	Boltzmann's constant, $1.380658{\times}10^{-23}$
r		4.5	identifies one of seven radiometers

r_l, r_u		4.4	lower and upper sideband responses of entire signal chain (including antenna)
r'_l, r'_u		4.8	lower and upper sideband responses of signal chain from radiometers (mixers) to switching mirror
s	Counts	4.32	sample variance
w_j		4.26	weighting applied to measurement j in least squares fit
x	V/Ω	5.3	calibrated multiplexed analog value
B_i	Hz	4.20	Predetection bandwidth of filter channel i
C_h		5.3	multiplexed analog 'high' calibration value
C_l		5.3	multiplexed analog 'low' calibration value
C_i^L	Counts	4.17	digitizer output viewing atmospheric limb
C_i^N	Counts	4.17	digitizer output random noise
C_i^O	Counts	4.17	digitizer output offset
$\widehat{C}_i^S(T)$	Counts	4.19	interpolated space reference signal at time of target view for channel i
C_i^S	Counts	4.17	digitizer output when viewing space
C_i^T	Counts	4.17	digitizer output viewing target
C_h	Hz	5.3	multiplexed analog 'high' calibration input
C_l	Hz	5.3	multiplexed analog 'low' calibration input
$F_i(\nu)$		4.3	radiometer frequency response function
$G^M(\nu, \theta, \phi)$		4.3	gain function at switching mirror
$G_r^A(\theta, \phi)$		4.7	antenna gain function for radiometer r
$H(f)$		4.40	Frequency (power) response of post-detector radiometric calibration process
$\overset{\bullet}{I}_i^L$	K	4.12	Level 2 estimate of limb radiance reaching switching mirror
$\overset{\bullet}{I}_\nu(\theta, \phi)$	WSr^{-1}Hz^{-1}	4.3	spectral radiance per unit frequency per unit solid angle
N		4.33	number of data points
N_t		5.1	Number of timebase cycles counted in an engineering data integration
N_v		5.1	Number of V/F converter cycles counted in an engineering data integration
$\overset{\bullet}{P}$	K	4.1	measured radiant power per unit bandwidth
$\overset{\bullet}{P}^A$	K	4.8	Limb radiance
$\langle \overset{\bullet}{P}_i^A \rangle$	K	4.13	Level 1 estimate of atmospheric limb radiance
$\overset{\star}{\overset{\bullet}{P}}_i^A$	K	4.12	Forward Model estimate of limb radiance collected by the antenna
$\overset{\bullet}{P}^L$	K	4.8	radiance at switching mirror limb port
$\overset{\bullet}{P}_r^{Bx}$	K	4.17	$\overset{\bullet}{P}$ for switching mirror baffle at port x for radiometer r
R_{in}	Ω	5.5	measured resistance of parallel thermistor/resistor pair
R_{th}	Ω	5.5	inferred thermistor resistance
R_{tlm}	Ω	5.4	measured PRD resistance
$S_g(f)$		4.40	non-spectrally flat component of post-detector noise power spectral density
T	K	4.1	temperature

T	C	5.4	inferred temperature (Celsius) of PRD
Δ		4.25	coefficient determinant in polynomial least squares fit
ϵ_r		4.18	calibration target emissivity for center frequency of radiometer r
$\eta_{i,s}^{MX}$		4.5	integrated gain over baffle aperture X
$\eta_{i,s}^{A}$		4.8	antenna transmission (scattering)
$\eta_{i,s}^{k}$		4.16	optical transmission of reflector k
λ_r	MIFs	4.26	$\frac{1}{e}$ rolloff distance for relative weightings in least squares fit
ν	Hz	4.1	radiation frequency
ν_{LO}	Hz	4.4	Local Oscillator frequency
ρ_r^{A}		4.8	antenna ohmic loss (cumulative)
$\rho_r^{1,2,3}$		4.16	ohmic loss for reflector 1,2,3
$\sigma(j)$	Counts	4.27	rms of measurement j
$\sigma'(j)$	Counts	4.27	weighted rms of measurement j
τ	s	4.20	data post-detector integration time
Ω_A		4.7	angle over which antenna pattern is defined
Ω_{MX}		4.4	solid angle defined by baffles
$d\Omega$		4.4	element of solid angle $[d\Omega = \sin(\theta)\, d\theta\, d\phi]$

Appendix J

Glossary

A/D	analog-to-digital
ADC	analog-to-digital converter
ASIC	Application Specific Integrated Circuit
C&DH	Control and Data Handling Assembly
CCSDS	Consultative Committee for Space Data Systems
CTH	Command and Telemetry Handbook (for the C&DH Flight Software)
CW	Continuous wave
D/A	digital-to-analog
DACS	Digital AutoCorrelator Spectrometer
DFT	Discrete Fourier Transform
EDH	Engineering Data Hybrid
EM	Engineering Model
EOS	Earth Observing System
FFT	Fast Fourier Transform
FM	Flight Model
FTI	Fourier Transform Interferometer
GB	Gigabyte, $\sim 10^9$ bytes
GSE	Ground Support Equipment
HDF	Hierarchical Data Format
HEMT	High Electron Mobility Transistor
HIRDLS	High-Resolution Dynamics Limb Sounder
IRU	Inertial Reference Unit
MAF	Major Frame
MB	Megabyte, $\sim 10^6$ bytes
MFLOPS	Millions of Floating Point Instructions per Second
MIF	Minor Frame
MIPS	Millions of Instructions per Second
MLS	Microwave Limb Sounder
msb	most significant bit
PRD	Platinum Resistance Device (temperature tranducer)
RAID	Redundant Array of Inexpensive Disks
RIU	Remote Interface Unit
SCF	Science Computing Facility

SIDS	Simulated Instrument Data Set
SLS	Submillimeter Limb Sounder
SMP	Symmetric Multi-Processor, a form of parallel computer
S/N	Signal-to-noise
TBR	to be revised
TES	Tropospheric Emission Spectrometer
UARS	Upper Atmosphere Research Satellite
UTC	Coordinated Universal Time (GMT)
V/F	voltage-to-frequency
VFC	V/F converter

Bibliography

[1] Waters, J.W., An Overview of the EOS MLS Experiment, JPL D-15745, Version 1.0, 15 Jan. 1999.

[2] MTPE EOS Reference Handbook 1995, available from the EOS Project Science Office, code 900, NASA Goddard Space Flight Center, Greenbelt, MD 20771.

[3] Jarnot, R.F. and Cofield, R.E., Microwave Limb Sounder (MLS) Instrument Calibration Report, JPL Document D–9394, August 1991.

[4] Jarnot, R.F., Cofield, R.E., Waters, J.W. and Flower, D.E., Calibration of the Microwave Limb Sounder on the Upper Atmosphere Research Satellite, *J. Geophys Res.*, 101 , April 1996, No. D6, 9957–9982.

[5] Hersman, M.S. and Poe, G.E., Sensitivity of the Total Power Radiometer with Periodic Absolute Calibration, *IEEE Transactions on Microwave Theory and Techniques*, Vol. MTT-29, No, 1, 32–40, January 1981.

[6] Peckham, G.E., An Optimum Calibration Procedure for Radiometers, *Int. J. of Remote Sensing*, Vol. 10, 227–236, 1989.

[7] Interface Control Document for the Microwave Limb Sounder (MLS) EOS Common Spacecraft Project, TRW document D26475, 31 July 2000.

[8] Robinson, F.N.H., Noise and Fluctuations in Electronic Devices and Circuits, Clarendon Press, Oxford, 1974, Chapter 19.

[9] Cooper, B.F.C., Correlators With Two-Bit Quantization, *Aust J. Physics*, 1970, **23**, 521-527.

[10] Hagen, J.B., Farley D.T., Digital-correlation techniques in radio science, *Radio Science*, Volume 8, Numbers 8, 9, 775–784, August–September 1973.

[11] Lau, C.L., Peckham, G.E., Suttie, R.A., Jarnot, R.F., Characterization of MLS $\frac{1}{f}$ noise parameters, *Int. J. Remote Sensing*, 1996, Vol. 17, No. 18, 3751–3759.

[12] Girard, M., Instrument Flight Software Requirements Document, JPL D-15384, September 1998.

[13] Girard, M., Instrument Flight Software Command and Telemetry Handbook, JPL D-16761, January 2002.

[14] Livesey, N.J. and Wu, D.L., EOS MLS Retrieval Processes Algorithm Theoretical Basis, JPL D-16159, Version 1.0, 15 Jan. 1999.